



## Invited paper

# Evolution of the Global Overturning Circulation since the Last Glacial Maximum based on marine authigenic neodymium isotopes



Jianghui Du <sup>a, b, \*</sup>, Brian A. Haley <sup>a</sup>, Alan C. Mix <sup>a</sup>

<sup>a</sup> College of Earth, Ocean and Atmospheric Sciences, Oregon State University, Corvallis, OR, 97331, USA

<sup>b</sup> Department of Earth Sciences, Institute of Geochemistry and Petrology, ETH Zürich, Clausiusstrasse 25, 8092, Zürich, Switzerland

## ARTICLE INFO

## Article history:

Received 13 February 2020

Received in revised form

29 May 2020

Accepted 29 May 2020

Available online 25 June 2020

## Keywords:

Ocean circulation  
Last glacial maximum  
Last deglaciation  
Paleoceanography  
Paleoclimate  
Neodymium isotopes  
Marine Nd Cycle  
Authigenic phase  
Detrital sediments

## ABSTRACT

The Global Overturning Circulation is linked to climate change on glacial-interglacial and multi-millennial timescales. The understanding of past climate-circulation links remains hindered by apparent conflicts among proxy measures of circulation. Here we reconstruct circulation changes since the Last Glacial Maximum (LGM) based on a global synthesis of authigenic neodymium isotope records ( $\epsilon_{Nd}$ ). We propose the bottom-up framework of interpreting seawater and authigenic  $\epsilon_{Nd}$  considering not only conservative watermass mixing, but also the preformed properties and the non-conservative behavior of  $\epsilon_{Nd}$ , both subject to sedimentary influences. We extract the major spatial-temporal modes of authigenic  $\epsilon_{Nd}$  using Principal Component Analysis, and make a first-order circulation reconstruction with budget-constrained box model simulations. We show that during the LGM, the source region of North Atlantic overturning shifted southward, which led to more radiogenic preformed  $\epsilon_{Nd}$  of glacial Northern Source Water (NSW). Considering this preformed effect, we infer that glacial deep Atlantic had a similar proportion of NSW as today, although the overall strength of glacial circulation appears reduced from both North Atlantic and Southern Ocean sources, which increased the relative importance of non-conservative behavior of  $\epsilon_{Nd}$  and may have facilitated accumulation of respired carbon in the deep ocean. During the deglaciation, we find that Southern Ocean overturning increased, which offset suppressed North Atlantic overturning and resulted in a net stronger global abyssal circulation. Faster global scale deglacial circulation reduced the relative importance of non-conservative effects, resulting in Atlantic-Pacific convergence of abyssal  $\epsilon_{Nd}$  signatures. Variations of Southern Ocean overturning likely drove a significant fraction of deglacial changes in atmospheric  $CO_2$  and oceanic heat budget.

© 2020 The Author(s). Published by Elsevier Ltd. This is an open access article under the CC BY-NC-ND license (<http://creativecommons.org/licenses/by-nc-nd/4.0/>).

## 1. Introduction

### 1.1. The Ocean's overturning circulation

The Global Overturning Circulation (GOC) is responsible for the transport of carbon and heat among the ocean basins and between the ocean and the atmosphere. The GOC can be conceptualized primarily as two connected overturning cells (Talley, 2013). The upper cell is linked to the formation of North Atlantic Deep Water (NADW) and its shallower return flow to form the Atlantic Meridional Overturning Circulation (AMOC), roughly in the depth range 1500–3500 m. The lower cell is associated with the production of Antarctic Bottom Water (AABW) which occupies the deeper parts of

the abyssal ocean, and its return flow mostly as Pacific Deep Water (PDW) and is referred to as the Southern Ocean Meridional Overturning Circulation (SOMOC). These two circulation cells are interconnected via upwelling in the Southern Ocean where deep waters are mixed in the circumpolar circulation. Part of the resultant mixture contributes to AABW formation locally, and the rest converts to less dense watermasses transported northward at intermediate and shallower depths, such as the Antarctic Intermediate Water (AAIW) and various mode waters, eventually contributing to the production of NADW. There is no deep water formation in the North Pacific today: instead, there is a weak cell of North Pacific Intermediate Water (NPIW) circulation. In paleoceanography, the NADW and AABW watermasses are commonly referred to as Northern and Southern Source Waters (NSW and SSW). Because the largest reactive carbon reservoir on glacial-interglacial and deglacial millennial scales is the deep ocean, we will mainly focus on the abyssal circulation in this study.

\* Corresponding author.

E-mail address: [jianghui.du@erdw.ethz.ch](mailto:jianghui.du@erdw.ethz.ch) (J. Du).

That the GOC influences the global carbon cycle and heat transport is a leading tenet in paleoclimatology (Shakun et al., 2012). However, despite decades of research, a globally consistent description of the changes in the GOC, for example since the Last Glacial Maximum (LGM), remains elusive. Geochemical proxies often lead to diverging interpretations on the various aspects of the GOC (Curry and Oppo, 2005; Gebbie, 2014; Lund et al., 2011; McManus et al., 2004; Negre et al., 2010; Oppo et al., 2018; Roberts et al., 2010), and climate models similarly produce conflicting arrays of the GOC behavior (Amrhein et al., 2018; Kurahashi-Nakamura et al., 2017; Menviel et al., 2016; Muglia et al., 2018; Muglia and Schmittner, 2015; Otto-Bliesner et al., 2007). Four critical issues are highly debated as a result, namely: (1) the mixing proportions of NSW and SSW in the glacial deep Atlantic, with suggestions ranging between <50% and ~100% (Amrhein et al., 2018; Duplessy et al., 1988; Gebbie, 2014; Kurahashi-Nakamura et al., 2017; Lang et al., 2016; Oppo et al., 2018; Sarin et al., 1994); (2) the strength of the AMOC during deglacial stadial events such as Heinrich Stadial 1 (HS1, 18–15 ka), whether the AMOC ceased completely (McManus et al., 2004) or was weakened but present (Bradt Miller et al., 2014); (3) whether the AMOC and SOMOC respond oppositely or in the same directions to climate changes on glacial-interglacial and deglacial millennial timescales (Broecker, 1998; Menviel et al., 2016, 2014); (4) potential changes of Pacific circulation, which remains under-constrained (Broecker et al., 2008, 2004; Davies-Walczak et al., 2014; Lund, 2013; Lund et al., 2011; Marchitto et al., 2007; Okazaki et al., 2010; Sikes et al., 2000).

Such controversies arise because geochemical tracers are often affected by more than circulation alone, and they may also be related to circulation in multiple ways. For instance, benthic stable carbon isotopes ( $\delta^{13}\text{C}$ ) may be interpreted from the perspective of binary NSW/SSW mixing (Oppo and Fairbanks, 1987), but temporal changes of the preformed  $\delta^{13}\text{C}$  linked to air-sea exchange (Lynch-Stieglitz et al., 2019; Mix and Fairbanks, 1985) and non-conservative effects due to remineralization could also be significant (Gebbie, 2014). Benthic radiocarbon ( $\Delta^{14}\text{C}$ ) is affected by circulation rate, as well as watermass mixing, preformed age and potential interior sources/sinks such as  $^{14}\text{C}$ -dead hydrothermal carbon (Ronge et al., 2016; Skinner et al., 2010; Zhao et al., 2018). Marine sediment  $^{231}\text{Pa}/^{230}\text{Th}$  may be affected by particle-selective scavenging and preformed properties in addition to circulation strength (Deng et al., 2018). Given multiple controls of these tracers, their evidence of paleo-overturning circulation remains underdetermined.

Realistic tracers of the GOC must have residence times comparable to that of ocean circulation; consequently, their marine cycles inherently have large-scale global and basinal components, superimposed upon any local factors. Thus, constraints on the global and basinal tracer budgets are needed for robust interpretation of tracer data at any individual location. Such constraints remain limited by the relative paucity of information about the Southern and Pacific Oceans. The Pacific has both the largest volume and thus largest tracer reservoirs; the Pacific is also mainly ventilated by the SOMOC, which, in turn, includes mixed components of Atlantic and Pacific waters (Broecker et al., 1985; Rae and Broecker, 2018). As the nexus of mixing between basinal watermasses, the Southern Ocean mediates the tracer budgets of both the Pacific and Atlantic, making them non-independent (Marinov et al., 2006; Vance et al., 2017). Ultimately, the Pacific-Southern Ocean link must be critical in regulating the global budgets of such tracers, even in the Atlantic Ocean, depending on the residence times of seawater and the tracer.

The closure of the GOC requires wind-driven upwelling and other vertical mixing processes that bring deep water back to the

surface (Ferrari, 2014). The Southern Ocean is the main location of deep water upwelling, driven by southern westerlies (Marshall and Speer, 2012). The Pacific is the main location for diapycnal transformations of dense deep water to lighter density class waters because it has the largest seafloor areas for turbulent mixing in the Benthic Boundary Layer (de Lavergne et al., 2017; Talley, 2013). Again, Pacific and Southern Ocean circulation is critical to the sustenance of the GOC.

Because the various watermasses that comprise the GOC are interconnected, reconstructing the GOC demands a global synthesis constrained by tracer budgets, while taking into account the multifaceted connections these tracers may have with ocean circulation (mixing ratios, circulation rate, mode of deep water formation, etc.), and non-circulation factors that may also vary over time and space.

## 1.2. Neodymium isotopes as a circulation tracer

Here we summarize global patterns of change since the LGM in radiogenic neodymium (Nd) isotope composition (the  $^{143}\text{Nd}/^{144}\text{Nd}$  ratio) of marine authigenic phases, which is an important tracer of paleo-circulation (Frank, 2002; Goldstein and Hemming, 2003). The radiogenic Nd isotope composition is expressed as  $\epsilon_{\text{Nd}} = [(^{143}\text{Nd}/^{144}\text{Nd})_{\text{sample}} / (^{143}\text{Nd}/^{144}\text{Nd})_{\text{CHUR}} - 1] \times 10^4$ , i.e., the parts per 10,000 deviation of a sample from the chondritic uniform reservoir (CHUR) (Jacobsen and Wasserburg, 1980). The standard terms are “radiogenic” for more positive  $\epsilon_{\text{Nd}}$  values and “unradiogenic” for more negative values.

The utility of seawater and authigenic  $\epsilon_{\text{Nd}}$  as a circulation tracer rests on the “labelling” of seawater and authigenic phases by lithogenic Nd inputs that reflect the surrounding terrestrial rock sources (Frank, 2002; Goldstein and Hemming, 2003; Jeandel et al., 2007). It is traditionally thought that this labelling happens at the surface ocean, where surface waters inherit the  $\epsilon_{\text{Nd}}$  signatures of surrounding continents through dust and dissolved riverine inputs; these surface ocean labels are carried into the ocean interior through deep water formation or brought down by settling particles through reversible scavenging (i.e., the “top-down” view) (Bertram and Elderfield, 1993; Siddall et al., 2008). More recently it has been suggested that additional labelling happens at the sediment-water interface, where bottom waters are influenced by detrital lithogenic  $\epsilon_{\text{Nd}}$  signatures through interaction with sediments (i.e., the “bottom-up” view) (Haley et al., 2017; Lacan and Jeandel, 2005a).

The application of authigenic  $\epsilon_{\text{Nd}}$  as a paleo-circulation tracer has been advanced to date largely under the top-down framework, and thus most studies treat authigenic  $\epsilon_{\text{Nd}}$  as primarily a tracer of conservative watermass mixing (Rutberg et al., 2000; Piotrowski et al., 2004; Böhm et al., 2015; Pahnke et al., 2008; Gutjahr et al., 2008; Lippold et al., 2016; Howe et al., 2016a; Roberts et al., 2010; Jonkers et al., 2015). However, since the discovery of large benthic Nd fluxes from the abyssal seafloor (Haley and Klinkhammer, 2003) and the proposal of Boundary Exchange hypothesis (Lacan and Jeandel, 2005a), it is becoming increasingly clear that sources of Nd at the ocean surface are not alone in balancing the global Nd- $\epsilon_{\text{Nd}}$  budget (Bertram and Elderfield, 1993; Jones et al., 2008; Tachikawa et al., 2003; van de Flierdt et al., 2016). More recent studies have provided strong evidence that sedimentary sources are likely the dominant Nd sources to the ocean (Du et al., 2016; Abbott et al., 2015a, 2015b; Abbott, 2019; Arsouze et al., 2009; Rempfer et al., 2011), and this progress in understanding the marine Nd cycle has informed some recent paleo-reconstructions (Blaser et al., 2019; Du et al., 2018; Pöppelmeier et al., 2019; Wilson et al., 2012).

The top-down and bottom-up views are not mutually exclusive; both are needed to understand the marine Nd cycle, and here we propose a framework that integrates both views and applies them to global paleo-circulation reconstruction. This more complete interpretive framework modifies previous interpretations of past circulation changes based on  $\epsilon_{Nd}$  and reconciles this tracer with inferences made from other tracers. Here, under this framework, we reconstruct the major features of GOC since the LGM by decomposing a collection of authigenic  $\epsilon_{Nd}$  records into global and basinal patterns and identifying non-circulation influences, aided by Principal Component Analysis (PCA) and budget-constrained box model simulations. Our objectives are (1) to provide a first-order and globally consistent description of (mainly abyssal) GOC on *global and basinal* scales since the LGM based on  $\epsilon_{Nd}$ , and (2) to provide a conceptual and methodological framework for resolving the complexities of an array of geochemical circulation tracers. Our focus is on the major deep overturning circulation cells that operate over relatively long timescales. We leave the regional details to future work, because  $\epsilon_{Nd}$  data are currently insufficient to resolve small scale changes.

## 2. Materials and methods

### 2.1. Global $\epsilon_{Nd}$ data collection

For modern seawater  $\epsilon_{Nd}$  we use existing compilations (Lacan et al., 2012; Tachikawa et al., 2017; van de Flierdt et al., 2016), complemented by data published since 2017 (Amakawa et al., 2019, 2018; Behrens et al., 2018; Che and Zhang, 2018; Dubois-Dauphin et al., 2017; Filippova et al., 2017; Garcia-Solsona and Jeandel, 2020; Grasse et al., 2017; Grenier et al., 2019, 2018; Lambelet et al., 2018; Laukert et al., 2018, 2017a; 2017b; Molina-Kescher et al., 2018; Morrison et al., 2018; Rahlf et al., 2019; Stichel et al., 2018; Struve et al., 2017; Yu et al., 2017; Zieringer et al., 2019).

For paleo-reconstruction, we compiled published authigenic  $\epsilon_{Nd}$  records that span ages since the LGM, *i.e.*, data with published ages younger than 23 ka, or reported as Holocene or LGM time-slices. The authigenic data are generated from leaching of foraminifera, fish debris, coral and bulk sedimentary Fe-Mn oxyhydroxides. Sediment leach data that do not agree with foraminifera/fish debris data from the same site are excluded. We exclude core-top authigenic data that lack age constraint demonstrating a Holocene age. Sites and references are reported in [Supplementary Table S1](#).

We create four subsets of the authigenic  $\epsilon_{Nd}$  data collection: a deglacial time-series dataset, a Holocene time-slice (0–6 ka) dataset, an LGM time-slice (19–23 ka) dataset, and a HS1 time-slice (15–18 ka) dataset. The deglacial time-series dataset includes records that span 6 to 19 ka, and have at least 10 data points (average resolution is 1.3 kyr). Data from the same site generated using various archives and from different studies are averaged to create the time-series and time-slice data. In summary, there are 72 stations with deglacial time-series records and HS1 time-slices, 259 stations with Holocene time-slice records and 155 stations with LGM time-slice records. Individual deglacial authigenic time-series are plotted in [Supplementary Table S2](#), and the time-slice data are plotted in [Supplementary Fig. S1](#).

We also compile published detrital sediment  $\epsilon_{Nd}$  data since the LGM. The detrital  $\epsilon_{Nd}$  data help to identify sedimentary influences on seawater and authigenic  $\epsilon_{Nd}$ . There is currently no standard procedure for measuring detrital sediment  $\epsilon_{Nd}$ , and the compilation includes bulk sediment digests, post-leach residuals and/or specific detrital size fractions.

Recent sediment leaching studies give evidence that certain “reactive” components of detrital sediments are more influential sedimentary Nd sources than less reactive components, which may

reflect the mineralogy and weathering history of sediments (Abbott et al., 2019, 2016; Blaser et al., 2016; Du et al., 2016; Wilson et al., 2013). As such, strong leaching procedure commonly adopted in older studies may lead to loss of reactive detrital phases which are not preserved in the operationally defined “detrital residuals” (Abbott et al., 2019, 2016; Blaser et al., 2016; Du et al., 2016; Wilson et al., 2013), while bulk sediment digestion may avoid such a problem if authigenic Nd fraction is small relative to the detrital ones (Du et al., 2016).

Moreover, recent pore water data have also shown that the  $\epsilon_{Nd}$  of sediment flux may differ from operationally defined detrital  $\epsilon_{Nd}$  (Abbott et al., 2015a), but perhaps instead reflects “reactivity-weighted” detrital  $\epsilon_{Nd}$  (Du et al., 2016; Wilson et al., 2013). Thus, we suggest that operationally defined bulk or residual detrital  $\epsilon_{Nd}$  should be used as semi-quantitative proxies for, rather than exact representations of, the  $\epsilon_{Nd}$  of sediment Nd flux. This likely works best on large spatial-temporal scales when detrital provenance can be reasonably constrained. Here we treat collected detrital  $\epsilon_{Nd}$  data equally without favoring any specific extraction method, but we call for community effort for better understanding the *reactive spectrum* of detrital Nd bearing phases in future studies.

Detrital data are processed similar to authigenic data *except* the following cases: (1) In addition to a Holocene dataset we also include a core-top (defined as within 10 cm of the sediment-water interface) dataset including sites without confirmed Holocene ages; (2) A deglacial detrital  $\epsilon_{Nd}$  record is included as long as it spans 6 to 19 ka but no resolution requirement is made because few time-series records exist; (3) A Heinrich Layer 1 (HL1) - instead of a HS1 - detrital  $\epsilon_{Nd}$  dataset is made, because the stratigraphic constraints on such data were made based on sedimentological evidence rather than absolute dating (Hemming, 2004). The distinction between HL1 and HS1 was detailed by Hodell et al. (2017). The HL1 detrital  $\epsilon_{Nd}$  data are from the subpolar North Atlantic, mainly in the classically defined ice rafted detritus (IRD) belt (40–50°N), but also extending north, close to Iceland and the Nordic Seas. Detrital sites and references are reported in [Supplementary Table S3](#).

Almost all collected sites are deeper than 500 m. Only four authigenic  $\epsilon_{Nd}$  records we know of exist from shallower sites and three of these are incomplete. Shallow sites are likely affected by local source variability in addition to circulation (Friedrich et al., 2014). We thus will not discuss shallow ocean circulation in this study. We also avoid data from the marginal seas where local detrital sediment provenance may vary and differ from the open ocean (Osborne et al., 2014; Wu et al., 2015). We exclude the Arctic Ocean because of data scarcity. Our focus is on the global distribution of  $\epsilon_{Nd}$  in the main ocean basins, especially the deep ocean.

### 2.2. Box model

We analyze the modern global ocean Nd- $\epsilon_{Nd}$  budget in a box model, which facilitates sensitivity tests and transient simulations to aid our interpretation of authigenic records. The box model has four ocean boxes: Atlantic, Pacific, Indian and Southern Ocean, and the circulation geometry follows the box geostrophic inverse models of Talley (2013) (Fig. 1A). In Talley’s estimates the Southern Ocean box is separated from the other basins at 30°S, and the related water fluxes are transports across this latitude based on hydrographic lines. This simple box model is an extension of the Pacific-only model presented in Du et al. (2018), and the governing equations for Nd concentration ( $[Nd]$ ) and  $\epsilon_{Nd}$  in a box are:

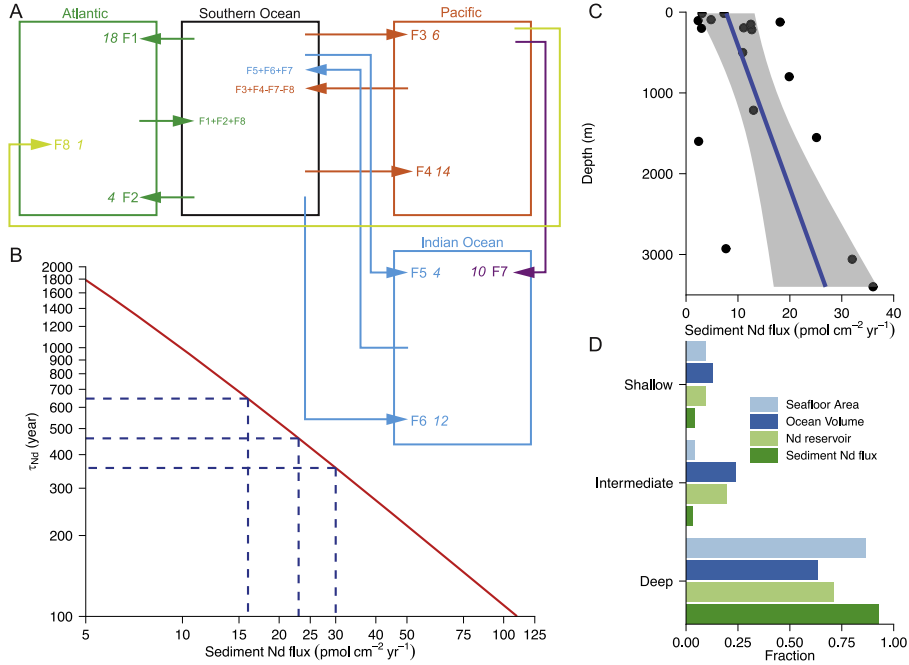


**Fig. 1.** Global box model design and the depth-distribution of Nd budget. **A:** The physical circulation in the model. The numbers following the labels are transport in Sverdrup. **B:** Dependence of the global Nd residence time  $\tau_{Nd}$  on sediment Nd flux in the box model. Range of area weighted benthic flux measurements are indicated by blue dashed lines. **C:** Sediment Nd fluxes derived using pore water and benthic chamber measurements (Abbott, 2019; Abbott et al., 2015b; Elderfield and Sholkovitz, 1987; German and Elderfield, 1989; Haley and Klinkhammer, 2003). **D:** Fractions of depth-integrated seafloor area, ocean volume, Nd reservoir and sediment Nd flux binned into three water depth categories: shallow (<500 m), intermediate (500–1500 m) and deep (>1500 m).

$$V \frac{d[Nd]}{dt} = \sum F^i \cdot ([Nd]^i - [Nd]) + S \cdot A + D + R - k \cdot [Nd] \cdot V \quad (1)$$

$$V \frac{d([Nd] \cdot \epsilon_{Nd})}{dt} = \sum F^i \cdot ([Nd]^i \cdot \epsilon_{Nd}^i - [Nd] \cdot \epsilon_{Nd}) + S \cdot A \cdot \epsilon_{Nd}^S + D \cdot \epsilon_{Nd}^D + R \cdot \epsilon_{Nd}^R - k \cdot [Nd] \cdot V \cdot \epsilon_{Nd} \quad (2)$$

where  $V$  and  $A$  are the water volume and seafloor area of the box,  $F^i$  are the water fluxes entering the box with associated  $[Nd]^i$  and  $\epsilon_{Nd}^i$ . The model has three external sources:  $S$  for sedimentary flux (mol per area per time),  $D$  for dust flux (mol per time) and  $R$  for dissolved riverine flux (mol per time).  $\epsilon_{Nd}^S$ ,  $\epsilon_{Nd}^D$ , and  $\epsilon_{Nd}^R$  are their respective isotope compositions. These sources are balanced by one external sink, scavenging, parameterized as a first order rate law of  $[Nd]$  where the removal rate constants  $k$  are allowed to vary among the ocean boxes.

The  $V$  and  $A$  of the boxes are determined using the ETOPO1 bathymetry (Amante and Eakins, 2009). When calculating  $V$  and  $A$  all depths levels are included. In the model we use volume-weighted means of  $[Nd]$  and  $\epsilon_{Nd}$  for each ocean box: we first bin seawater  $[Nd]$  and  $\epsilon_{Nd}$  data into 500 m depth intervals and compute the mean values for each depth bin. The weight for each depth bin is therefore the fraction of the ocean volume in that bin with respect to the summed volume of all the non-empty bins.  $D$  is calculated using the gridded global annual mean dust flux (Mahowald et al., 2005) assuming 20 ppm Nd in dust and 2% soluble fraction (Tachikawa et al., 2003) and  $\epsilon_{Nd}^D$  follows Tachikawa et al. (2003).  $R$  and  $\epsilon_{Nd}^R$  are from Goldstein and Jacobsen (1987). We consider the  $\epsilon_{Nd}$  of sediment Nd flux ( $\epsilon_{Nd}^S$ ) in each box to be unknowns (*i.e.*, not using the collected detrital  $\epsilon_{Nd}$  data in its stead).

In each box we then have two equations, (1) and (2), but three unknowns,  $S$ ,  $\epsilon_{Nd}^S$  and  $k$ . Thus, determination of steady-state budget requires one of the unknowns to be constrained.

Given the present knowledge of sedimentary Nd flux we are only confident in constraining the global and basinal Nd- $\epsilon_{Nd}$  budgets (Du et al., 2018, 2016). Our box model is built to reflect this limitation and as such it is suitable for quantitative investigation of large-scale changes of  $\epsilon_{Nd}$  in the deep ocean which dominates the marine Nd budget (Fig. 1D) (Du et al., 2018). Quantitative interpretation of seawater and authigenic  $\epsilon_{Nd}$  at specific locations or from shallow and intermediate-depths requires knowledge of local Nd budgets, which are often lacking. We thus mainly focus on large-scale patterns of authigenic  $\epsilon_{Nd}$  change in the deep ocean in this study. Increasing measurements and improving mechanistic understanding of the magnitude and  $\epsilon_{Nd}$  of sediment flux, and the Nd scavenging in the water column are critically important for building better marine Nd cycle models on finer spatial-temporal scales in the future.

### 2.3. Estimating the non-conservative $\epsilon_{Nd}$ in the modern ocean

We provide quantitative and globally consistent estimates of the non-conservative components of seawater and authigenic  $\epsilon_{Nd}$  in the modern ocean, as the difference between observed  $\epsilon_{Nd}$  and  $\epsilon_{Nd}$  predicted based on conservative mixing alone. If seawater  $\epsilon_{Nd}$  is strictly conservative and only has sources at the surface ocean, *i.e.*, has no internal cycling or sedimentary sources, then the conservative  $\epsilon_{Nd}$  could be estimated by propagating surface ocean  $\epsilon_{Nd}$  boundary conditions via ocean circulation. To estimate the truly conservative component of  $\epsilon_{Nd}$  (with respect to the surface boundary condition) we can use the Total Matrix Intercomparison (TMI) method (Gebbie and Huybers, 2010). Mathematically this is

equivalent to solving a set of linear equations of the form:

$$\mathbf{c} = \mathbf{A}^{-1} \mathbf{d} \quad (3)$$

where  $\mathbf{c}$  is a vector of estimated conservative  $\epsilon_{Nd}$ ,  $\mathbf{d}$  is a vector of the same size equal to observed  $\epsilon_{Nd}$  at the surface but zero in the interior, and  $\mathbf{A}$  is the circulation pathway matrix. The pathway matrix contains global steady-state watermass mixing information that links ocean interior points to the surface ocean, and is derived using modern tracer climatology. Conceptually this is similar to the Optimal Multi-Parameter Analysis (OMPA) approach often used to calculate watermass mixing ratios for regional ocean sections, which then provides a means for separation of non-conservative tracer components (Zheng et al., 2016). The advantage of TMI is that the conservative mixing components of tracers can be estimated in a globally consistent manner while also eliminating the subjective selection of a fixed-number mixing endmembers by acknowledging that all surface sites could contribute to the properties of the interior ocean. In this estimate,  $\epsilon_{Nd}$  is propagated by

circulation on its own and [Nd] is not considered. Nd concentration is well-known to be non-conservative (Goldstein and Hemming, 2003). In omitting [Nd] in this particular analysis we are implicitly favoring the hypothesis that  $\epsilon_{Nd}$  is a conservative tracer of circulation, and thus the resulting estimates of non-conservative behavior should be considered minimums.

The circulation pathway matrix  $\mathbf{A}$  is defined on a global  $4^\circ \times 4^\circ$  grid and 33 depth levels (Gebbie and Huybers, 2010). To generate the surface boundary condition  $\mathbf{d}$  (Fig. 2A), we perform variational analysis on seawater  $\epsilon_{Nd}$  observations from the upper 200 m and interpolate these data onto the TMI grid using the “DIVAnd.jl” package designed for oceanography studies (Barth et al., 2014). This package allows optimization of analysis parameters, such as correlation length scale and signal-to-noise ratio, using cross-validation methods. The analysis also produces uncertainty estimates for the surface boundary condition. To quantify the effect of this uncertainty on the resulting estimates of conservative  $\epsilon_{Nd}$  we use 1000 random realizations of the surface boundary conditions in equation (3).

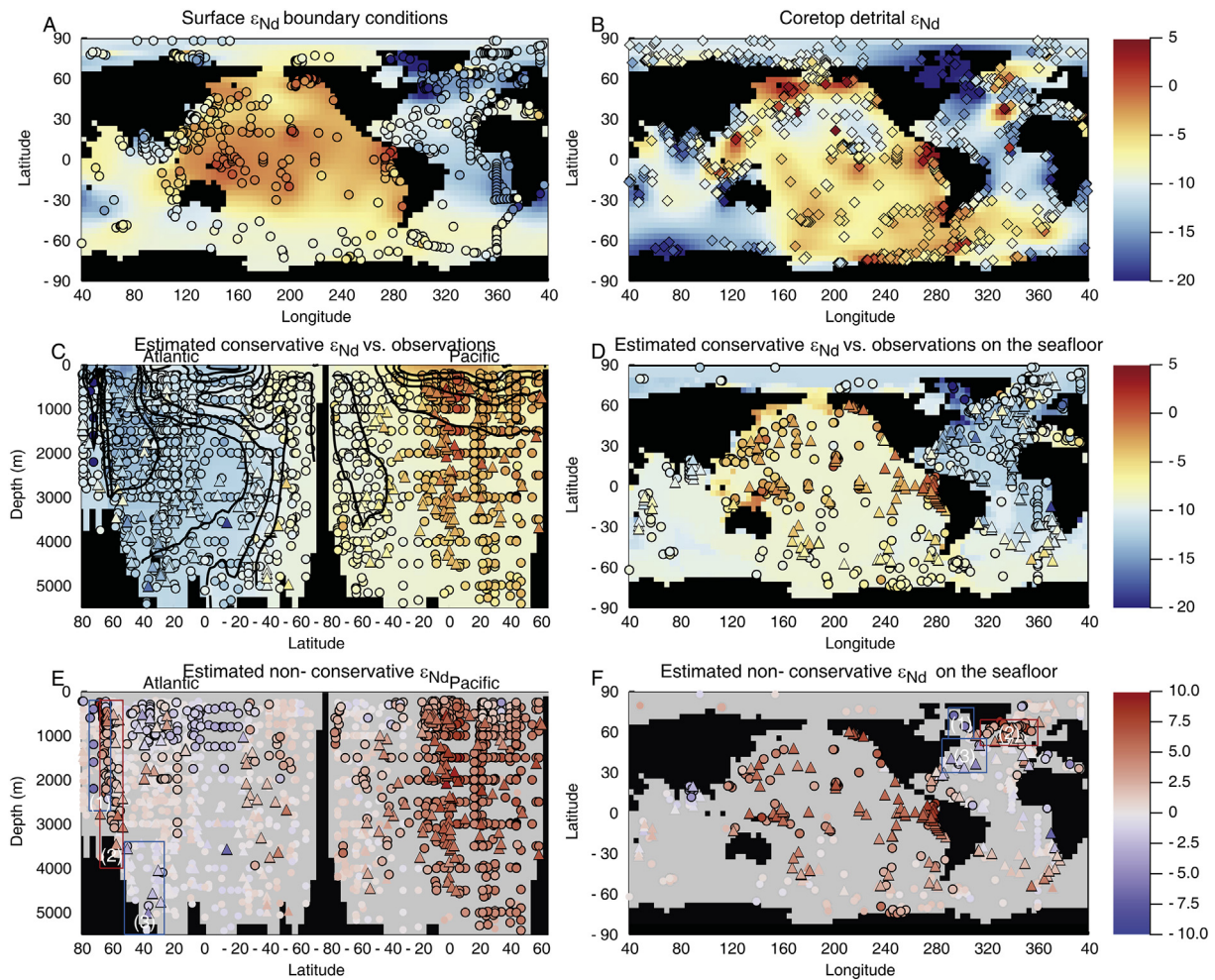


**Fig. 2.** Observations and estimated conservative and non-conservative components of  $\epsilon_{Nd}$  in the global ocean. Modern seawater, Holocene authigenic and coretop detrital data are marked by dots, triangles and diamonds respectively. In **A** symbols indicate surface water (<200 m) observations, and the background is the surface boundary condition used in TMI. In **B** symbols indicate coretop detrital sediment observations, and the background is interpolated data. In **C** symbols indicate modern seawater and Holocene authigenic observations plotted on the same section (i.e., longitudinal differences are ignored), and the background is the zonal-averages of estimated conservative component of  $\epsilon_{Nd}$  with contours shown in black lines (contour levels are from -13 to -5 by 1 unit). In **D** symbols indicate modern seawater and Holocene authigenic observations from within 500 m of the seafloor, and the background is the estimated conservative component of  $\epsilon_{Nd}$  on the bottommost grid. In **E** symbols indicate estimated non-conservative component of modern seawater and Holocene authigenic  $\epsilon_{Nd}$ . In **F** symbols indicate estimated non-conservative component of modern seawater and Holocene authigenic  $\epsilon_{Nd}$  from within 500 m of the seafloor. In **E** and **F**, symbols with black borders indicate non-conservative  $\epsilon_{Nd}$  that are statistically non-zero (95% CI) while those without borders are not. In **E** and **F**, three regions in the North Atlantic of interest are marked by boxes: (1) Baffin-Labrador Basins, (2) Iceland, and the (3) Benthic Nepheloid Layer linked to DWBC.

The estimated conservative  $\varepsilon_{\text{Nd}}$  product is then interpolated to interior  $\varepsilon_{\text{Nd}}$  observation locations ( $>200$  m), and the non-conservative  $\varepsilon_{\text{Nd}}$  is calculated as the difference between observed  $\varepsilon_{\text{Nd}}$  and estimated conservative  $\varepsilon_{\text{Nd}}$ . The uncertainties of this interpolating step as well as the analytical  $\varepsilon_{\text{Nd}}$  uncertainties (typically  $1\sigma \leq 0.2$ ) are neglected as the overall uncertainty is dominated by the uncertainties in generating the surface boundary conditions. We summarize the statistics of resulting non-conservative  $\varepsilon_{\text{Nd}}$  using medians and 95% confidence intervals (CI).

Finally, we perform the same analysis on the Holocene authigenic  $\varepsilon_{\text{Nd}}$  dataset, such that we can examine whether the non-conservative behavior of modern bottom seawater and Holocene authigenic  $\varepsilon_{\text{Nd}}$  are consistent. The non-conservative  $\varepsilon_{\text{Nd}}$  of the authigenic phase is defined as the difference between observed authigenic  $\varepsilon_{\text{Nd}}$  and estimated conservative  $\varepsilon_{\text{Nd}}$  of the overlying bottom water.

#### 2.4. Principal Component Analysis of paleo-authigenic times-series

We synthesize and resolve empirical spatial-temporal modes of global and regional authigenic  $\varepsilon_{\text{Nd}}$  variabilities in time-series records using PCA. A previous study has also performed PCA on deglacial  $\varepsilon_{\text{Nd}}$  records but with a smaller dataset (25 records) (Friedrich et al., 2014). Our compilation benefits from high resolution  $\varepsilon_{\text{Nd}}$  records from strategically important locations (deep Pacific, subpolar North Atlantic and deep Southern Ocean) that have only recently become available.

Authigenic records are first binned and averaged into 500-year intervals between 0 and 23 ka. The binned data form an  $n \times p$  matrix where  $n = 45$  is the number of age bins and  $p = 72$  is the number of sites. No single record has enough resolution and age range to fill all bins, and missing values in the data matrix are filled based on PCA imputation using a regularized iterative algorithm (Josse and Husson, 2016). With this method, missing data are estimated using the correlation structure of the entire dataset, so no artificial variance is introduced as may occur with within-site interpolation. We then perform covariance-based PCA on the completed data matrix such that the resulting loadings are scaled to the variance in the authigenic  $\varepsilon_{\text{Nd}}$  records.

Finally, we decompose each completed authigenic  $\varepsilon_{\text{Nd}}$  time-series into its PCs. This is useful because the PC scores only summarize the “common” signals shared by authigenic records in variance units. Decomposition recreates the records using the time-series of PC scores and their respective loadings at each site, thus putting these “common” signals back into each individual  $\varepsilon_{\text{Nd}}$  record (Lé et al., 2008). Mathematically, we use  $\mathbf{X}$  to denote the  $n \times p$  authigenic  $\varepsilon_{\text{Nd}}$  data matrix after missing value imputation.  $\mathbf{X}$  is first centered by removing column-means ( $\frac{1}{n} \sum_{m=1}^n \mathbf{X}_{m,i}$  is the mean  $\varepsilon_{\text{Nd}}$  of the  $i$ th site). PCA gives

$$\mathbf{S} = \mathbf{X}_c \mathbf{W} \quad (4)$$

where  $\mathbf{X}_c$  is centered data matrix.  $\mathbf{S}$  ( $n \times p$ ) is the score matrix, the columns of which are the time-series of PC scores ( $\mathbf{S}_{k,j}$  is the score of the  $j$ th PC in the  $k$ th age bin).  $\mathbf{W}$  ( $p \times p$ ) is the weighting matrix, the columns of which are the eigenvectors of matrix  $\mathbf{X}_c^T \mathbf{X}_c$  (T indicates transpose). The loadings of the  $i$ th site on the  $j$ th PC is thus  $\sqrt{\lambda_j} \mathbf{w}_{i,j}$  where  $\lambda_j$  is the  $j$ th eigenvalue of  $\mathbf{X}_c^T \mathbf{X}_c$ , i.e., the variance explained by the  $j$ th PC, corresponding to the eigenvector in the  $j$ th column of  $\mathbf{W}$ . The decomposed authigenic  $\varepsilon_{\text{Nd}}$  records, for example the  $j$ th PC of the  $i$ th site in the  $k$ th age bin in the original  $\varepsilon_{\text{Nd}}$  unit is thus

$$\hat{\mathbf{X}}_{k,i}^j = \hat{\mathbf{S}}_{k,j} \hat{\mathbf{W}}_{j,i}^T + \frac{1}{n} \sum_{m=1}^n \mathbf{X}_{m,i} \quad (5)$$

where hat symbol “ $\hat{\phantom{x}}$ ” indicates truncation, i.e., minor PCs explaining small portions of variances are truncated to attenuate noise or uncorrelated local signals. This reconstruction makes it relatively easy to assess visually how the PCA decomposition has captured the main features of the measured data at each site.

We assess the uncertainties on the PCA due to  $\varepsilon_{\text{Nd}}$  analytical uncertainty and age model limitations using a Monte-Carlo approach. The analytical uncertainty of  $\varepsilon_{\text{Nd}}$  is included by adding Gaussian white noise with a  $2\sigma$  of 0.3 (typical of most laboratories) to the original data matrix (the data matrix after binning but before imputation). We apply a fixed uncertainty typical of modern instruments because not all studies reported long-term external  $\varepsilon_{\text{Nd}}$  reproducibility. Second, the age model uncertainty is included by adding Gaussian white noise with a  $2\sigma$  of 500 years to original age models. We apply this fixed uncertainty because it is often not possible to assess the uncertainties of the published age models. This temporal uncertainty is larger than well-dated high-resolution records that are used to discuss the deglacial millennial events. We created 10,000 random realizations of each  $\varepsilon_{\text{Nd}}$  record (100 for  $\varepsilon_{\text{Nd}}$  uncertainty times 100 for age model uncertainty). The resulting data matrices with missing values are subjected to the imputation and PCA procedures described above. PC scores and decomposed  $\varepsilon_{\text{Nd}}$  records are summarized using medians and 95% CIs. Authigenic  $\varepsilon_{\text{Nd}}$  time-series and their PCs are plotted in [Supplementary Table S2](#).

### 3. A new framework for using $\varepsilon_{\text{Nd}}$ as a circulation tracer

#### 3.1. The modern ocean Nd- $\varepsilon_{\text{Nd}}$ budget

Using the box model, we perform sensitivity tests to constrain the modern Nd- $\varepsilon_{\text{Nd}}$  budget in regard to sedimentary fluxes. At this point in our understanding, we are interested in the global budget to a first-order, and thus assume that the sedimentary flux (per area) is constant (Arsouze et al., 2009). Although a simplification, this assumption is supported by the similarity of existing observations of benthic Nd fluxes, largely on the order of  $10 \text{ pmol cm}^{-2} \text{ yr}^{-1}$ , from diverse sedimentary environments ranging from terrigenous to calcareous (Fig. 1C) (Abbott, 2019; Abbott et al., 2015b; Du et al., 2018; Haley et al., 2004; Haley and Klinkhammer, 2003).

A key constraint on the global Nd- $\varepsilon_{\text{Nd}}$  budget is the global residence time of Nd with respect to the total external sources ( $\tau_{\text{Nd}}$ ), with recent studies converging to an estimate of 300–600 years (Abbott et al., 2015b; Arsouze et al., 2009; Du et al., 2018; Rempfer et al., 2011; Tachikawa et al., 2003). We performed a series of steady-state model experiments in which we varied the sedimentary flux and calculated the resulting  $\tau_{\text{Nd}}$ . In doing so, we find that a  $\tau_{\text{Nd}}$  of 300–600 years corresponds to a sediment flux of 20–30  $\text{pmol cm}^{-2} \text{ yr}^{-1}$  (Fig. 1B).

This box model estimate is derived by fitting the observations of global seawater Nd concentration and  $\varepsilon_{\text{Nd}}$  subject to steady-state mass balance (equations (1) and (2)). The box model is agnostic to the processes regulating the Nd sources. That the box model derived estimate agrees with existing area-weighted measurements of sediment Nd flux (Abbott et al., 2015b; Du et al., 2018; Haley et al., 2004; Haley and Klinkhammer, 2003), gives strong evidence that sedimentary flux can readily account for the “missing source” in global Nd- $\varepsilon_{\text{Nd}}$  budget (Abbott et al., 2015b; Arsouze et al., 2009; Tachikawa et al., 2003). Existing measurements of

sedimentary Nd flux have an arithmetic mean of  $13 (\pm 3, \text{ standard error}) \text{ pmol cm}^{-2} \text{ yr}^{-1}$  and seafloor area weighted mean of  $23 (\pm 7, \text{ standard error}) \text{ pmol cm}^{-2} \text{ yr}^{-1}$ , the latter being higher because measurements of sediment Nd flux (per area) increase slightly with increasing water depth, and because the deep ocean has a much greater fraction of seafloor area (Fig. 1C-D) (Abbott et al., 2015b; Du et al., 2018).

The observed increase in sediment Nd flux (per area) with increasing water depth does not include biologically induced non-diffusive transport (such as bio-irrigation) in the flux calculations, which may lead to underestimation of the flux on the shelf (Abbott et al., 2015b). Such biases however are likely small (Meile and Cappellen, 2003), in which case sediment Nd flux per area on the shelf might be on par with, but not much higher, than that of the deep ocean. Given that the range of measured sediment Nd fluxes (per area) is dwarfed by the depth-dependent variability of seafloor area, the depth-dependent total sediment Nd flux is mainly controlled by the hypsometry of ocean basins, which is strongly weighted toward the deep ocean (>2500m, Fig. 1D) (Du et al., 2018).

The relatively large deep-ocean benthic source for Nd contrasts other elements, such as carbon, oxygen, nutrients and iron, the benthic fluxes of which typically decrease with increasing water depth. This contrast further manifests in the lack of correlation between sediment Nd flux and sediment redox state indicated by organic carbon flux and bottom water oxygen concentration (Abbott et al., 2015b; Du et al., 2018). Sediment Nd flux therefore appears to be not a primary function of sedimentary Fe-Mn oxide reduction (German and Elderfield, 1989) (which may act as an intermediary rather than the ultimate source), but is instead limited by chemical weathering of lithogenic sediments at and below the sea floor. If so, the Nd flux from the sea floor is approximately stable on glacial-interglacial timescales (Abbott et al., 2019, 2015b; Du et al., 2018).

Other candidates of the “missing source” to satisfy the mass balance of observed global seawater Nd concentration and  $\epsilon_{\text{Nd}}$  include partial dissolution of detrital particles in the high salinity zones of river estuaries and ground water discharge, which are estimated to be in the ranges of  $2.2\text{--}5.8 \times 10^7 \text{ mol/yr}$  (Rousseau et al., 2015) and  $0.9\text{--}2.4 \times 10^7 \text{ mol/yr}$  (Johannesson and Burdige, 2007) respectively. Acknowledging that there are considerable uncertainties in these estimates as they are also derived from small observational datasets, both are smaller than estimated sediment Nd flux based on pore water sampling ( $7.9\text{--}10.3 \times 10^7 \text{ mol/yr}$  using the area weighted average). Moreover, there is not necessarily observational or mechanistic distinctions among these sources. For example, partial dissolution of detrital particles can happen throughout the estuary-shelf-slope-abyssal plain continuum and the reported benthic Nd flux on the shelf may already include ground water discharge. As the sum of these fluxes would imply a global Nd residence time of  $\sim 200$  years, which would likely be too short for  $\epsilon_{\text{Nd}}$  to have an observable global circulation structure, it seems likely that there are overlaps among these sources. Finally, Nd fluxes due to partial dissolution of detrital particles in riverine estuaries and ground water discharge, though potentially leading to much shorter effective Nd residence times in shallow waters close to the margins, are likely to have limited effects on the deep ocean Nd reservoir (Arsouze et al., 2009) that dominates the global ocean Nd- $\epsilon_{\text{Nd}}$  budget (Fig. 1D).

Although future work may definitively resolve the “missing source” problem, it remains that the greatest imbalance of the Nd- $\epsilon_{\text{Nd}}$  budget is in the deep ocean, especially the vast deep Pacific reservoir (Jones et al., 2008). We contend that sediment flux from deep sea sediments is the most likely candidate to resolve this imbalance, and available observations support this inference

(Abbott et al., 2015; Du et al., 2018).

At this stage of our understanding of the marine Nd cycle, we consider a globally average value of  $23 (\pm 7) \text{ pmol cm}^{-2} \text{ yr}^{-1}$  for sediment Nd flux to be suitable for deriving the Nd- $\epsilon_{\text{Nd}}$  budgets on the large spatial-temporal scales that are the focus of this study, but we caution the use of this number in regional studies as well as in shallow and intermediate water studies. Increasing the number of measurements of benthic flux and other sources, and improving the mechanistic understanding of the processes regulating such fluxes must be considered a high priority for future study, especially if we are to apply the  $\epsilon_{\text{Nd}}$  proxy on smaller spatial-temporal scales.

Adopting this estimate, globally surficial (dust and dissolved river fluxes) and sediment sources account for  $\sim 5\%$  and  $\sim 95\%$  of the external Nd source fluxes respectively (Table 1), in agreement with previous estimates (Tachikawa et al., 2003; Arsouze et al., 2009; Abbott et al., 2015b; Rempfer et al., 2011). Adding consideration for the redistribution of Nd within the ocean due to watermass transport, we estimate that surficial sources account for  $\sim 2\%$ , sediment sources accounts for  $\sim 40\%$  and watermass transport accounts for  $\sim 58\%$  of the total Nd fluxes (i.e., external sources plus internal fluxes due to transport). Considering the uncertainty in the area-weighted sediment Nd flux, the ratio of sediment flux to transport flux is  $0.7 \pm 0.2$  globally.

Balancing the modern Atlantic Nd- $\epsilon_{\text{Nd}}$  budget requires a sedimentary source with  $\epsilon_{\text{Nd}}$  more negative than basinal-average seawater  $\epsilon_{\text{Nd}}$ . The opposite is true for the Pacific. This contrast has been shown previously (Tachikawa et al., 2003). In the Atlantic, such a negative  $\epsilon_{\text{Nd}}$  source can readily come from sediments in the Labrador Basin and the Western Atlantic Basin (Fig. 2B) (Lacan and Jeandel, 2005b), where a high fraction of the detrital sediments is derived from Precambrian materials in the Canadian Shield ( $\epsilon_{\text{Nd}} < -25$ ). In the Pacific, the volcanic fraction ( $\epsilon_{\text{Nd}} > 0$ ) within detrital sediments offers a high  $\epsilon_{\text{Nd}}$  sedimentary source, consistent with pore water and authigenic studies (Abbott et al., 2015a; Du et al., 2016). This basin-scale Atlantic-Pacific contrast in detrital influence is also consistent with the understanding of detrital reactivity based on sediment leaching studies (Abbott et al., 2016; Blaser et al., 2016; Du et al., 2016).

### 3.2. Non-conservative Nd isotope behavior

Seawater  $\epsilon_{\text{Nd}}$  in the modern ocean is thought to be “quasi-conservative” rather than strictly conservative (Goldstein and Hemming, 2003; van de Flierdt et al., 2016), and here we quantify the non-conservative components of  $\epsilon_{\text{Nd}}$ .

The Nd- $\epsilon_{\text{Nd}}$  budget shows that globally the conservative contributions due to watermass transport and the non-conservative contributions originating from sediment sources are, at present, of the same order of magnitude (Table 1), explaining the quasi-conservative properties of  $\epsilon_{\text{Nd}}$ . On basinal scales, transport has greater proportional effect on  $\epsilon_{\text{Nd}}$  in the Atlantic, while sediment source is the dominant term controlling  $\epsilon_{\text{Nd}}$  in the Pacific (Table 1). This difference in the relative strength of non-conservation in Atlantic and Pacific is attributed to the difference of water residence time  $\tau_w$  in these two basins.

The steady-state solution of  $\epsilon_{\text{Nd}}$  in any ocean box (ignoring the small surface sources) can be broken down into two terms (Du et al., 2018):

$$\epsilon_{\text{Nd}} = \frac{\tau_w}{\tau_w + \tau_{\text{Nd}}} \epsilon_{\text{Nd}}^{\text{S}} + \frac{\tau_{\text{Nd}}}{\tau_w + \tau_{\text{Nd}}} \sum m^i \epsilon_{\text{Nd}}^i \quad (6)$$

where the first is the sediment source or the non-conservative term ( $\epsilon_{\text{Nd}}^{\text{S}}$  is the isotope composition of the sediment source) and the

**Table 1**  
Modern global Nd- $\epsilon_{Nd}$  budget. Each individual ocean basin has four sources of Nd: dust, river (dissolved), sediment flux and transport in (Nd carried by waters entering the box). These sources are balanced by two sinks: scavenging and transport out (Nd carried by waters leaving the box). Note that transport only distributes Nd among the ocean basins and does not provide a net sink/source globally. Only dust, river and sediment flux are external sources and scavenging is the only external sink. In the model the scavenging flux is scaled to [Nd] and the first order rate law constant  $k$  is reported here. The  $\epsilon_{Nd}$  of the scavenging flux is the same as seawater. At the end of the table we report the percentage of the individual sources with respect to the external sources (%ES) and the total sources (%TS, i.e., external sources plus transport in).

| Basin                           | Atlantic | Pacific  | Indian   | Southern | Global   |
|---------------------------------|----------|----------|----------|----------|----------|
| Seawater [Nd] (pmol/kg)         | 24.9     | 32.0     | 29.6     | 26.7     | 28.8     |
| Seawater $\epsilon_{Nd}$        | -12.1    | -4.3     | -9.3     | -8.3     | -7.2     |
| Seafloor area (m <sup>2</sup> ) | 6.06E+13 | 1.31E+14 | 3.81E+13 | 1.08E+14 | 3.38E+14 |
| Volume (m <sup>3</sup> )        | 2.26E+17 | 5.25E+17 | 1.42E+17 | 4.16E+17 | 1.31E+18 |
| Dust flux (mol/yr)              | 4.01E+05 | 1.48E+05 | 2.01E+05 | 6.68E+04 | 8.17E+05 |
| Dust flux $\epsilon_{Nd}$       | -12.5    | -6.0     | -6.0     | -8.0     | -9.4     |
| River flux (mol/yr)             | 2.35E+06 | 7.59E+05 | 2.70E+05 | 0        | 3.38E+06 |
| River flux $\epsilon_{Nd}$      | -12.6    | -2.9     | -8.7     | NA       | -10.1    |
| Transport in (mol/yr)           | 1.95E+07 | 1.68E+07 | 2.36E+07 | 5.14E+07 | 1.11E+08 |
| Transport in $\epsilon_{Nd}$    | -8.1     | -8.3     | -6.6     | -9.4     | -8.4     |
| Transport out (mol/yr)          | 1.81E+07 | 2.02E+07 | 2.42E+07 | 4.88E+07 | 1.11E+08 |
| Sediment flux (mol/yr)          | 1.39E+07 | 3.02E+07 | 8.76E+06 | 2.49E+07 | 7.78E+07 |
| Sediment flux $\epsilon_{Nd}$   | -17.8    | -2.1     | -16.7    | -5.9     | -7.8     |
| Scavenging flux (mol/yr)        | 1.81E+07 | 2.78E+07 | 8.55E+06 | 2.75E+07 | 8.20E+07 |
| $k$ (yr <sup>-1</sup> )         | 3.23E-03 | 1.66E-03 | 2.04E-03 | 2.48E-03 | 2.17E-03 |
| External sources (mol/yr)       | 1.67E+07 | 3.11E+07 | 9.23E+06 | 2.50E+07 | 8.20E+07 |
| Total sources (mol/yr)          | 3.62E+07 | 4.80E+07 | 3.28E+07 | 7.64E+07 | 1.93E+08 |
| %ES Sediment                    | 83.5%    | 97.1%    | 94.9%    | 99.7%    | 94.9%    |
| %ES Dust and River              | 16.5%    | 2.9%     | 5.1%     | 0.3%     | 5.1%     |
| %TS Sediment                    | 38.5%    | 63.0%    | 26.7%    | 32.6%    | 40.2%    |
| %TS Transport in                | 53.9%    | 35.1%    | 71.9%    | 67.3%    | 57.6%    |
| %TS Dust and River              | 7.6%     | 1.9%     | 1.4%     | 0.1%     | 2.2%     |

second is the conservative mixing term ( $m^i$  and  $\epsilon_{Nd}^i$  are the mixing ratio and isotope composition of the source waters, i.e., the pre-formed  $\epsilon_{Nd}$ ). Critically, greater  $\tau_w/\tau_{Nd}$  implies stronger expression of the sediment influence.

Our quantification of the non-conservative  $\epsilon_{Nd}$  components in the modern ocean come from the TMI, which propagates surface water  $\epsilon_{Nd}$  signatures into the ocean interior through circulation. Deviation of observed modern seawater and Holocene authigenic  $\epsilon_{Nd}$  from this conservatively mixed  $\epsilon_{Nd}$  indicates that non-conservative processes must modify  $\epsilon_{Nd}$  in the ocean interior. This modification could happen on the seafloor and/or in the water column, and the resulting non-conservative  $\epsilon_{Nd}$  components are integrated values along the circulation pathway, which is sensitive to the large-scale isotopic character of the non-conservative Nd source, but not necessarily to specific small-scale local isotopic source.

Globally, the non-conservative  $\epsilon_{Nd}$  is well correlated to coretop detrital sediment  $\epsilon_{Nd}$  (Figs. 2 and 3A), as predicted by the bottom-up hypothesis (Abbott et al., 2016; Abbott et al., 2015a; Du et al., 2016). In the Pacific, consistently positive non-conservative  $\epsilon_{Nd}$ , up to  $>+7$ , indicates volcanic sedimentary input (Abbott et al., 2016; Abbott et al., 2015a; Behrens et al., 2018; Du et al., 2016) (Fig. 2E and F). In the Atlantic, the non-conservative behavior is generally weaker than in the Pacific but clearly identifiable. More evident examples include (Fig. 2E and F): a strong negative non-conservative  $\epsilon_{Nd}$  ( $\sim-5$ ) in the Baffin-Labrador Basin where sediments are partially sourced from the Canadian Shield (Filippova et al., 2017; Lacan and Jeandel, 2005b); a strong positive non-conservative  $\epsilon_{Nd}$  ( $\sim+5$ ) around Iceland, reflecting basaltic sources (Morrison et al., 2018); a pattern of consistent negative non-conservative  $\epsilon_{Nd}$  ( $\sim-3$ ) in the deep western North Atlantic that corresponds to the thick and persistent Benthic Nepheloid Layer in this region (Gardner et al., 2018; Pöppelmeier et al., 2019), where suspended sediments are likely transported from the Labrador Basin via the Deep Western Boundary Current (DWBC) (Grousset and Biscaye, 2005).

Other regional non-conservative examples include (Fig. 2F): a positive non-conservative  $\epsilon_{Nd}$  in the Caribbean due to local volcanic

sediments (Osborne et al., 2014); a negative non-conservative source signature for  $\epsilon_{Nd}$  in the Angola Basin consistent with local detrital sediments (Rahlf et al., 2019); a positive non-conservative source signature for  $\epsilon_{Nd}$  in the Pacific and Atlantic sectors of the Southern Ocean where local Antarctic sourced detrital sediments have radiogenic  $\epsilon_{Nd}$  (Carter et al., 2012; Lambelet et al., 2018), and a negative non-conservative signature for  $\epsilon_{Nd}$  in the Bay of Bengal due to unradiogenic detritus from the Himalayans (Yu et al., 2017).

These results also confirm the “aging effect” predicted by the bottom-up hypothesis: longer benthic exposure time will lead seawater and authigenic  $\epsilon_{Nd}$  to converge toward regional (reactivity-weighted) detrital sediment  $\epsilon_{Nd}$  (Abbott et al., 2015a; Du et al., 2016; Osborne et al., 2014). To illustrate this effect, we substitute ideal watermass mean age (i.e., the time since leaving the sea surface) (Gebbie and Huybers, 2012) for benthic exposure time (though rigorous quantification of benthic exposure time along flow pathways will be necessary for 3-dimensional models). In the Pacific, the aging effect reflects a more homogenous detrital sediment  $\epsilon_{Nd}$  of mainly volcanic origin such that the non-conservative  $\epsilon_{Nd}$  trends only toward radiogenic values (Figs. 3C and 2B). In contrast, the aging effect in the Atlantic has both positive and negative  $\epsilon_{Nd}$  trends, reflecting the heterogeneity in basinal sedimentary sources (Figs. 3C and 2B): An aging trend toward more negative non-conservative  $\epsilon_{Nd}$  indicates sedimentary input of Canadian Shield origin and is mainly developed along the pathway of DWBC in the western basin; The expression of the aging effect due to sedimentary influence of Iceland basalt origin is limited because the extent of such sediments is spatially restricted near the location of NSW formation today and thus mainly young waters acquire the corresponding non-conservative behavior. Overall, our analysis suggests that the aging trend toward negative non-conservative  $\epsilon_{Nd}$  is dominant on the basinal-average basis in the Atlantic (Table 1). The limited expression of non-conservative behavior of  $\epsilon_{Nd}$  in the Atlantic is not caused by a lack of sedimentary source, but by short benthic exposure time relative to circulation timescales, i.e., in the basin, smaller  $\tau_w/\tau_{Nd}$  means that conservative mixing dominates today. This does not need to have been the case in the past, for example if the circulation slowed and  $\tau_w$  became longer.

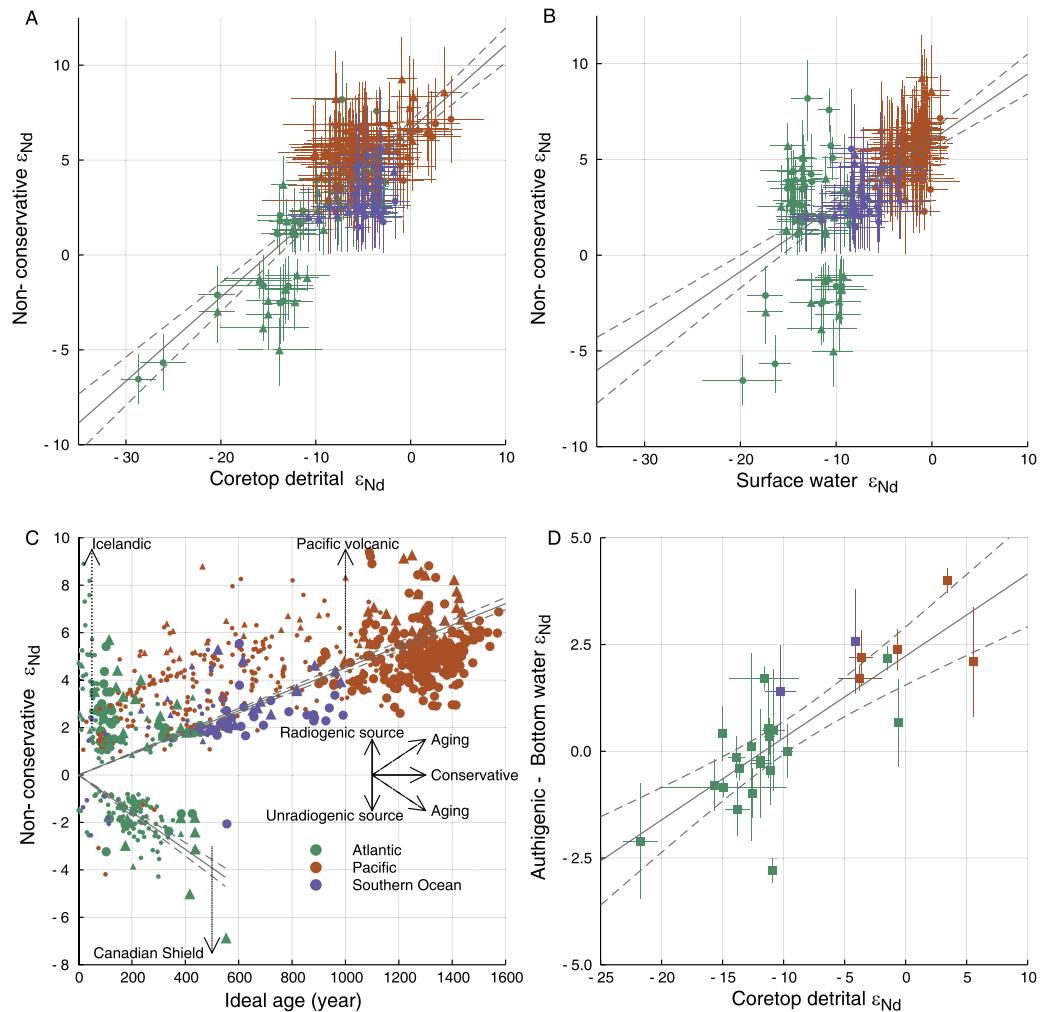


**Fig. 3.** The cause of the non-conservative component of modern seawater and Holocene authigenic  $\epsilon_{\text{Nd}}$  and its implication. **A** and **B**: Comparison of estimated non-conservative component of modern seawater (dots) and Holocene authigenic (triangles)  $\epsilon_{\text{Nd}}$  on the seafloor (within 500 m) with underlying coretop detrital sediment  $\epsilon_{\text{Nd}}$  (**A**) and overlying surface water  $\epsilon_{\text{Nd}}$  (**B**). Non-conservative  $\epsilon_{\text{Nd}}$  are from Fig. 2F. Detrital and surface  $\epsilon_{\text{Nd}}$  are interpolated values at corresponding locations using data in Fig. 2B and A respectively.  $R^2$  of linear regression are 0.6 ( $p \ll 0.05$ ) in **A** and 0.4 ( $p \ll 0.05$ ) in **B**. If the regression is only performed on the Atlantic data, then  $R^2$  are 0.7 ( $p \ll 0.05$ ) and 0.002 ( $p = 0.7$ ) respectively in **A** and **B**. **C**: Comparison of estimated non-conservative component of modern seawater and Holocene authigenic  $\epsilon_{\text{Nd}}$  (all data included) with circulation ideal age, approximating benthic exposure time. Non-conservative  $\epsilon_{\text{Nd}}$  are from Fig. 2E and F and circulation age are interpolated values at corresponding locations (Gebbie and Huybers, 2012).  $R^2$  of linear regression is 0.8 ( $p \ll 0.05$ ) for both the positive and negative trends. In **A–C** only non-conservative  $\epsilon_{\text{Nd}}$  that are statistically non-zero are used; colors indicate basins. In **C** bigger symbols indicate deep ocean data (>1500 m) while smaller symbols indicate intermediate depth data (500–1500 m). **D**: Comparison of the  $\epsilon_{\text{Nd}}$  offset between Holocene authigenic phase and overlying modern bottom water (within 500 m of seafloor) with underlying coretop detrital  $\epsilon_{\text{Nd}}$ . Raw authigenic, bottom water and detrital data are first binned into  $5^\circ \times 5^\circ$  boxes, generating paired data sets. The box-averaged values are used to calculate the authigenic-bottom water offset, plotted against paired box-average detrital values.  $R^2$  of linear regression is 0.7 ( $p \ll 0.05$ ).

An important outcome of considering a bottom-up source of non-conservative behavior of  $\epsilon_{\text{Nd}}$  is the ability to explain differences between modern bottom water and Holocene authigenic  $\epsilon_{\text{Nd}}$  (Fig. 3D). Such differences exist globally and are identified in all types of archives including apatite derived from fish debris and Fe-Mn oxides associated with foraminifera and bulk sediments (Blaser et al., 2016; Du et al., 2016; Elmore et al., 2011; Horikawa et al., 2011). While some of those differences, especially regarding dispersed Fe-Mn oxides extracted from bulk sediments, may reflect leaching procedures that cause detrital contamination during lab extraction, rigorous leaching procedures in recent studies have revealed *genuine* differences that must be caused by *in-situ* sedimentary processes (Blaser et al., 2016; Du et al., 2016; Elmore et al., 2011; Horikawa et al., 2011). Our bottom-up model specifies that bottom water and authigenic phases *may* have the same  $\epsilon_{\text{Nd}}$ , not

only because authigenic phases inherit a bottom water signature (Gutjahr et al., 2007; Roberts et al., 2012; Tachikawa et al., 2014), but because the bottom water signature is strongly influenced by the authigenic phases, which impart the sedimentary influence on bottom water through pore water interactions, and authigenic  $\epsilon_{\text{Nd}}$  is thus subject to greater sedimentary influence and inherently more non-conservative than seawater  $\epsilon_{\text{Nd}}$ . (Abbott et al., 2016, Abbott et al., 2015a; 2015b; Du et al., 2016; Haley et al., 2017).

Our analysis implies that the non-conservative behavior of  $\epsilon_{\text{Nd}}$  is not limited to the continental margins and shallow depths, but evident in the deep open ocean too, consistent with observed high benthic Nd flux from deep-sea sediments (Abbott, 2019; Abbott et al., 2015b; Haley and Klinkhammer, 2003). We stress, however, that these influences have variable impact on a given watermass depending on many factors (e.g., proximity to the seafloor). The

bottom-up framework is consistent with observed correlations between  $\epsilon_{\text{Nd}}$  and other tracers (Tachikawa et al., 2017), as the non-conservative component is also propagated by circulation just as the conservative component is. Demonstration of the (non-) conservative aspects of  $\epsilon_{\text{Nd}}$  by correlating it to other tracers, such as nutrients, requires first decomposing these tracers into conservative and non-conservative components as is done using TMI (Gebbie and Huybers, 2010) or other methods (Haley et al., 2014; Zheng et al., 2016).

The watermass  $\epsilon_{\text{Nd}}$  endmembers commonly used in conservative mixing calculations are partially set by sedimentary sources too, and thus non-conservative properties are propagated into the ocean interior when performing fixed-endmember mixing calculations. The preformed  $\epsilon_{\text{Nd}}$  of NADW's precursor watermasses, Labrador Sea Water (LSW) and Nordic Sea Overflow Water (NSOW), cannot be set solely through subduction of surface water  $\epsilon_{\text{Nd}}$  signatures; both require inputs from local sedimentary sources (Lacan and Jeandel, 2005b, 2004a; 2004b) which give LSW and NSOW contrasting "preformed"  $\epsilon_{\text{Nd}}$  ( $\sim -14$  vs.  $\sim -8$ , van de Flierdt et al. (2016)). These precursor watermasses then mix to form the preformed  $\epsilon_{\text{Nd}}$  of NADW ( $\sim -13$ ) (Lambelet et al., 2016; Piepgras and Wasserburg, 1987, 1980, 1982) with further sedimentary modification along the circulation pathway (Fig. 2F). In the subtropical North Atlantic, NADW loses contact with the underlying abyssal seafloor where AABW is present, and at that point, the non-conservative impact on NADW is diminished, relative to conservative mixing with AABW (Haley et al., 2017).

PDW cannot acquire its highly radiogenic  $\epsilon_{\text{Nd}}$  ( $\sim -4$ ) (Piepgras and Jacobsen, 1988; van de Flierdt et al., 2016) through subduction of surface waters given the lack of deep water formation in the North Pacific. Instead, the PDW  $\epsilon_{\text{Nd}}$  signature can be acquired at depth by interacting with volcanic sediments along the northward flow path of bottom waters in the abyssal Pacific (Abbott et al., 2016, Abbott et al., 2015a; Behrens et al., 2018; Du et al., 2016; Haley et al., 2017).

Similarly, the  $\epsilon_{\text{Nd}}$  endmember of AABW ( $\sim -8$ ) (Piepgras and Wasserburg, 1982; van de Flierdt et al., 2016) is not the result of solely mixing the unradiogenic NADW and the radiogenic PDW. Instead, systematic non-conservative behavior identified around Antarctic (Carter et al., 2012; Lambelet et al., 2018) indicates sedimentary impact on this endmember too.

Previous studies suggested that the non-conservative behavior of Nd may be attributed to reversible scavenging associated with particles in the water column rather than at the seafloor (Siddall et al., 2008). This top-down explanation has the following disadvantages compared with the bottom-up hypothesis: (1) reversible scavenging redistributes Nd between the surface and deep oceans but does not introduce *net* Nd sources to the global ocean which is required to balance the modern Nd budget (Arsouze et al., 2009); (2) the estimated non-conservative  $\epsilon_{\text{Nd}}$  is not well correlated to surface water  $\epsilon_{\text{Nd}}$  as predicted by reversible scavenging, especially

in the Atlantic (Fig. 3B). Rather, the stronger correlation to sea floor detrital sediment  $\epsilon_{\text{Nd}}$  (Fig. 3A) suggests a bottom-up control. The weaker correlation of non-conservative  $\epsilon_{\text{Nd}}$  to surface water  $\epsilon_{\text{Nd}}$  likely simply reflects the dominating control of overarching geology on global scales.

### 3.3. Implications for authigenic $\epsilon_{\text{Nd}}$ as a paleo-circulation tracer

We summarize the new framework of using  $\epsilon_{\text{Nd}}$  as an abyssal circulation tracer schematically (Fig. 4). Seawater/authigenic  $\epsilon_{\text{Nd}}$  should be interpreted taking into account three dominant components (Du et al., 2018): the preformed  $\epsilon_{\text{Nd}}$  of watermasses inherited from detrital sources at the locations of deep water formation; the conservative mixing of watermasses with distinct preformed  $\epsilon_{\text{Nd}}$ ; and the non-conservative effect as a function of benthic exposure time and detrital sediment composition. Incorporating the bottom-up view of  $\epsilon_{\text{Nd}}$  carries six key implications for paleoceanography, as follows:

- (1) On global and basinal scales, the distribution of detrital sediment  $\epsilon_{\text{Nd}}$  is heterogeneous and effectively sets the "blueprint" for seawater and authigenic  $\epsilon_{\text{Nd}}$ . Circulation acts to smooth out this heterogeneity through watermass mixing. Faster circulation (lower benthic exposure time) would tend to homogenize  $\epsilon_{\text{Nd}}$  in the water column and authigenic sediments, while slower circulation (higher benthic exposure time) would allow seawater and authigenic  $\epsilon_{\text{Nd}}$  to converge toward equilibrium with local detrital sediment  $\epsilon_{\text{Nd}}$ .
- (2) The temporal variability of detrital sediment  $\epsilon_{\text{Nd}}$  should be evaluated before interpreting authigenic  $\epsilon_{\text{Nd}}$  records, because of potential local imprints in the sediment system (Blaser et al., 2019; Du et al., 2016). Ideal sites for assessing changes in bottom water  $\epsilon_{\text{Nd}}$  as a function of watermass mixing and ocean circulation rate have a relatively constant detrital background. Changes of detrital  $\epsilon_{\text{Nd}}$  do not necessary preclude the use of authigenic  $\epsilon_{\text{Nd}}$  to reconstruct circulation if detrital influence is minor, or can be corrected for. Authigenic  $\epsilon_{\text{Nd}}$  records are best interpreted together with detrital records on *global to basinal* scales for robust circulation inference, whereas *local* heterogeneity of authigenic and detrital variability can be recognized against the global and basinal background. Concurrent measurements of authigenic and detrital  $\epsilon_{\text{Nd}}$  in the same samples are recommended.
- (3) Highly heterogeneous detrital sediment compositions in the North Atlantic implies that the preformed  $\epsilon_{\text{Nd}}$  of NSW rests upon a relative weighting of the highly unradiogenic Canadian Shield and the highly radiogenic Icelandic Basalt Nd sources: a situation that is likely to have changed over time (Goldstein and Hemming, 2003), for example through sensitivity to the locations and pathways of deep water

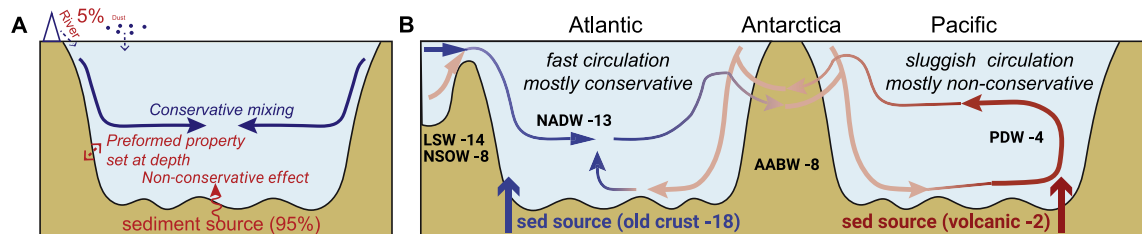


**Fig. 4.** Schematics for the modern global Nd- $\epsilon_{\text{Nd}}$  budget and its relation to the GOC. **A:** The revised budget including the effect of sedimentary flux on the preformed and non-conservative  $\epsilon_{\text{Nd}}$ . **B:** The modern Nd- $\epsilon_{\text{Nd}}$  budget superimposed on the GOC, with the emphases on Atlantic-Pacific contrast and GOC connection through the Southern Ocean (Talley, 2013). The modern Nd budget derived in this study is dominated by the deep ocean and thus intermediate water Nd budget is not shown.

formation, and the mixing of local sources to form a coherent deep water mass (Lacan and Jeandel, 2005b).

- (4) The partition of non-conservative and conservative  $\epsilon_{Nd}$  components is circulation dependent (Du et al., 2018). It cannot be assumed that conservative behavior of  $\epsilon_{Nd}$  always dominated in the Atlantic when the AMOC was much weaker in the past. Conversely, Pacific  $\epsilon_{Nd}$  cannot be assumed to always be dominated by non-conservative influences, e.g., if the SOMOC strengthened and reduced benthic exposure time compared to today.
- (5) The non-conservative component of  $\epsilon_{Nd}$  can be used to reconstruct abyssal circulation rate which controls benthic exposure time (Abbott et al., 2015a). Reconstructions can be done quantitatively via separation of the non-conservative component using budget-constrained models assuming stable sedimentary Nd fluxes, especially in the Pacific where only a single aging trend exists (Du et al., 2018, 2016). It can also be done qualitatively by considering the expression of the heterogeneity of detrital influence on seawater and authigenic  $\epsilon_{Nd}$ , e.g., given the same distribution of detrital sediment  $\epsilon_{Nd}$ , more heterogeneous seawater and authigenic  $\epsilon_{Nd}$  would indicate more sluggish circulation.
- (6) Authigenic  $\epsilon_{Nd}$  is a unique bottom-up tracer fundamentally different from top-down tracers, such as salinity, nutrients, oxygen and carbon isotopes, whose preformed properties are dominantly set at the surface ocean and whose marine cycling are dominated by upper ocean processes (Abbott et al., 2015a; Du et al., 2016; Haley et al., 2017). The bottom origin of preformed properties and non-conservativeness of  $\epsilon_{Nd}$  makes it sensitive to changes in abyssal circulation which may be difficult for top-down tracers to detect (de Lavergne et al., 2017), particularly when the bottom boundary conditions are less variable than the surface boundary conditions as one would expect is inherently the case in the oceans (Du et al., 2018).

#### 4. Paleo-authigenic $\epsilon_{Nd}$ records and non-circulation influence

##### 4.1. PCA results

PCA describes the empirical spatial-temporal modes of authigenic  $\epsilon_{Nd}$  variation since the LGM, finding large-scale patterns common to the full array of records, while attenuating uncorrelated noise or local anomalies. Two orthogonal PCs explain ~92% of the total variance (PC1 and PC2 contribute 86% and 6% respectively) (Fig. 5). PC1 mainly describes the LGM to Holocene change, with a relatively smooth transition between these states from ~19 ka to ~10 ka, followed by a slight but significant rebound in mid-to-late Holocene time. PC2 reveals deglacial anomalies peaking near ~16 ka and ~12 ka, roughly coeval with Heinrich Stadial 1 (HS1) and Younger Dryas (YD) events respectively.

In the following discussion, we use PCA decomposed  $\epsilon_{Nd}$  instead of PCA loadings for easier interpretation. The decomposed records are show in Supplementary Table S2. To illustrate the spatial pattern of PC1 loadings, we use the LGM-Holocene difference of the PC1  $\epsilon_{Nd}$  record, calculated as the difference between the average PC1  $\epsilon_{Nd}$  values of these two time-slices (19–23 ka and 0–6 ka respectively). The LGM-Holocene difference of the PC1  $\epsilon_{Nd}$  record and the LGM-Holocene difference of the original  $\epsilon_{Nd}$  record (raw data) are similar, because PC1 dominates the total variance.

To illustrate the spatial pattern of PC2 loadings, we use the deglacial anomaly of the PC2  $\epsilon_{Nd}$ , defined as the HS1-LGM difference of the PC2  $\epsilon_{Nd}$  record and calculated as the difference between the most extreme PC2  $\epsilon_{Nd}$  value in the HS1 time-slice (15–18 ka) and the average PC2  $\epsilon_{Nd}$  value of the LGM time-slice. Alternatively, we

could use the PC2  $\epsilon_{Nd}$  anomaly with respect to the Holocene or using YD instead of HS1 in the definition of deglacial anomaly, but all these definitions produce the same spatial pattern. We stress that the deglacial anomaly defined using HS1-LGM difference of the PC2  $\epsilon_{Nd}$  record differs from the HS1-LGM difference of the original  $\epsilon_{Nd}$  record (raw data), because in the PC2 based deglacial HS1-LGM comparison PC1 has been removed from the original record.

##### 4.2. Temporal detrital imprints on authigenic $\epsilon_{Nd}$ records

Our interpretations of the authigenic records and PCA patterns begin with identifying temporally variable “local” detrital imprints that may have affected the authigenic  $\epsilon_{Nd}$  records, as these detrital imprints may be superimposed on, or overwhelm, circulation imprints. Unfortunately, paired authigenic-detrital  $\epsilon_{Nd}$  data are relatively rare (Du et al., 2018; Hu and Piotrowski, 2018; Pöppelmeier et al., 2020; Struve et al., 2019; Zhao et al., 2019), and high resolution detrital  $\epsilon_{Nd}$  records are particularly scarce. As such, we focus on well-studied regions and take advantage of other detrital composition proxies when necessary.

###### 4.2.1. Global and basinal changes

We find no consistent changes of detrital sediment  $\epsilon_{Nd}$  that parallel the authigenic  $\epsilon_{Nd}$  on global and basinal scales (Fig. 6A). PC1 reveals that authigenic  $\epsilon_{Nd}$  is more positive in the LGM almost everywhere, especially in the deep ocean which dominates the global Nd budget, and this pattern is not mirrored in the detrital data. In most areas, detrital  $\epsilon_{Nd}$  changed little and thus for most records we conclude that authigenic  $\epsilon_{Nd}$  changes reflect circulation changes, albeit with potentially temporally constant offsets (Du et al., 2018, 2016; Pöppelmeier et al., 2020, 2019). In the Equatorial Pacific, the North Atlantic IRD belt and North Indian Ocean, however, detrital  $\epsilon_{Nd}$  varies significantly, and here authigenic  $\epsilon_{Nd}$  partially tracks detrital  $\epsilon_{Nd}$ . We address each of these areas as examples of local influences in the following.

###### 4.2.2. Equatorial Pacific

Equatorial Pacific  $\epsilon_{Nd}$  has been used to suggest that deep Pacific circulation strengthened during the LGM, based on more negative  $\epsilon_{Nd}$  in the LGM than the Holocene (Hu and Piotrowski, 2018). However, the global data shows that the Equatorial Pacific authigenic records are anomalous relative to the global authigenic patterns of change or to records from elsewhere in the deep Pacific (Fig. 6B; upper panel). The authigenic  $\epsilon_{Nd}$  records of the Equatorial Pacific track detrital  $\epsilon_{Nd}$ , suggesting a local imprint of changing detrital sources (Reimi and Marcantonio, 2016; Xie and Marcantonio, 2012). To illustrate the potential for correcting authigenic  $\epsilon_{Nd}$  records impacted by local detrital changes, we subtracted the change of local detrital  $\epsilon_{Nd}$  (with respect to Holocene) from authigenic  $\epsilon_{Nd}$  data. Such a hypothetically “corrected” Equatorial Pacific authigenic  $\epsilon_{Nd}$  data would conform to the rest of the Pacific records and would fit the global pattern of PC1 (Fig. 6B; lower panel). This correction, while encouraging, is crude and future work may facilitate more rigorous process-based corrections once the mechanisms of detrital impact on pore waters are better understood.

###### 4.2.3. Ice-rafted debris belt in the North Atlantic

Millennial scale detrital  $\epsilon_{Nd}$  variations in HLs are documented in the subpolar North Atlantic, for example in the ice-rafted debris (IRD) belt at 40–50°N (Fig. 5D, F) (Hemming, 2004; Ruddiman, 1977). Highly unradiogenic detrital  $\epsilon_{Nd}$  implies that the HL1 sediment in the IRD belt was sourced from the Canadian Shield (Hemming, 2004) (Fig. 7A). Further north, where IRD counts are

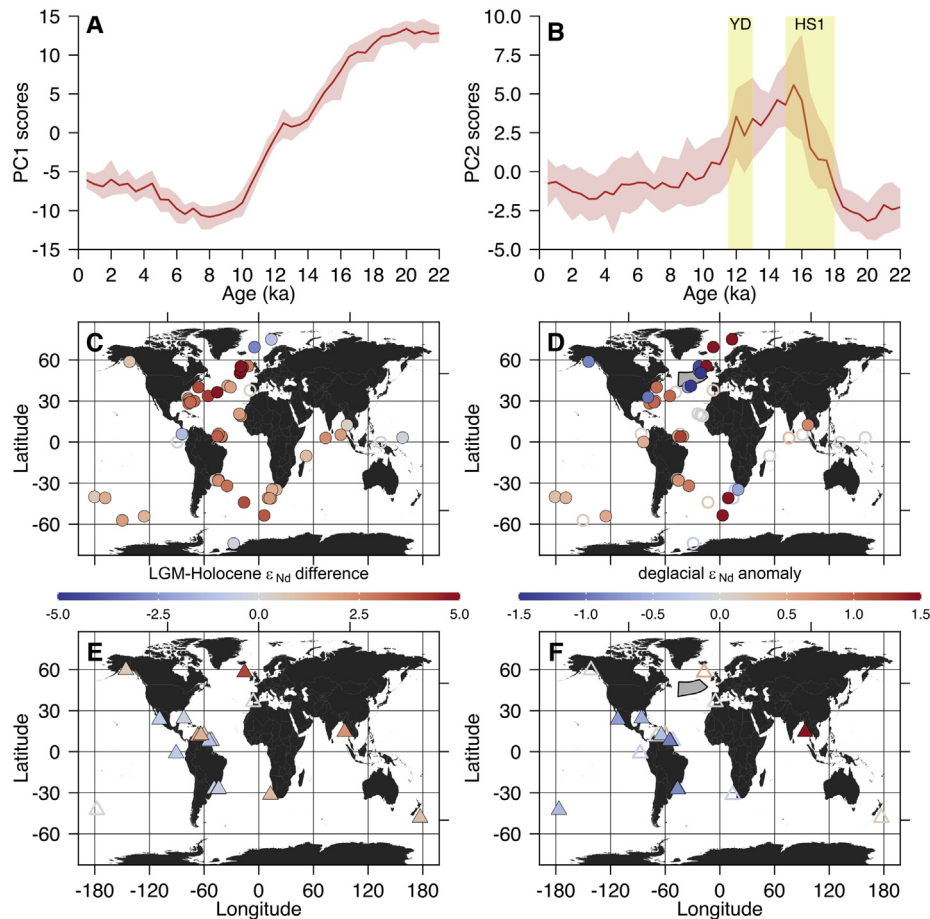


**Fig. 5.** Principal components of authigenic  $\epsilon_{Nd}$ . **A:** PC1 scores (shading is 95% CI, unitless). **B:** PC2 scores. **C:** LGM-Holocene difference of PC1  $\epsilon_{Nd}$  records from deep sites (circles, >1500 m). **D:** Deglacial  $\epsilon_{Nd}$  anomalies, i.e., HS1-LGM difference of PC2  $\epsilon_{Nd}$  records, from deep sites. **E and F:** Same as **C** and **D** but from intermediate-depth sites (triangles, 500–1500 m). The signs of the PC scores and LGM-Holocene  $\epsilon_{Nd}$  differences and deglacial  $\epsilon_{Nd}$  anomalies are consistent (i.e., positive scores correspond to positive differences/anomalies). Filled symbols in **C**, **D**, **E** and **F** indicate PC loadings that are significantly different from zero (95% CI); open symbols are not. The grey shaded area in the North Atlantic in **D** and **F** is the classic IRD belt associated with Heinrich Events (Hemming, 2004).

generally lower, radiogenic detrital  $\epsilon_{Nd}$  points to material from Icelandic sources of detritus supplied during HL1 (Revel et al., 1996).

The spatial pattern of HS1 authigenic anomalies in the classic IRD belt and north of it toward Iceland resembles that of HL1 detrital  $\epsilon_{Nd}$  (Fig. 7A and B), suggesting detrital imprints occurred on authigenic  $\epsilon_{Nd}$  at this time in this region. Such imprints are seen more clearly after decomposing authigenic  $\epsilon_{Nd}$  records into their PC1 (Fig. 7C and D) and PC2 (Fig. 7E and F) components. While PC1  $\epsilon_{Nd}$  clearly tracks the global authigenic trend on glacial-interglacial timescale (Figs. 5A and 6A), PC2  $\epsilon_{Nd}$  correlates well with the local IRD abundance on millennial timescale, but in opposite directions. In the classic IRD belt negative shifts of authigenic  $\epsilon_{Nd}$  during stadial events correlate to negative shifts of detrital  $\epsilon_{Nd}$  (Grousset et al., 2001) and increasing IRD counts (e.g., IODP Site U1313; Fig. 7E), whereas further north and close to Iceland positive shifts of authigenic  $\epsilon_{Nd}$  correlate to increasing volcanic IRD counts (e.g., ODP Site 980; Fig. 7F). Such contrasting changes of authigenic  $\epsilon_{Nd}$  in nearby locations (Fig. 7B) are unlikely to reflect true watermass differences, but implicate the superimposition of local detrital imprints on global circulation changes at the core sites. As discussed above, such contrasting detrital imprints are also themselves consistent with reduced AMOC that would have increased benthic exposure time during stadial events (Blaser et al., 2019).

Blaser et al. (2019) reported an extreme case of HL detrital

imprinting, where authigenic  $\epsilon_{Nd}$  was completely dominated by detrital sediment  $\epsilon_{Nd}$  sourced from the Canadian Shield. These authors suggested that such imprint was limited to the center of the IRD belt. While reaffirming that detrital imprints are strongest near the IRD belt center, our PCA decomposition reveals subtler detrital imprints at the periphery of the IRD belt which are not limited to any single detrital source in accordance to the complexity of HL provenance (Hemming, 2004). Because of the heterogeneous nature of this type of detrital imprint, we do not attempt any corrections and these records will not be used for circulation reconstruction.

#### 4.2.4. North Indian Ocean

Seawater  $\epsilon_{Nd}$  in the North Indian Ocean today is subject to seasonal variability due to changing terrestrial input linked to monsoon activity, which affects the entire water column in the Bay of Bengal (BoB) as far south as the equator (Yu et al., 2017). It has been debated whether authigenic  $\epsilon_{Nd}$  here reflects ocean circulation or monsoon activity in the past (Burton and Vance, 2000; Naik et al., 2019; Piotrowski et al., 2009; Rashid et al., 2019).

Our data compilation shows that the North Indian authigenic  $\epsilon_{Nd}$  behaved anomalously on both glacial-interglacial and deglacial millennial-scales in the global context. The LGM-Holocene authigenic  $\epsilon_{Nd}$  difference of as much as  $\sim 4.5$  here surpasses values measured everywhere else except the North Atlantic (Fig. 5C, E, 8A).

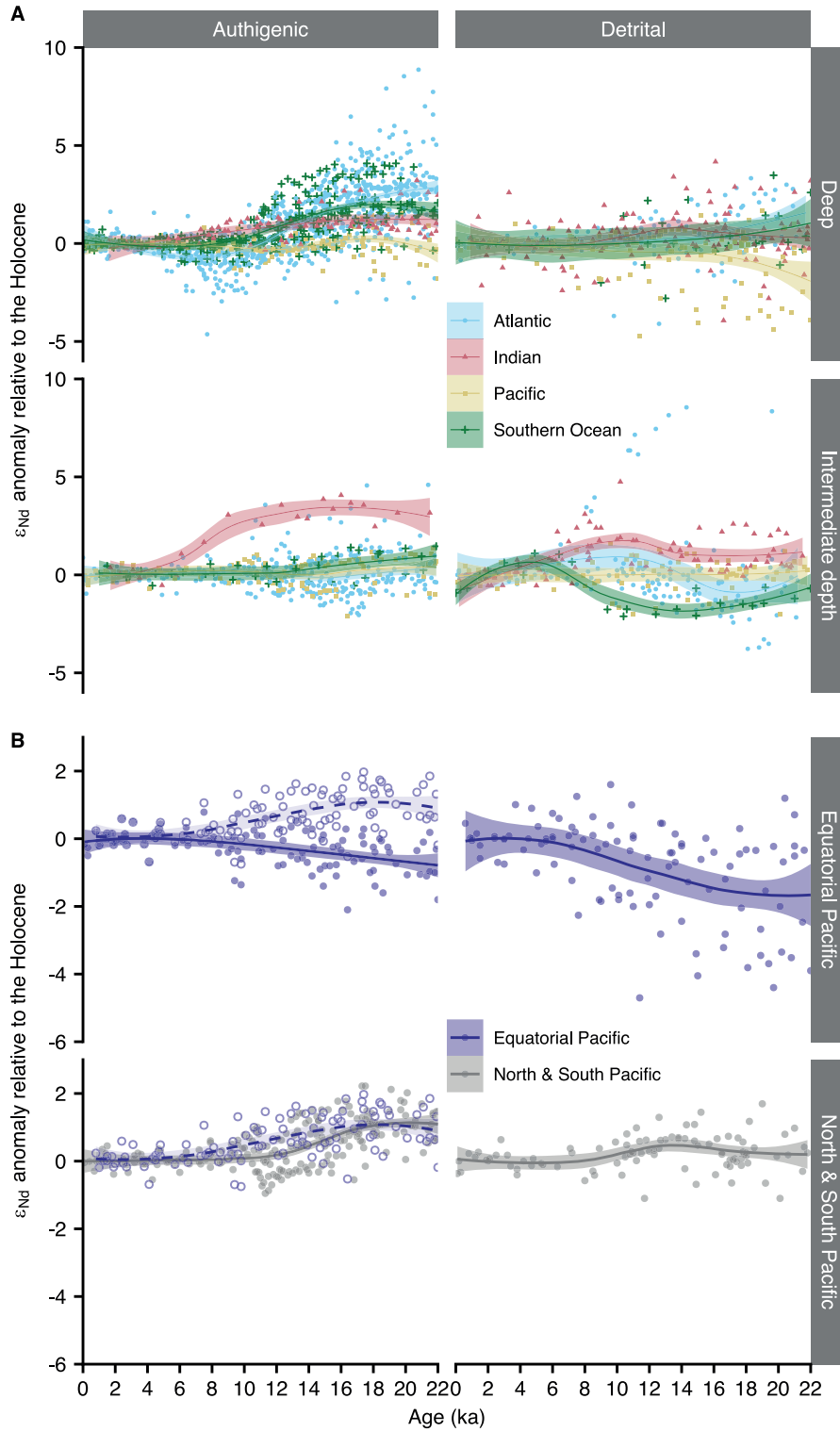


**Fig. 6.** Comparing authigenic and detrital  $\epsilon_{Nd}$  from the global ocean (A) and the Pacific (B). Data are plotted as anomalies with respect to the Holocene (0–6 ka) mean. Shaded lines are LOESS regression lines with 95% CIs. In A data are separated into >1500 m (deep) and 500–1500 m (intermediate depth). In B data (all from the deep ocean) are separated into Equatorial (25°S–25°N) and the rest of the Pacific. In B filled circles indicate raw data. Open circles and dash-shaded line indicate corrected Equatorial Pacific authigenic data and their LOESS regression results (section 4.2.2).

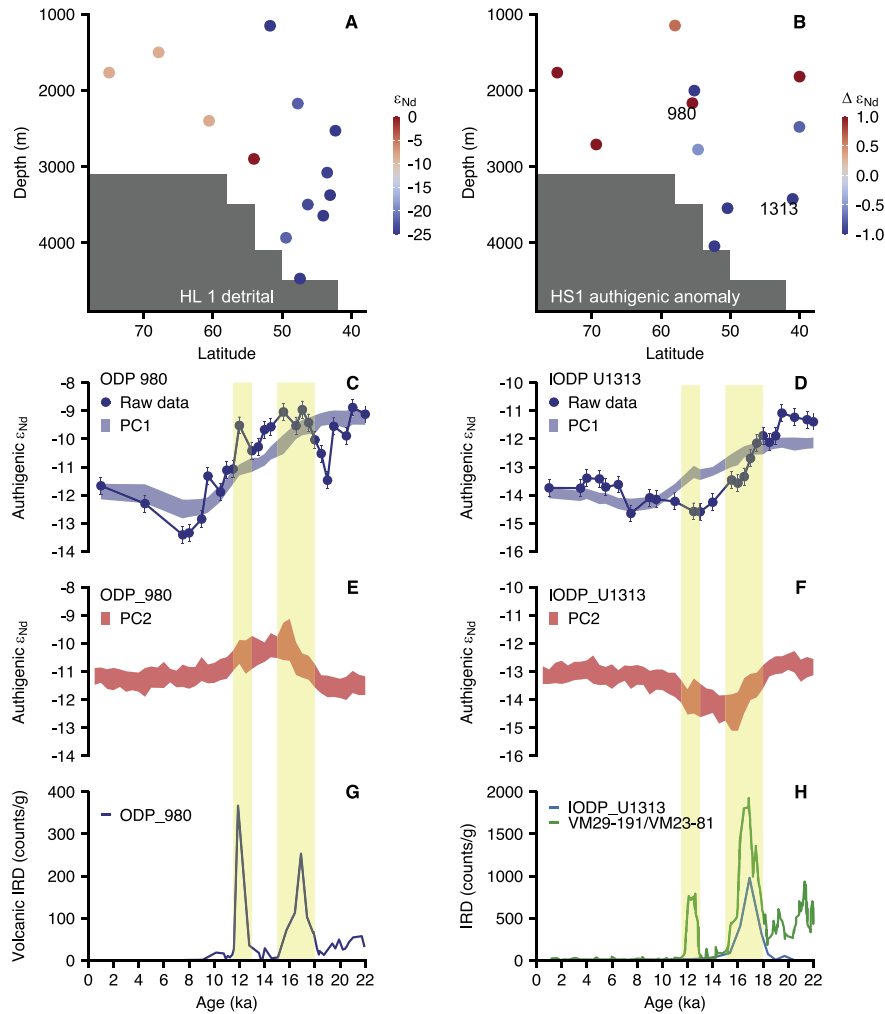


**Fig. 7.** Comparing authigenic and detrital  $\epsilon_{Nd}$  in the subpolar North Atlantic around the IRD belt. **A:**  $\epsilon_{Nd}$  of detrital HL1 (Blaser et al., 2016; Grousset et al., 2001, 2000; Hemming et al., 1998; Jullien et al., 2006; Peck et al., 2006; Plaza-Morlote et al., 2017; Revel et al., 1996; Verplanck et al., 2009). **B:** Deglacial HS1 authigenic  $\epsilon_{Nd}$  anomaly from Fig. 5. The blue color indicates detrital sources and imprints ( $\Delta\epsilon_{Nd} < 0$  in **B**) by materials (likely from the Canadian Shield) with  $\epsilon_{Nd}$  lower than the preformed  $\epsilon_{Nd}$  of modern NADW ( $\epsilon_{Nd} < -13$  in **A**). The red color indicates detrital sources and imprints ( $\Delta\epsilon_{Nd} > 0$  in **B**) by materials (likely Icelandic) with  $\epsilon_{Nd}$  higher than the preformed  $\epsilon_{Nd}$  of modern NADW ( $\epsilon_{Nd} > -13$  in **A**). **C to H:** An example of Icelandic detrital imprint (**C**, **E**, and **G**) using ODP Site 980 (55.5°N, 14.7°W, 2168 m) (Crocker et al., 2016) and an example of Canadian Shield detrital imprint (**D**, **F**, and **H**) using IODP Site U1313 (41°N, 33°W, 3425 m) (Lang et al., 2016; Lippold et al., 2016), the locations of which are shown in **B**. **C** and **D:** The original authigenic  $\epsilon_{Nd}$  records and their PC1s; **E** and **F:** Their PC2  $\epsilon_{Nd}$  records. **G:** Volcanic IRD count at site ODP Site 980. **H:** Total IRD count at IODP Site U1313 and a more complete IRD record from the classic IRD belt at site VM29-191/23-81 (54.27°N, 16.78°W, 2370 m) (Bond et al., 1997).

The magnitude of deglacial authigenic  $\epsilon_{Nd}$  anomalies in the BoB, especially at intermediate depths (~4) (Yu et al., 2018), also surpasses any in the global ocean except for the IRD belt in the North Atlantic (Fig. 5D, F, 8B). Although the general trend of authigenic  $\epsilon_{Nd}$  change here appears to be aligned with the global ocean, as the PCA decomposition reveals (Fig. 8B and C), the magnitudes of change seems unlikely to be explained by circulation alone.

More positive glacial authigenic  $\epsilon_{Nd}$  can also be explained by reduced detrital Nd input (Fig. 8A), which is less radiogenic than seawater in this region today (Yu et al., 2018), perhaps because of a weaker monsoon (Burton and Vance, 2000). The deglacial  $\epsilon_{Nd}$  change also correlates to monsoon activity: during the deglaciation the Indian Monsoon became even weaker than the LGM (Rashid et al., 2011) (Fig. 8E), leading to more positive detrital sediment  $\epsilon_{Nd}$  in the Bengal Fan (Hein et al., 2017; Liu et al., 2019) (Fig. 8D). This could thus have resulted in positive deglacial authigenic  $\epsilon_{Nd}$  anomalies (Fig. 8C). It is possible that local detrital influence worked generally in the same direction as circulation and thus

amplified the authigenic changes in this region on both glacial-interglacial and deglacial millennial timescales. Because most of the published Indian Ocean authigenic  $\epsilon_{Nd}$  records are from the BoB, and that the variable monsoon impact on detrital input extends to the Arabian and Andaman Seas and as far south as the equator during the deglaciation (Ahmad et al., 2005; Goswami et al., 2012; Rashid et al., 2019), we will not discuss Indian Ocean circulation in this study. Quantitatively partition the authigenic  $\epsilon_{Nd}$  changes in the North Indian Ocean into circulation and detrital components will require further studies in the future (Naik et al., 2019).

## 5. Reconstructing past ocean circulation

### 5.1. Glacial-interglacial contrasts

#### 5.1.1. Deep ocean

LGM-Holocene authigenic  $\epsilon_{Nd}$  difference is in most places more

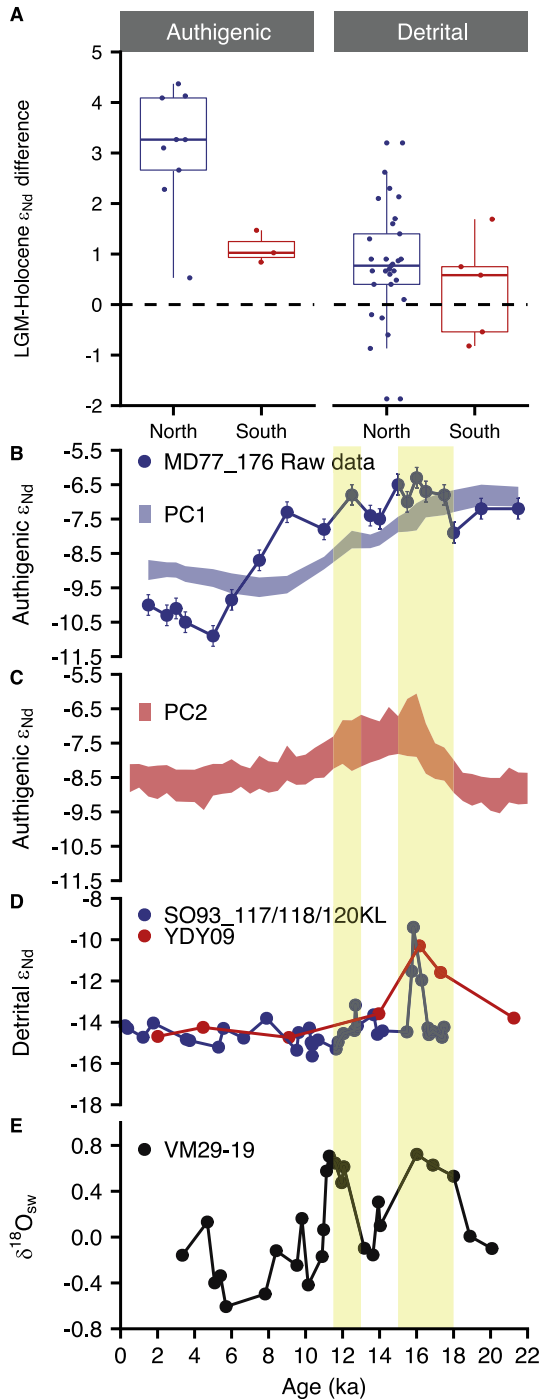


**Fig. 8.** Comparing authigenic  $\epsilon_{Nd}$  records with detrital and monsoon records in the Indian Ocean. **A:** LGM-Holocene differences of authigenic and detrital sediment  $\epsilon_{Nd}$  in the North and South Indian Oceans. **B and C:** Authigenic  $\epsilon_{Nd}$  and its PC1 and PC2 from the Bay of Bengal (MD77\_176: 14.5°N, 93°E, 1375 m) (Yu et al., 2018). **D:** Detrital sediment  $\epsilon_{Nd}$  from the Bengal Fan (16.5°N, 87.8°N, 2605 m; YDY09: 10°N, 86°E, 3520 m) (Hein et al., 2017; Liu et al., 2019). **E:** Ice volume corrected surface water  $\delta^{18}O_{sw}$  records from the Bay of Bengal (VM29-19: 14.7°N, 83.6°E, 3182 m) (Rashid et al., 2011).

positive at water depths >1500 m, except in the Nordic Seas (Fig. 9A), and the most positive values (~+5) occurs in the open North Atlantic between 40–65°N at all depths. A spatial pattern of PC1 related  $\epsilon_{Nd}$  change can be traced throughout the deep ocean, in which the amplitude of glacial increase of  $\epsilon_{Nd}$  is highest the North

Atlantic, decreases toward the Southern Ocean, and continues to decline downstream into the Pacific (Fig. 9A).

We suggest that the spatial pattern of PC1 in the deep ocean is best explained by an increase of the preformed  $\epsilon_{Nd}$  of NSW in the LGM (Gutjahr et al., 2008; Roberts and Piotrowski, 2015; Zhao et al., 2019), and the propagation of this perturbation downstream. In this scenario, the gradual reduction of the magnitude of the perturbation farther from its place of origin (i.e., the North Atlantic) reflects diminishing NSW contribution diluted by mixing, and gradual increase of non-conservative behavior as benthic exposure increases (Du et al., 2018).

A reduction of the NSW/SSW mixing ratio hypothesized for the glacial deep Atlantic (Jonkers et al., 2015; Lippold et al., 2016; Roberts et al., 2010; Rutberg et al., 2000; Wei et al., 2016) cannot explain the highly positive  $\epsilon_{Nd}$  (~−8) in the North Atlantic at all depths (Roberts and Piotrowski, 2015). Glacial  $\epsilon_{Nd}$  here was similar or even more radiogenic than the  $\epsilon_{Nd}$  of modern AABW in the Atlantic (~−9) (van de Flierdt et al., 2016). A fixed-endmember conservative mixing hypothesis would thus imply ~0% NSW at all depths in the North Atlantic, contradicting results based on other tracers that stations shallower than 2000 m in the North Atlantic were occupied largely by pure NSW in the LGM (Curry and Oppo, 2005; Howe et al., 2016a; Oppo et al., 2018). Instead, a change of preformed  $\epsilon_{Nd}$  of NSW can reconcile these tracer distributions and changes.

We explore these conceptual arguments using box model sensitivity tests (Fig. 10): two tests illustrate how  $\epsilon_{Nd}$  responds to hypothetical changes in circulation rate and watermass mixing ratio, and two tests that illustrate how  $\epsilon_{Nd}$  responds to changes in preformed  $\epsilon_{Nd}$  of the endmembers, as follows: “NSW/4” reduces NSW production (F1 in Fig. 1) by 4-fold; “SSW\*4” increases SSW production (F2, F4 and F6) by 4-fold; “NSW pre+5” increases the NSW preformed  $\epsilon_{Nd}$  by 5 units; “SSW pre+5” increases the SSW preformed  $\epsilon_{Nd}$  by 5 units. The scales of these forcings produce  $\epsilon_{Nd}$  responses in the box model similar in magnitude to the observations (Fig. 9A). Our box model is not designed to resolve the local processes that set the preformed  $\epsilon_{Nd}$  at the locations of deep-water formation. Instead, we implement this change via the sedimentary source  $\epsilon_{Nd}$ , which approximates a changing preformed effect in the box model (Du et al., 2018). These simulations all start with modern conditions, and the forcings were applied for 1500 years, by which time steady-state is established. All other parameters remain the same as today.

Both “NSW/4” and “SSW\*4” leads to reduction of NSW/SSW mixing ratio, yet they produce opposite responses (Fig. 10A and B). This is because changes of circulation also cause the partition of non-conservative and conservative  $\epsilon_{Nd}$  components to vary. In “NSW/4” the global benthic exposure time increases, leading seawater and authigenic  $\epsilon_{Nd}$  to approach their basinal detrital  $\epsilon_{Nd}$  signatures and thus diverge from each other. The opposite is true in “SSW\*4”. In contrast, changing the preformed  $\epsilon_{Nd}$  of NSW or SSW produces globally uni-directional changes, which decreases downstream away from the origin (Fig. 10C and D). An increase of NSW preformed  $\epsilon_{Nd}$  is most consistent with the spatial loadings of PC1 (Fig. 10E).

**5.1.1.1. Cause of the preformed NSW  $\epsilon_{Nd}$  change.** We find no significant difference in the distributions of detrital  $\epsilon_{Nd}$  between the LGM and Holocene from the North Atlantic, despite this region having a significantly different distribution in authigenic  $\epsilon_{Nd}$  (Fig. 11). It thus seems unlikely that detrital provenance changed significantly in the North Atlantic region between the LGM and Holocene, and we consider this explanation for changing the preformed  $\epsilon_{Nd}$  of NSW unlikely (Roberts and Piotrowski, 2015).

From a tracer budget perspective, it is also unlikely that changes

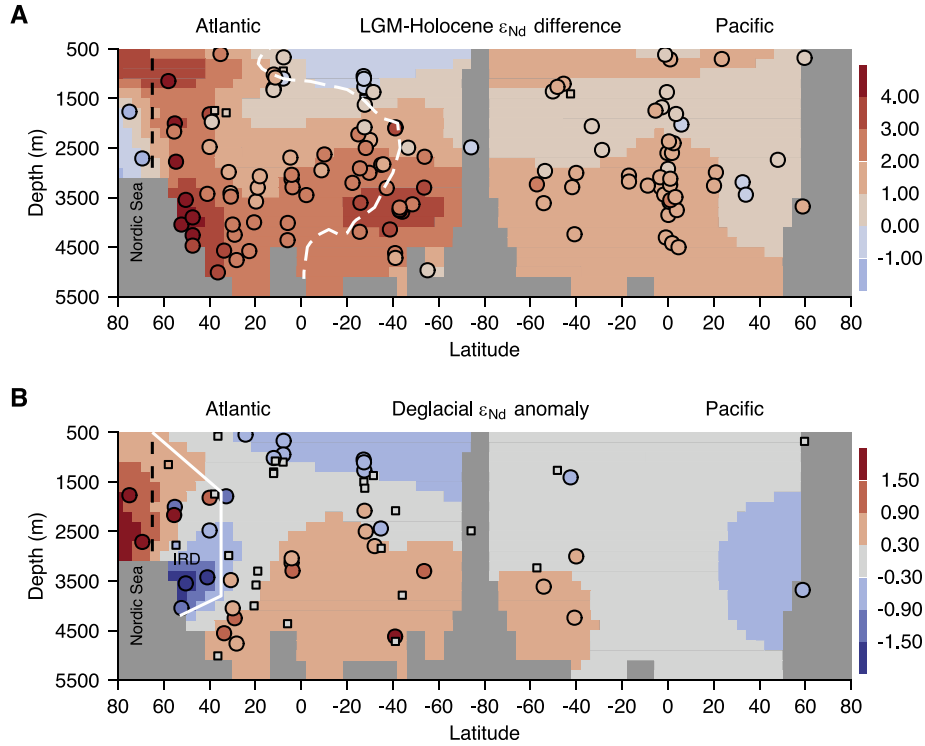


**Fig. 9.** Section plots of (A) LGM-Holocene difference of PC1  $\epsilon_{Nd}$  and (B) Deglacial  $\epsilon_{Nd}$  anomalies, i.e., HS1-LGM difference of PC2  $\epsilon_{Nd}$ . **A** uses the same data as Fig. 5C, E but also includes stations that only have paired LGM and Holocene time-slice data. In **A** we also corrected the Equatorial Pacific records for detrital imprints (section 4.2.1). **B** uses the same data as Fig. 5D, F, but excluding the Equatorial Pacific records since the correction applied is only reasonable on glacial-interglacial timescale (section 4.2.1). Stations with the respective PC loadings that are statistically non-zero (95% CI) are marked by large circles, and those that are not by small squares. The dash black line separates the Nordic Seas from the North Atlantic. In **A**, the white dash line indicates the modern 50% NSW/SSW volume fraction (zonally averaged) (Gebbie and Huybers, 2010). In **B**, the white solid line separates authigenic records subject to HL1 detrital imprints (Fig. 7B). In **A** and **B** red and blue colors indicate positive and negative  $\epsilon_{Nd}$  differences/anomalies respectively. In **B** the grey background indicates values that are not significantly different from zero.

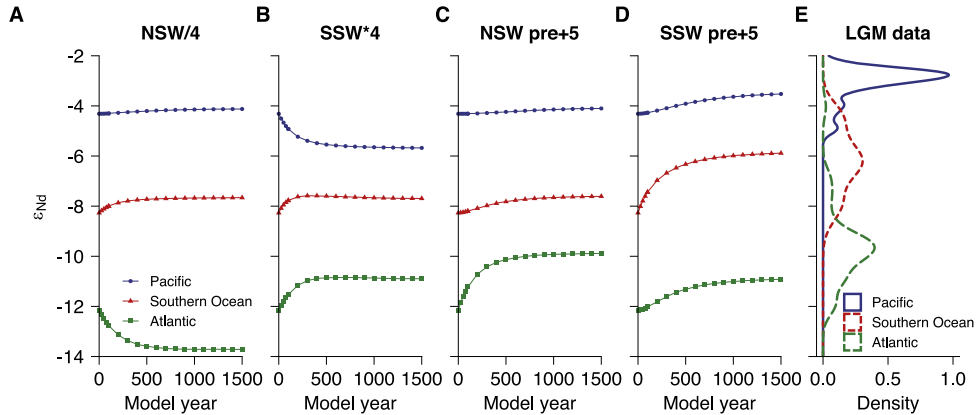


**Fig. 10.** Transient box-model sensitivity tests for conceptual insights into basinal  $\epsilon_{Nd}$  responses to hypothetical circulation changes, compared with LGM observations. **A:** Reduce NSW formation by 4-fold. **B:** Increase SSW formation by 4-fold. **C:** Increase the preformed  $\epsilon_{Nd}$  of NSW by +5. **D:** Increase the preformed  $\epsilon_{Nd}$  of SSW by +5. **E:** Probability density (the probability distribution estimated using a gaussian smoothing kernel) of LGM data from the deep ocean.

of continental chemical weathering flux could have driven the variations of the preformed  $\epsilon_{Nd}$  (Zhao et al., 2019), as dissolved riverine flux only accounts for 7% of the total Nd flux into the modern Atlantic (Table 1). Consider  $\epsilon_{Nd}$  in the Atlantic box

$$\epsilon_{Nd} = \frac{R\epsilon_{Nd}^R + O\epsilon_{Nd}^O}{R + O}, \quad (7)$$

where  $R$  is the riverine flux and  $O$  is the sum of all other source fluxes in Table 1,  $\epsilon_{Nd}^R$  is the riverine  $\epsilon_{Nd}$ , and  $\epsilon_{Nd}^O$  is the weighted

average of the other fluxes. Taking the derivative with respect to the riverine flux and its  $\epsilon_{Nd}$  (assuming other fluxes are constant) we have

$$\Delta\epsilon_{Nd} = \frac{O(\epsilon_{Nd}^R - \epsilon_{Nd}^O)}{(R + O)^2} \Delta R + \frac{R}{R + O} \Delta\epsilon_{Nd}^R \quad (8)$$

and  $\Delta$  signifies LGM-Holocene difference. Assuming a 60% reduction of runoff in the LGM at high latitudes (von Blanckenburg et al., 2015), the riverine  $\epsilon_{Nd}$  would need to increase to  $\sim +2$

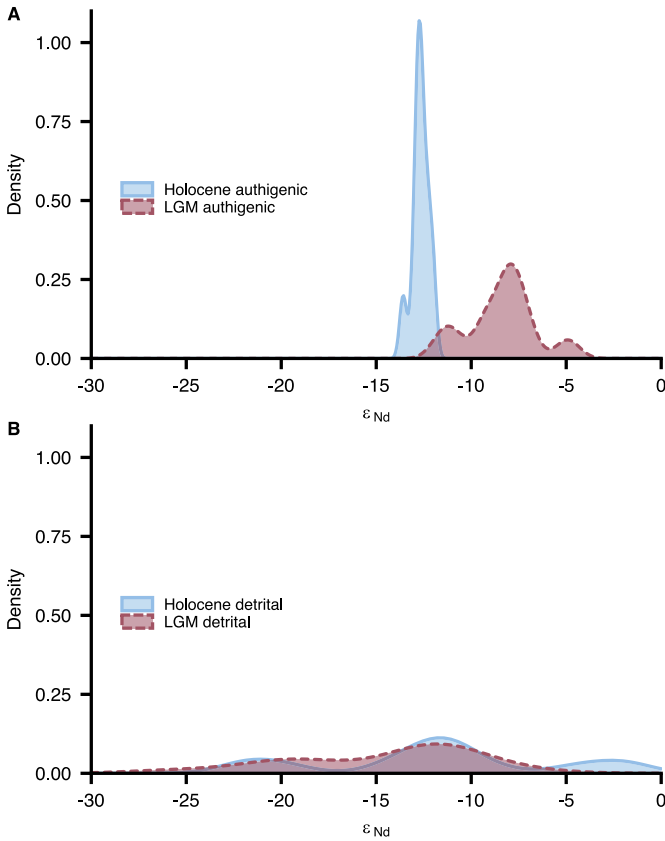


**Fig. 11.** Distributions of Holocene and LGM authigenic (A) and detrital (B)  $\epsilon_{Nd}$  in the North Atlantic (40°N65°N). In A, the Holocene and LGM authigenic data are from the same set of sites, and therefore their difference is not due to sampling difference.

( $\Delta\epsilon_{Nd}^R \approx +14$ ) in the LGM to make  $\Delta\epsilon_{Nd} \approx +2$ , the average change observed in the Atlantic (Fig. 9A). Even ignoring the Canadian Shield and other North America terranes of highly unradiogenic  $\epsilon_{Nd}$  due to ice coverage in the LGM (Zhao et al., 2019), the continental materials surrounding the North Atlantic simply cannot provide such highly radiogenic weathering flux (Goldstein and Jacobsen, 1987; Jeandel et al., 2007). Moreover, as continental weathering flux is introduced to the surface ocean, one would expect its effect to decrease with increasing depth, which is not observed (Fig. 9A). We therefore reject an explanation for changing preformed NSW  $\epsilon_{Nd}$  based on changes in weathering inputs.

Similar calculations show that a change of dust flux is also unlikely to explain the increase of the preformed  $\epsilon_{Nd}$  of NSW in the LGM. Glacial dust input likely was 2–4 time higher than that of the Holocene (Albani et al., 2016; Lambert et al., 2015; Middleton et al., 2018), but this could only increase the dust contribution from ~2% to ~7% in the total basinal Atlantic Nd budget (assuming other sources are constant) and virtually has no impact on seawater  $\epsilon_{Nd}$  ( $\Delta\epsilon_{Nd} \approx 0$  using an equation similar to Equation (8) assuming constant dust  $\epsilon_{Nd}$ ), especially given that the dust and seawater  $\epsilon_{Nd}$  values are similar in the Atlantic (Table 1) (Goldstein et al., 1984; Tachikawa et al., 2003). Moreover, during the LGM, Saharan dust, the most important dust source to the Atlantic, had more negative  $\epsilon_{Nd}$  than the Holocene (Grousset et al., 1998), opposite the direction of change observed for NSW.

A change of preformed  $\epsilon_{Nd}$  of NSW during the LGM could instead be explained by a shift in the location and mode of deep water formation. Zhao et al. (2019) suggested this was unlikely by adopting a top-down view of the acquisition of the preformed  $\epsilon_{Nd}$  of NSW. However, shifting the assumptions to ones in which the

preformed  $\epsilon_{Nd}$  signature is largely acquired at the seafloor offers alternative explanations, falling into two categories: increasing the influence of radiogenic benthic sources and reducing those of unradiogenic sources. The most positive LGM-Holocene authigenic  $\epsilon_{Nd}$  difference is found south of Iceland, at the same place where the most positive non-conservative  $\epsilon_{Nd}$  in the Atlantic is located today (Fig. 2E and F). Paleoclimate models and proxies suggest that the principle location of NSW formation shifted south of Iceland to this region in the LGM (Otto-Bliesner et al., 2007; Sarinthein et al., 1994; Waelbroeck et al., 2009), consistent with an increase in the relative contribution of sedimentary Nd sources of Icelandic basalt origin. It may be countered that the influence of volcanic detrital sediments via the Nordic Sea pathway could have also been reduced due to limited export of glacial NSOW (Thornalley et al., 2015). However, glacial NSOW was less radiogenic than today (Struve et al., 2019), and thus cannot have been a significant contributor to the preformed  $\epsilon_{Nd}$  of NSW in the LGM (Fig. 9A). Regarding the reduction of unradiogenic sources, the contribution of Canadian Shield Nd sources to the NSW preformed  $\epsilon_{Nd}$  was likely reduced in the LGM, because of reduced LSW formation (Hillaire-Marcel et al., 2001), a diminished DWBC pathway (Fagel et al., 1999) along which deep-sea boundary exchange with low- $\epsilon_{Nd}$  detrital sediments happens (Lacan and Jeandel, 2005b) (Fig. 2E, F), and a removal of shelf area in the Baffin-Labrador Basin for sedimentary flux (Arsouze et al., 2008). Evidence shows that authigenic  $\epsilon_{Nd}$  from the deep Labrador Basin was more unradiogenic in the LGM than the Holocene (Blaser et al., 2020). This is opposite to the changes in the open North Atlantic, and is consistent with a weaker DWBC and more isolated Labrador Basin circulation in the LGM (Fagel et al., 1999). Thus it appears that neither the Nordic Sea nor the Labrador Sea were the major sources of glacial NSW.

**5.1.1.2. NSW/SSW mixing ratio.** Taking into account changes in preformed  $\epsilon_{Nd}$ , we re-estimate the change of NSW/SSW mixing ratio in the deep Atlantic in the LGM (Howe et al., 2016a)

$$\epsilon_{Nd} = f^{NSW} \epsilon_{Nd}^{NSW} + (1 - f^{NSW}) \epsilon_{Nd}^{SSW}, \quad (9)$$

where  $\epsilon_{Nd}$  is the seawater  $\epsilon_{Nd}$  at any specific deep site,  $f^{NSW}$  is the NSW mixing ratio and  $\epsilon_{Nd}^{NSW}$  and  $\epsilon_{Nd}^{SSW}$  are the preformed  $\epsilon_{Nd}$  of NSW and SSW respectively. Taking the derivative, we get

$$\Delta f^{NSW} = \frac{\Delta\epsilon_{Nd} - f^{NSW} \Delta\epsilon_{Nd}^{NSW} - (1 - f^{NSW}) \Delta\epsilon_{Nd}^{SSW}}{\epsilon_{Nd}^{NSW} - \epsilon_{Nd}^{SSW}}, \quad (10)$$

where  $\Delta$  again signifies the LGM-Holocene difference. We prefer this “ $\Delta$  formula” of mixing calculation for authigenic  $\epsilon_{Nd}$  because it makes it easier to incorporate preformed change and it also removes (if any) constant authigenic-bottom water  $\epsilon_{Nd}$  offsets (Du et al., 2018; Pöppelmeier et al., 2020). We ignore the influence of seawater [Nd] on  $\epsilon_{Nd}$  given the small difference in basinal averages between Atlantic and Southern Ocean today (Table 1), and because in box model tests, we find that basinal average [Nd] changes in the past were within 5% (Supplementary Figure S2).

We estimate  $\Delta f^{NSW}$  between 35 and 45°S and 2000–4000 m depths in the South Atlantic, a region having  $f^{NSW} = 50\%$  today (Gebbie and Huybers, 2010) (Fig. 9A) that is potentially sensitive to the change of this ratio. In this region,  $\Delta\epsilon_{Nd} = 3.1 \pm 0.3$ , and the modern watermass endmembers are  $\epsilon_{Nd}^{NSW} = -13$  and  $\epsilon_{Nd}^{SSW} = -9$  (van de Flierdt et al., 2016). We find  $\Delta\epsilon_{Nd}^{NSW} = 5.0 \pm 0.5$  (1 $\sigma$  Standard Error) using data from the North Atlantic (45–65°N), and  $\Delta\epsilon_{Nd}^{SSW} = 1.3 \pm 0.2$  using data from the Southern Ocean (south of 45°S) (Fig. 9A). Given these data we use Equation (10) to derive  $\Delta f^{NSW} = 2\% \pm 10\%$ . This indicates that the LGM NSW mixing ratio in

this region was not significantly different from today (Amrhein et al., 2018; Gebbie, 2014; Howe et al., 2016a).

**5.1.1.3. Circulation rate.** The persistence and dominance of the preformed signal (PC1) in authigenic  $\epsilon_{Nd}$  records on the global scale suggest that the glacial GOC was vigorous enough that the preformed effect of NSW was not overwhelmed by non-conservative effects, a situation that is similar to today (Table 1). However, evidence of greater contributions of non-conservative  $\epsilon_{Nd}$  behavior superimposed on this preformed signal is consistent with a somewhat reduced glacial GOC relative to the Holocene (Adkins, 2013; Broecker et al., 2004; Skinner et al., 2017). In the deep Pacific, we showed that the positive LGM-Holocene  $\epsilon_{Nd}$  difference can only be partially explained by the increase of preformed  $\epsilon_{Nd}$  while the majority of the difference was attributed to reduced SSW transport in the LGM (Fig. 10) (Du et al., 2018). In the deep North Atlantic, aside from an increase of preformed  $\epsilon_{Nd}$ , we also find an increase of the heterogeneity of authigenic  $\epsilon_{Nd}$  in the LGM (Fig. 11). This stronger expression of the regional detrital source heterogeneity is consistent with longer benthic exposure times. In the deep South Atlantic,  $\epsilon_{Nd}$  indicates reduced AABW export in the Weddell Sea in the LGM (Huang et al., 2020). The global  $\epsilon_{Nd}$  data thus support a circulation scenario of slightly weaker AMOC and SOMOC in the LGM (Menviel et al., 2016; Muglia et al., 2018; Sarnthein et al., 2013; Sikes et al., 2017; Skinner et al., 2017).

### 5.1.2. Intermediate depth

Glacial intermediate depth (<1500 m)  $\epsilon_{Nd}$  changes are not well-constrained outside the Atlantic (Figs. 5E and 9B). More positive glacial  $\epsilon_{Nd}$  at these depths in the North Atlantic suggests that the inferred high preformed  $\epsilon_{Nd}$  was carried southward by both intermediate and deep NSWs in the LGM (Fig. 9A). A coherent feature of nearly constant (slightly more negative) glacial  $\epsilon_{Nd}$  ( $\sim -0.1$ ) is found at  $\sim 1000$  m in the Equatorial and South Atlantic, which corresponds to the negative non-conservative  $\epsilon_{Nd}$  component in this region today (Fig. 2E). Thus, we interpret this glacial-interglacial change as an increase of the non-conservative component, reflecting slower circulation rate, and/or a weaker penetration of glacial Antarctic Intermediate Water (AAIW) (Pöppelmeier et al., 2020), which are not mutually exclusive if AAIW penetration and the AMOC strength are correlated (Gu et al., 2017). While we cannot constrain the circulation rate change at intermediate depth as we do not know the local Nd budget precisely, we can attempt to quantify changes of watermass mixing.

Intermediate water in this equatorial Atlantic region today has three sources (Oppo et al., 2018): AAIW ( $f^{AAIW} = 75\%$ ,  $\epsilon_{Nd}^{AAIW} = -9$ ,  $[Nd]^{AAIW} = 15$  pM), tropical waters ( $f^{TPW} = 15\%$ ,  $\epsilon_{Nd}^{TPW} = -13$ ,  $[Nd]^{TPW} = 15$  pM) and NSW ( $f^{NSW} = 10\%$ ,  $\epsilon_{Nd}^{NSW} = -13$ ,  $[Nd]^{NSW} = 25$  pM). The  $\epsilon_{Nd}$  and  $[Nd]$  endmembers are estimated using nearby stations, which lead to a mixture of  $\epsilon_{Nd} = -10$  that is consistent with regional seawater data (Piepgras and Wasserburg, 1987; Huang et al., 2014; Osborne et al., 2014; Schlitzer et al., 2018). During the LGM in this region the volume vacated by receding AAIW was occupied by tropical waters rather than NSW (Oppo et al., 2018). There are no data for the glacial AAIW and tropical water  $\epsilon_{Nd}$  endmembers at their formation locations: here we assume that these two shallow endmembers remained the same as today (while we include an uncertainty of 0.5 for error propagation). If the glacial preformed  $\epsilon_{Nd}$  of AAIW was more radiogenic (Pöppelmeier et al., 2020), then the estimate of AAIW reduction would be minimum. We include watermass  $[Nd]$  in this calculation, because they are sufficiently different, but we also assume they are same as today. Under these assumptions, we can derive the change of AAIW mixing fraction:

$$\Delta f^{AAIW} = \frac{\Delta \epsilon_{Nd} [Nd] - \Delta \epsilon_{Nd}^{NSW} f^{NSW} [Nd]^{NSW}}{\epsilon_{Nd}^{AAIW} [Nd]^{AAIW} - \epsilon_{Nd}^{TPW} [Nd]^{TPW}} \quad (11)$$

The LGM-Holocene difference is  $\Delta \epsilon_{Nd} = -0.1 \pm 0.2$  in this region, and we again use  $\Delta \epsilon_{Nd}^{NSW} = 5.0 \pm 0.5$  (section 5.1.1.2). Thus, using Equation (11) we find  $\Delta f^{AAIW} = -25\% \pm 11\%$ , i.e., glacial AAIW was reduced by  $\sim 25\%$  compared to the Holocene. More specifically, we find the small LGM-Holocene  $\epsilon_{Nd}$  difference of  $\sim -0.1$  in this region was the result of two opposing influences canceling each other: a  $-0.9$  effect due to reduced AAIW contribution and a  $+0.8$  effect due to increasing preformed  $\epsilon_{Nd}$  of NSW.

The contrast between the large but consistent  $\epsilon_{Nd}$  patterns in the deep ocean versus the smaller and differing regional  $\epsilon_{Nd}$  patterns at shallow depths (Fig. 9) suggests that the dominant processes controlling the distributions of  $\epsilon_{Nd}$  at these two depths levels are different. At intermediate depth watermass mixing is likely more important as the surface area of seafloor in contact with watermasses is relatively small, compared to the deeper ocean, where interaction with seafloor sediments becomes more important (Du et al., 2018). That is, the contrasting behavior of intermediate and deep waters supports the idea that the glacial changes of deep ocean  $\epsilon_{Nd}$  had an elevated bottom-up contribution compared with the top-down contribution (Abbott et al., 2015a; Du et al., 2018; Haley et al., 2017).

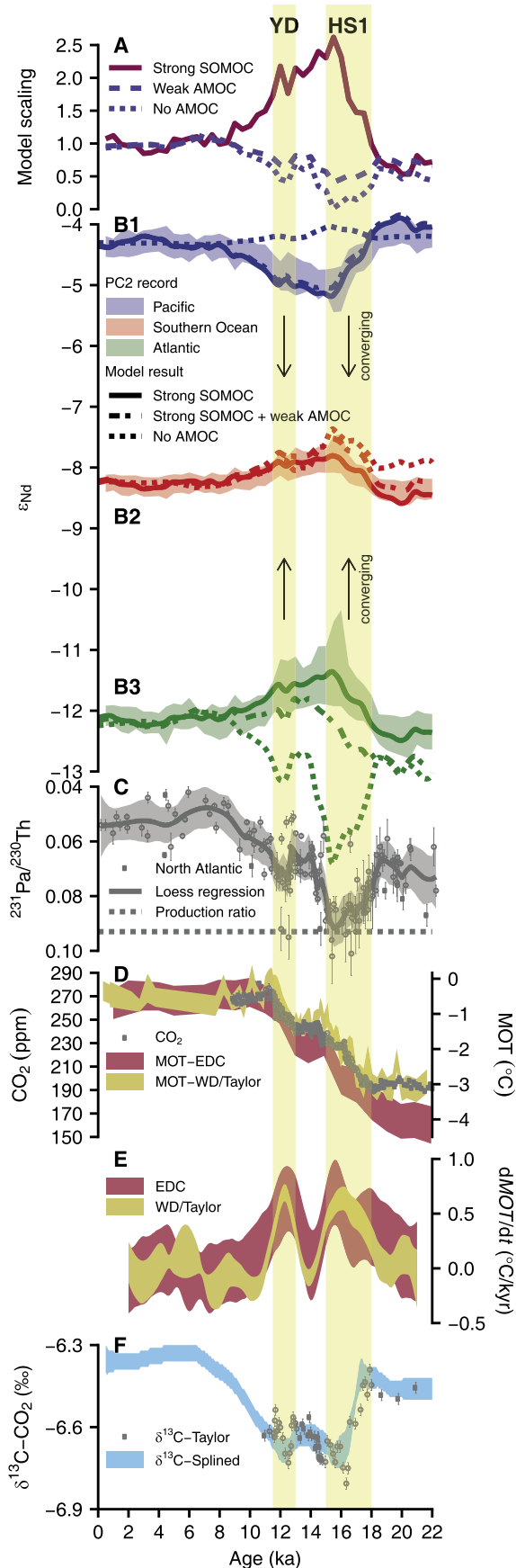
## 5.2. The deglacial transition

To study deglacial circulation we use the PC2 of each authigenic  $\epsilon_{Nd}$  record after removing the PC1 component which we infer mainly reflects a glacial-interglacial change of the preformed  $\epsilon_{Nd}$ . In this way, PCA helps to reveal the secondary deglacial pattern of variation that is not immediately obvious in the raw data. When showing the spatial pattern of PC2 loadings, we use the deglacial anomaly, i.e., the HS1-LGM difference of the PC2  $\epsilon_{Nd}$  records.

### 5.2.1. Deep ocean

Outside the IRD belt, authigenic  $\epsilon_{Nd}$  increased in the deep Atlantic but decreased in the Pacific during HS1 and YD, leading to a convergence of  $\epsilon_{Nd}$  in both these oceans toward the Southern Ocean value, which only became slightly more positive. This is seen spatially in basin cross sections of deglacial  $\epsilon_{Nd}$  anomaly (Fig. 9B) and temporally in the PC2 of high resolution authigenic  $\epsilon_{Nd}$  records (Fig. 12B). In a previous study, we inferred that this deglacial decrease of deep North Pacific  $\epsilon_{Nd}$ , after removing the preformed effect (PC1), was caused by stronger SOMOC (SSW formation) (Du et al., 2018). The global records here further show that the increase in the SOMOC extends also to the deep North Atlantic (Huang et al., 2020), expressed as consistently positive deglacial  $\epsilon_{Nd}$  anomalies (Fig. 9B). Our box model sensitivity tests show conceptually that the Atlantic-Pacific convergence of  $\epsilon_{Nd}$  can be explained by an increase of the absolute strength of the SOMOC, but not by a relative decrease of NSW/SSW mixing ratio due to weaker AMOC (NSW formation) (Fig. 10A and B). We thus conclude that a stronger deglacial SOMOC was a global phenomenon, which could have reduced benthic exposure time of deep waters globally, leading to a greater influence of conservative mixing relative to the non-conservative effect (Du et al., 2018).

We further explore this inference of increased SOMOC during the deglacial transition using box model transient simulations (Fig. 12A). In scenario "Strong SOMOC", we held the AMOC constant and scaled SOMOC transport (SSW production) to PC2, approximately doubling it in HS1 and YD relative to the Holocene. This forcing is similar to our previous study in the Pacific (Du et al., 2018) and consistent with that used in an Earth System Model used to



simulate deglacial change of atmospheric  $\text{CO}_2$  concentration (Menviel et al., 2018). In “No AMOC”, we held the SOMOC constant and scaled AMOC transport (NSW formation) to North Atlantic records of  $^{231}\text{Pa}/^{230}\text{Th}$  (Fig. 12C) (Ng et al., 2018), reducing it to zero in HS1: an extreme scenario. In “Strong SOMOC + weak AMOC” scenario, we used the same SOMOC scaling as in “Strong SOMOC”, but included an AMOC scaling that reduced it to ~60% in HS1. This scaling is consistent with modeled AMOC strength in HS1 using realistic freshwater forcing (Ivanovic et al., 2018). All other parameters are the same as in the modern case. These simulations are compared to the high-resolution records from the deep oceans which offer the best representation of PC2 (Fig. 12B). Because the model results represent basal average  $\epsilon_{\text{Nd}}$  values, they differ from  $\epsilon_{\text{Nd}}$  measured at any specific location in that basin. For model/data comparison, we remove the mean offset between a given record and the modeled basal average.

In these tests (Fig. 12B), an increase in the SOMOC during the deglaciation simulates the observed deep Atlantic-Pacific convergence of  $\epsilon_{\text{Nd}}$ . This convergence occurs with either constant or weakened AMOC, but not with no AMOC. In contrast, if we retain constant SOMOC strength and reduce AMOC, the model will produce Atlantic-Pacific divergence of  $\epsilon_{\text{Nd}}$  during the deglaciation. The  $\epsilon_{\text{Nd}}$  evidence thus indicates a circulation scenario of globally stronger SOMOC and a diminished but persistent AMOC during the deglaciation, with a net global effect of strengthening of the GOC in the deep ocean.

### 5.2.2. Intermediate depth

In the Equatorial and South Atlantic at ~1000 m, we find negative deglacial  $\epsilon_{\text{Nd}}$  anomalies (Fig. 9B) in the same region as in the LGM (Fig. 9A). This pattern again may be explained by reduced AAIW contribution (Howe et al., 2016b; Huang et al., 2014; Poggemann et al., 2018; Xie et al., 2014). We can perform a mixing calculation to quantify this factor as done for the LGM (section 5.1.2). In Equation (11) we use the deglacial anomaly which is  $\Delta\epsilon_{\text{Nd}} = -0.7 \pm 0.4$  in this region, wherein here  $\Delta$  signifies the HS1-LGM PC2 difference. Because we use the deglacial anomaly after removing the preformed effect (i.e., PC1),  $\Delta\epsilon_{\text{Nd}}^{\text{NSW}}$  is 0 in Equation (11) by definition. Adopting the same assumptions as in section 5.1.2 and substitute these data into Equation (11) we find  $\Delta f^{\text{AAIW}} = -20\% \pm 14\%$ . (The HS1-LGM differences of the original  $\epsilon_{\text{Nd}}$  records in this region is ~-1, which can be decomposed to this deglacial anomaly of -0.7 (PC2) and the HS1-LGM difference of -0.2 in the preformed  $\epsilon_{\text{Nd}}$  of NSW (PC1).

Thus, the AAIW mixing ratio (in the AAIW-NSW-tropical water mixture) in this region was reduced by ~20% during HS1 relative to the LGM, or ~45% relative to the Holocene considering the

**Fig. 12.** Observed and simulated deglacial authigenic  $\epsilon_{\text{Nd}}$  records compared to global climate proxies. **A:** Model scaling (with respect to the Holocene mean) applied to the SOMOC (scaled to median PC2 scores in Fig. 5B) and the AMOC (scaled to North Atlantic  $^{231}\text{Pa}/^{230}\text{Th}$  LOESS regression median in C) in simulations. **B:** Model results (lines, labels corresponding to the scaling in A) compared to the PC2 records (ribbons) of representative high resolution authigenic  $\epsilon_{\text{Nd}}$  records from North Pacific (B1, EW0408-87JC, 3680 m) (Du et al., 2018), Southern Ocean (B2, PS75/073\_2, 3234 m) (Basak et al., 2018) and North Atlantic (B3, OCE326\_GGC6/ODP Site1063, 4543 m) (Böhm et al., 2015; Lippold et al., 2019; Roberts et al., 2010). The mean  $\epsilon_{\text{Nd}}$  offset between each individual site and the ocean box average is removed to facilitate data-model comparison. **C:**  $^{231}\text{Pa}/^{230}\text{Th}$  records from the North Atlantic (Ng et al., 2018) (dots for raw data; solid line and ribbon for LOESS regression median and 95% CI). 0.093 (dotted line) is the production ratio. **D:** Ice Core  $\text{CO}_2$  from WAIS Divide (WD) (Marcott et al., 2014) and noble gas derived Mean Ocean Temperature (MOT) anomaly from EPICA Dome C (EDC) and WD. The YD interval of WD record is replaced by Taylor Glacier data (Baggerstos et al., 2019; Bereiter et al., 2018; Shackleton et al., 2019). **E:** Rate change of MOT (dMOT/dt) estimated using nonparametric kernel regression smoothing with a global bandwidth of 1.5 kyr. **F:** Ice core  $\delta^{13}\text{C}-\text{CO}_2$  from Taylor Glacier (Bauska et al., 2016) and a spline-smoothed compilation (Schmitt et al., 2012).

estimated additional 25% reduction in the LGM relative to the Holocene (section 5.1.2). These negative deglacial  $\epsilon_{Nd}$  anomalies therefore support a weaker AMOC during HS1 more than during the LGM (Gu et al., 2017; Huang et al., 2014).

The deglacial  $\epsilon_{Nd}$  anomalies suggest that during the deglaciation the influence of reduced AMOC was limited to the subpolar and intermediate-depth North Atlantic, while the global deep ocean experienced a strengthening of the SOMOC (Fig. 9B).

### 5.3. $\epsilon_{Nd}$ in 3D models

A few studies have implemented  $\epsilon_{Nd}$  in 3-dimensional (3D) Ocean General Circulation and Earth System Models, and performed sensitivity and paleo-experiments (Arsouze et al., 2008; Friedrich et al., 2014; Gu et al., 2020, 2019, 2017; Rempfer et al., 2012a, 2012b). Here we compare them with our simple box model, in light of the new data compilation and our bottom-up framework of the marine Nd cycle.

The Boundary Exchange implementation of sedimentary source in the 3D models was first proposed by Arsouze et al. (2007), who acknowledged uncertainties and heuristic approximations as a first-step toward understanding sedimentary impacts on seawater  $\epsilon_{Nd}$ . Despite evolving understanding of the marine Nd cycle and increasing data density in the following years, the Arsouze et al. (2007) implementation was adopted largely unchanged in all subsequent models. The  $\epsilon_{Nd}$  of the sedimentary source, *i.e.*, the bottom boundary condition in this implementation, was generated by extrapolating a smaller compilation of detrital  $\epsilon_{Nd}$  data on land to the ocean margins. Our coretop detrital compilation suggests that this is not always accurate. For instance, Arsouze' extrapolation produced extremely unradiogenic ( $< -35$ ) detrital  $\epsilon_{Nd}$  southwest of Iceland in the Irminger Sea, a region critical for NSW formation, by extrapolating data on the southeast margin of Greenland. In the coretop data this region is instead occupied by detrital sediments of relatively high  $\epsilon_{Nd}$  ( $\sim -5$ ) (Fig. 2B). Recent leaching studies also showed that the  $\epsilon_{Nd}$  of the reactive detrital components and the operationally defined bulk/residual sediment  $\epsilon_{Nd}$  are correlated but unlikely to be the same (Abbott et al., 2016; Blaser et al., 2016; Du et al., 2016; Wilson et al., 2013). For this reason, we inferred the  $\epsilon_{Nd}$  of sedimentary flux in our box model by balancing the modern budget rather than using averaged coretop detrital  $\epsilon_{Nd}$  (Table 1).

To date, 3D models have implemented sedimentary Nd sources only on the margins shallower than 3000 m, another apparent legacy of Arsouze et al. (2007). This assumption is questionable. In fact, the largest benthic Nd flux ( $36 \text{ pmol cm}^{-2} \text{ yr}^{-1}$ ) measured to date was from below this depth (at 3400 m) (Haley and Klinkhammer, 2003), and recent observations further confirms high benthic Nd flux from the deep seafloor (Fig. 1) (Abbott, 2019; Abbott et al., 2015b). The 3D models may thus have missed the dominant Nd source given that  $\sim 75\%$  of the global seafloor area is below 3000 m (de Lavergne et al., 2016; Du et al., 2018). In the 3D models, bottom water  $\epsilon_{Nd}$  is also often "relaxed" toward detrital sediment  $\epsilon_{Nd}$  bottom boundary condition with timescales that decrease by orders of magnitude at greater depths, presuming that sedimentary fluxes decrease significantly with increasing depth. However, this assumption is inconsistent with pore water measurements (Fig. 1C) (Abbott, 2019; Abbott et al., 2015b).

With these potential issues in mind we compare our box model tests to experiments performed using 3D models. Among the four sensitivity tests (Fig. 10, *i.e.*, reduce the AMOC/NSW, increase the SOMOC/SSW, increase the preformed  $\epsilon_{Nd}$  of NSW and increase the preformed  $\epsilon_{Nd}$  SSW), our box model results of the latter three agree with the 3D models: Both Bern3D (Rempfer et al., 2012a) and LOVCLIM (Friedrich et al., 2014) simulated Atlantic-Pacific convergence when increasing the SOMOC/SSW production (Fig. 10B).

Bern3D also produced similar patterns after increasing the preformed  $\epsilon_{Nd}$  of NSW and SSW by changing local sediment source (Rempfer et al., 2012b) (Fig. 10C and D).

There is however disagreement among the 3D models on the effect of reducing the AMOC/NSW formation. Community Earth System Model (CEMS) produced more negative NSW  $\epsilon_{Nd}$  when reducing the AMOC (Gu et al., 2019). This is conceptually consistent with our interpretive framework and box model result that increasing benthic exposure time causes NSW  $\epsilon_{Nd}$  to converge to unradiogenic  $\epsilon_{Nd}$  sediments (Figs. 10A and 3C), except that in CESM this negative  $\epsilon_{Nd}$  pattern was limited to above  $\sim 3000$  m in the North Atlantic whereas at greater depth  $\epsilon_{Nd}$  became positive. This discrepancy is likely an artifact of limiting Boundary Exchange to above 3000 m, which misses the influence of the unradiogenic sediments in the abyssal North Atlantic (Fig. 2B, E, and F). The Bern3D and LOVECLIM models, in contrast, both simulated more positive  $\epsilon_{Nd}$  throughout the deep North Atlantic ( $> 1500$  m) when reducing the AMOC. This discrepancy may be related to the much lower vertical resolution in these two models compared to CESM, suggesting that modeled Atlantic  $\epsilon_{Nd}$  depends on how finely the highly heterogeneous bottom boundary condition in the North Atlantic is resolved (Fig. 2B).

None of the 3D models can produce the PC1 pattern by *solely* changing circulation rate or NSW/SSW mixing ratios in the LGM. Arsouze et al. (2008) suggested reduced glacial deep Atlantic NSW/SSW mixing ratios based on the very limited authigenic  $\epsilon_{Nd}$  data available to them, yet their model of weaker and shallower glacial AMOC also produced opposite signs of  $\epsilon_{Nd}$  change between the western and eastern Atlantic, not seen in data (Fig. 5C, E). Friedrich et al. (2014) similarly advocated the mixing ratio hypothesis, yet their model produced opposite signs of  $\epsilon_{Nd}$  change between  $40-65^\circ\text{N}$  and the rest of the Atlantic, and even greater magnitude of change in the deep North Pacific, inconsistent with data (Fig. 9A). Gu et al. (2020) in a simulation with weaker AMOC in the LGM also did not capture the highly radiogenic  $\epsilon_{Nd}$  values in the glacial North Atlantic between  $40-65^\circ\text{N}$  (Fig. 9A). The failure of these models to correctly simulate the change of preformed  $\epsilon_{Nd}$  of NSW in the LGM suggests the traditional model implementation of sedimentary Nd source is incomplete.

None of the 3D models can produce the PC2 pattern by *solely* reducing the AMOC in deglacial stadial events. In Bern3D and LOVECLIM, hosing the North Atlantic led to uni-directional  $\epsilon_{Nd}$  changes to more positive values in the Atlantic and Pacific (Friedrich et al., 2014; Rempfer et al., 2012a), while strengthening the SOMOC led  $\epsilon_{Nd}$  in these two basins to converge, as we observed and model (Figs. 12B and 10B). In their models, reducing the AMOC and strengthening the SOMOC both led to more positive  $\epsilon_{Nd}$  in the deep Atlantic. While the Atlantic data alone could be explained by mixing ratios and the AMOC strength, the Pacific data require acceleration of the SOMOC during the deglacial interval (Du et al., 2018) and this acceleration can also partially explain the Atlantic data.

These 3D models have also been used to perform tests relevant to paleo-reconstruction that were not done using our box model. For example, Rempfer et al. (2012b) varied the magnitude of sedimentary flux in each ocean basin in Bern3D, but the results cannot explain either the PC1 or PC2 patterns. Further, varying particle fields in Bern3D and CESM both resulted in little change of  $\epsilon_{Nd}$  (Gu et al., 2019), suggesting that reversible scavenging has limited impact on marine Nd budget.

We suggest that previous studies on paleo- $\epsilon_{Nd}$  using 3D models were limited by premature assumptions on sediment Nd sources made at a time when the sedimentary influence on seawater  $\epsilon_{Nd}$  was just emerging, and also by the small number of available paleo-records at a time when data from outside the North Atlantic were

scarce. Our simple box model is designed to address the basin-to-global scale changes that dominate the authigenic  $\epsilon_{Nd}$  records, appropriate to the present understanding of sediment Nd sources on this spatial scale. As such, we are encouraged by the ability of this box model to capture the first-order observations, and hope that it offers a steppingstone for the implementation of this new framework of the marine Nd cycle in 3D models that can readily remove the said limitations on these models for more detailed and quantitative reconstruction of past circulation. Mapping out the finer regional details of the GOC using  $\epsilon_{Nd}$  in 3D models will require better constraints on the spatial and temporal variabilities of the sedimentary sources that should be the priority of future research on marine Nd cycle.

## 6. Discussion

### 6.1. Implications for LGM climate and other circulation tracers

The  $\epsilon_{Nd}$ -based inference that the glacial NSW/SSW mixing ratio in the deep Atlantic was roughly similar to today can be reconciled with benthic  $\delta^{13}C$  data, if the non-conservative properties of  $\delta^{13}C$  due to remineralization increased, and/or if the preformed  $\delta^{13}C$  of SSW and/or NSW decreased in the LGM (Gebbie, 2014; Mix and Fairbanks, 1985; Howe et al., 2016a). Consistent with these requirements, carbonate system parameters suggest greater accumulation of remineralized carbon in the glacial deep ocean (Broecker et al., 2004; Burke and Robinson, 2012; Chalk et al., 2019; Rae et al., 2018), and inverse methods suggest lower preformed  $\delta^{13}C$  of glacial SSW (Gebbie, 2014; Oppo et al., 2018). A two-layer structure of glacial NSWs is also possible, in which a high preformed  $\delta^{13}C$  intermediate-to-mid depth NSW (<2500 m; Glacial North Atlantic Intermediate Water/GNAIW) formed through open-ocean convection with strong air-sea gas exchange, and a low preformed  $\delta^{13}C$  bottom NSW (>2500 m; Glacial North Atlantic Bottom Water/GNABW) formed under sea ice with limited air-sea gas exchange (Howe et al., 2016a; Keigwin and Swift, 2017; Mix and Fairbanks, 1985; Zhao et al., 2019) (Fig. 13A). Such a glacial NSW division is not yet fully resolved by  $\epsilon_{Nd}$  data (Fig. 9A), but this  $\epsilon_{Nd}$ - $\delta^{13}C$  comparison speaks to the importance of the multi-proxy approach to circulation reconstruction (Gu et al., 2020; Lippold et al., 2016; Muglia et al., 2018; Ng et al., 2018; Piotrowski et al., 2005; Skinner et al., 2013), taking advantage of the differing mechanisms that control various circulation tracers.

A reduced GOC rate in the LGM inferred using authigenic  $\epsilon_{Nd}$  is consistent with an estimate of global ocean residence time ~700 years longer than today based on benthic radiocarbon (Sarnthein et al., 2013; Skinner et al., 2017). We can reject substantially longer residence times than this because they would cause convergence of authigenic  $\epsilon_{Nd}$  toward regional detrital signatures by increasing the non-conservative effect (Abbott et al., 2015a; Du et al., 2018), which is inconsistent with the geographic distribution of PC1 as we infer to reflect a preformed signal (Fig. 9A).

The proposed  $\epsilon_{Nd}$ -based glacial GOC scenario has implications for understanding reduced atmospheric  $CO_2$  in the LGM relative to Holocene values. The inference of similar-to-today glacial NSW mixing ratio is contrary to hypotheses invoking higher efficiency of the glacial biological pump due to increasing ventilation by nutrient poor NSW (Kwon et al., 2012). Instead, with support from general circulation-biogeochemical model simulations (Menviel et al., 2016; Muglia et al., 2018), we suggest that the overall slower GOC, including both the AMOC and SOMOC cells (Fig. 13A), drove increased carbon sequestration in the glacial deep ocean (Broecker et al., 2004; Jacobel et al., 2020; Rae et al., 2018; Skinner et al., 2017).

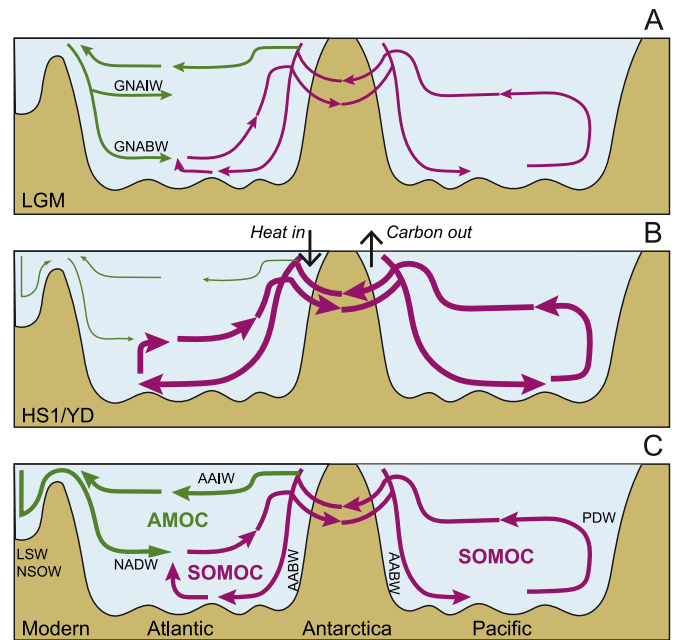


**Fig. 13.** Schematics of ocean circulation in the LGM (A), HS1 and YD (B), and today (C). The modern scheme is based on Talley (2013). Note inferred Glacial North Atlantic Intermediate and Bottom Water (GNAIW and GNABW). For schematics LSW and NSOW appear together but separated from the North Atlantic basin. The thickness of the lines indicates hypothetical transport strength. For  $\epsilon_{Nd}$ -based NPIW reconstruction we refer to our previous study (Du et al., 2018) where we found it to not have changed significantly since the LGM.

### 6.2. Implications for the deglacial events and other circulation tracers

Our decomposition of global  $\epsilon_{Nd}$  variability into its PC1 and PC2 components offers resolution to an apparent conflict between deglacial records of authigenic  $\epsilon_{Nd}$  and sedimentary  $^{231}Pa/^{230}Th$  in the deep North Atlantic (Fig. 14). Based on ostensibly invariant  $\epsilon_{Nd}$  between the LGM and HS1, previous studies have suggested little change of deep North Atlantic circulation in this interval, which contradicts the evidence of reduced AMOC according to  $^{231}Pa/^{230}Th$  (Howe et al., 2018; Roberts et al., 2010). Our  $\epsilon_{Nd}$  decomposition shows that the small LGM-to-HS1 change in  $\epsilon_{Nd}$  in the deep North Atlantic may result from the two components of  $\epsilon_{Nd}$  acting in opposite directions and therefore canceling each other out in this region (Fig. 14). Once the PC1 (preformed  $\epsilon_{Nd}$ ) is removed from the North Atlantic records, the PC2 of  $\epsilon_{Nd}$  does indeed correlate *positively* to  $^{231}Pa/^{230}Th$  in the deep North Atlantic, revealing that changes of overturning strength and watermass provenance were coupled during the deglaciation. This is expected given that the residence time of Nd is much longer and consequently  $\epsilon_{Nd}$  is subject to greater preformed effect than  $^{231}Pa/^{230}Th$  (Deng et al., 2018).

Whether the AMOC completely collapsed during Northern Hemisphere stadial events is crucial for understanding climate tipping points (Bradtmeier et al., 2014; Ivanovic et al., 2018; Lippold et al., 2012; McManus et al., 2004; Ng et al., 2018; Schmittner and Lund, 2015).  $\epsilon_{Nd}$  shows that the AMOC persisted, albeit in somewhat weakened state, during these events (Howe et al., 2018). Our findings are consistent with climate models that do not shut down the AMOC using realistic freshwater forcing (Ivanovic et al., 2018). Reduced AMOC would increase sedimentary  $^{231}Pa/^{230}Th$  ratio in the deep Atlantic by reducing local  $^{231}Pa$  export, but if the AMOC was still active we would not expect  $^{231}Pa/^{230}Th$  to approach, let alone exceed, the production ratio. Even after ruling out

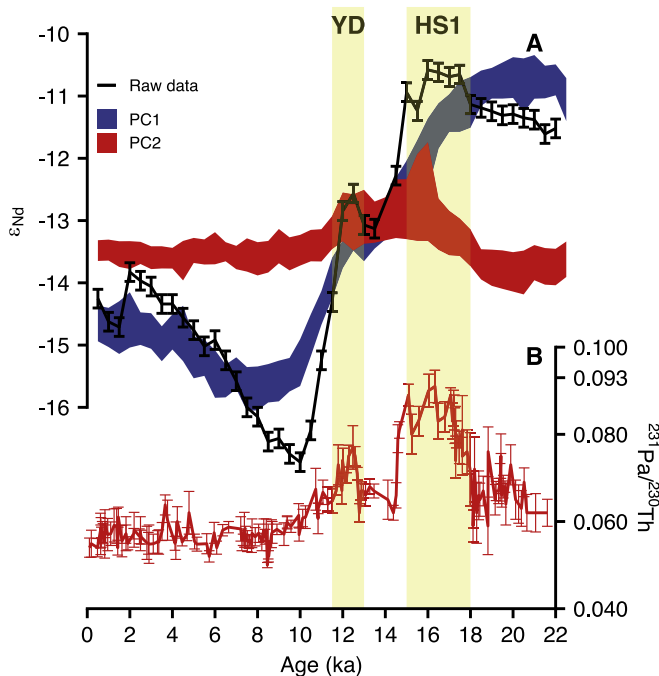


**Fig. 14.** Authigenic  $\epsilon_{Nd}$  and sedimentary  $^{231}Pa/^{230}Th$  records from the Bermuda Rise site OCE326\_GGC6/ODP Site 1063. **A:** Authigenic  $\epsilon_{Nd}$  (Böhm et al., 2015; Lippold et al., 2019; Roberts et al., 2010) and its PC1 and PC2. **B:** Sedimentary  $^{231}Pa/^{230}Th$  (Böhm et al., 2015; Lippold et al., 2019; McManus et al., 2004).

differential scavenging effects, high  $^{231}Pa/^{230}Th$  ratios are still found in the deep Atlantic (Ng et al., 2018), raising a dilemma. Given the positive correlation between  $\epsilon_{Nd}$  and  $^{231}Pa/^{230}Th$ , we suggest that this dilemma can be resolved by increasing Pa import from the Southern Ocean to the deep North Atlantic due to stronger SOMOC (Negre et al., 2010), i.e., high  $^{231}Pa/^{230}Th$  ratios in the deep North Atlantic during the deglaciation are results of both reduced AMOC and stronger SOMOC. Consideration of this import from the south results in the need for less severe reductions of the AMOC to account for the observed HS1  $^{231}Pa/^{230}Th$  values (Ivanovic et al., 2018).

We have inferred that during the deglaciation, global deep and bottom water residence times decreased in spite of diminished AMOC, because of stronger SOMOC (Huang et al., 2020). This inference is consistent with  $^{14}C$  data, which show that the deep North Atlantic had as large a  $^{14}C$  offset ( $\sim -250\%$ ) from the atmosphere, as did the Southern Ocean, during HS1 (Robinson et al., 2005). This scenario of fast overturning of a SSW with high apparent  $^{14}C$  age is also consistent with North Pacific  $^{14}C$  data (Du et al., 2018). As we have argued previously, the globally high apparent benthic  $^{14}C$  reservoir age could thus be attributed to a high SSW preformed  $^{14}C$  age (Zhao et al., 2018), driven by mixing of old PDW into the Southern Ocean and incomplete gas-isotope exchange as excess  $CO_2$  was released to the atmosphere (Du et al., 2018). This inference is also supported by benthic  $\delta^{13}C$ . During HS1, benthic  $\delta^{13}C$  at depths  $>3000$  m in the South Pacific and South Atlantic was similar ( $\sim 0\%$ ), contrary to the strong inter-ocean gradients seen both in the LGM and Holocene (Sikes et al., 2017). Analogous to  $^{14}C$ , Atlantic-Pacific convergence of  $\delta^{13}C$  in HS1 occurred when Atlantic  $\delta^{13}C$  was becoming more negative (Lund et al., 2015). This observation implies changes of the preformed  $\delta^{13}C$  as a significant driver of evolving deglacial benthic  $\delta^{13}C$  (Lynch-Stieglitz et al., 2019; Mix and Fairbanks, 1985). Like  $^{14}C$  (Du et al., 2018), the effects of preformed changes in  $\delta^{13}C$  were likely

large enough to mask other components of benthic  $\delta^{13}C$  upon visual inspection, as is the case for  $\epsilon_{Nd}$ .

The proposed acceleration of the SOMOC during the deglaciation (Fig. 13B) generally aligns with steps of rapid deglacial rise of atmospheric  $CO_2$  concentration (Du et al., 2018; Marcott et al., 2014; Shakun et al., 2012) (Fig. 12D). As such, increasing carbon storage in the mid-depth Atlantic during these stadial events precludes reduction of the AMOC as a prime driver of atmospheric  $CO_2$  rise (Lacerra et al., 2017). Rather, release of excess  $CO_2$  due to intensified SOMOC and flushing of accumulated carbon from the abyssal ocean, particularly from the Pacific, seems a more likely driver of atmospheric  $CO_2$  (Anderson et al., 2009; Burke and Robinson, 2012), which can also explain the deglacial decreases of the  $\delta^{13}C$  of  $CO_2$  in the atmosphere (Schmitt et al., 2012; Bauska et al., 2016) (Fig. 12F). The SOMOC scaling used in our box model, which can reproduce deep ocean authigenic  $\epsilon_{Nd}$  records in both the Atlantic and Pacific (Fig. 12A), is similar to the one used in a three-dimensional Earth System Model that simulates atmospheric rise of  $CO_2$  during HS1 (Menviel et al., 2018). We thus conclude that authigenic  $\epsilon_{Nd}$  indicates a dominant role of the SOMOC in the deglacial rise of atmospheric  $CO_2$  concentration (Anderson et al., 2009; Basak et al., 2018; Burke and Robinson, 2012; Du et al., 2018; Rae et al., 2018; Skinner et al., 2010).

These inferred changes of the SOMOC may also explain the evolution of global ocean heat budget during the deglaciation (Shakun et al., 2012). Mean Ocean Temperature (MOT) (Bereiter et al., 2018), volumetrically weighted toward the deep ocean, increased rapidly during the deglaciation (Fig. 12E). With reduced AMOC in these intervals, stronger SOMOC may be needed to efficiently bring heat from the surface to the global deep ocean (Bereiter et al., 2018). The  $\epsilon_{Nd}$ -based inference that a greater volume of the global deep ocean was ventilated by the SOMOC during these intervals offers a mechanism for why MOT is highly correlated to Antarctic surface temperature (Bereiter et al., 2018). This appears to be consistent with a dominant AABW pathway of anthropogenic heat uptake by the abyssal ocean today (Purkey and Johnson, 2013), and that AABW may reinvigorate during the ongoing global warming (Abrahamsen et al., 2019). The conclusion that the SOMOC sustained warming during the last deglaciation, through its influence on both atmospheric  $CO_2$  and ocean heat transport (Shakun et al., 2012) (Fig. 13B), may prove useful for model testing which can help elucidate the yet unresolved role of the SOMOC in future warming (Meijers, 2014).

## 7. Conclusion

To interpret authigenic  $\epsilon_{Nd}$  records we further develop a “bottom-up” framework of marine Nd cycle proposed recently (Abbott et al., 2015a; Du et al., 2018, 2016; Haley et al., 2017). Using a box model we find that sedimentary Nd flux is the dominant external source, in agreement with previous studies (Arsouze et al., 2009; Tachikawa et al., 2003), except that we place the benthic source primarily in the deep ocean where the seafloor area in contact with bottom water is the largest. We further identify that the non-conservative behavior of seawater and authigenic  $\epsilon_{Nd}$  is widespread in the global ocean, and that these behaviors are predictable functions of benthic exposure time and detrital sediment composition. In the Pacific, the non-conservative behavior is driven by a radiogenic (volcanic origin) sedimentary flux that causes seawater and authigenic  $\epsilon_{Nd}$  to become more positive as watermasses age. The Atlantic is dominated by an opposite trend towards an unradiogenic character because of sediments of Canadian Shield origin, while the sedimentary influence of Icelandic basalt is limited to young waters near the location of modern deep-water formation. In the modern ocean seawater  $\epsilon_{Nd}$  in the Atlantic is less influenced by

the non-conservative behavior due to sedimentary influence than seawater in the Pacific because of the Atlantic's shorter water residence time. Our analysis reaffirms the bottom-up acquisition of the preformed  $\epsilon_{Nd}$  of NSW today that depends on its formation mode and pathway (Lacan and Jeandel, 2005b).

Under this framework, we describe coherent patterns of change in authigenic  $\epsilon_{Nd}$  records since the LGM using PCA. When comparing the results to detrital sediment  $\epsilon_{Nd}$  records, we identify three regions (the Equatorial Pacific, the IRD belt in the North Atlantic, and the North Indian Ocean) where temporally variable detrital imprint on authigenic  $\epsilon_{Nd}$  was likely driven by changes of detrital provenance on glacial-interglacial and/or deglacial millennial timescales.

The PC1 pattern shows that in the deep ocean authigenic  $\epsilon_{Nd}$  was consistently more positive in the LGM than the Holocene, a difference that is greatest in the North Atlantic, and decreases downstream toward the Southern Ocean and the Pacific. Based on box model sensitivity tests, we infer that this pattern is best explained by an ( $\sim+5$  unit) increase of the preformed  $\epsilon_{Nd}$  of NSW in the LGM, likely linked to a shift of deep-water formation location. Once this preformed effect is taken into account, we find little change in NSW/SSW mixing ratio in the deep Atlantic in the LGM compared to today. Superimposed on this preformed effect, we find evidence for greater non-conservative behavior of authigenic  $\epsilon_{Nd}$  in the Atlantic and Pacific, which would be consistent with weaker AMOC and SOMOC in the LGM than today. A pattern of more negative authigenic  $\epsilon_{Nd}$  in the LGM at intermediate depth in the Equatorial and South Atlantic is interpreted as the result of weaker circulation strength or reduced AAIW contribution.

The PC2 pattern shows that deep Atlantic and Pacific authigenic  $\epsilon_{Nd}$  converged toward Southern Ocean values during the deglacial transition. Based on box model transient simulations, we suggest that this pattern is consistent with a circulation scenario of stronger SOMOC and reduced, but not ceased, AMOC during the deglaciation. At intermediate depths, we find a pattern of more negative  $\epsilon_{Nd}$  in HS1 than in the LGM in the Equatorial and South Atlantic, similarly suggested to be the result of weaker circulation strength or reduced AAIW contribution, more so than in the LGM.

Our interpretation and box model results are qualitatively consistent with modelling results of more complex models, though we consider the implementation of sedimentary Nd cycle in these models to be inaccurate in its lack of a deep benthic source. Our simple model provides a new framework of marine Nd cycle that future studies could implement in more physically sophisticated models.

The inferred circulation scenarios for the LGM and deglaciation can be reconciled with other circulation tracers ( $\delta^{13}C$ ,  $\Delta^{14}C$  and  $^{231}Pa/^{230}Th$ ) after taking into account circulation factors other than NSW/SSW mixing ratio and the AMOC strength, including changes in preformed properties and the non-conservative behavior of  $\delta^{13}C$  and  $\Delta^{14}C$ , and potential Southern Ocean (SSW) influences on  $^{231}Pa/^{230}Th$ .

The reconstructed circulation changes suggest sluggish global circulation as most likely the key cause of lower glacial atmospheric  $CO_2$  (Jacobel et al., 2020). Further, we argue that during the deglaciation, strengthening of the SOMOC was likely the driving factor of carbon release to the atmospheric and warming of the abyssal ocean.

## Author contributions

J.D., B.A.H. and A.C.M. designed this study. J.D. led the effort of data collection, analysis and modeling. B.A.H. and A.C.M. contributed to data interpretation. J.D. wrote the initial manuscript and produced the figures with significant contributions from B.A.H. and

A.C.M.

## Declaration of competing interest

The authors declare that they have no known competing financial interests or personal relationships that could have appeared to influence the work reported in this paper.

## Acknowledgements

Funding for this study was provided by US National Science Foundation Grant #1502754 to A.C.M. and #1357529 to A.C.M. and B.A.H. J.D. was also supported by an ETH Zurich Postdoctoral Fellowship 19-2 FEL-32. We thank Andreas Schmittner and Clare Reimers for helpful comments. We also thank two anonymous referees for comments that helped us to improve the manuscript.

## Appendix A. Supplementary data

Supplementary data to this article can be found online at <https://doi.org/10.1016/j.quascirev.2020.106396>.

## References

- Abbott, A.N., 2019. A benthic flux from calcareous sediments results in non-conservative neodymium behavior during lateral transport: a study from the Tasman Sea. *Geology* 47, 363–366. <https://doi.org/10.1130/G45904.1>.
- Abbott, A.N., Haley, B.A., McManus, J., 2015a. Bottoms up: sedimentary control of the deep North Pacific ocean's  $\epsilon_{Nd}$  signature. *Geology* 43. <https://doi.org/10.1130/G37114.1>, 1035–1035.
- Abbott, A.N., Haley, B.A., McManus, J., 2016. The impact of sedimentary coatings on the diagenetic Nd flux. *Earth Planet Sci. Lett.* 449, 217–227. <https://doi.org/10.1016/j.epsl.2016.06.001>.
- Abbott, A.N., Haley, B.A., McManus, J., Reimers, C.E., 2015b. The sedimentary flux of dissolved rare earth elements to the ocean. *Geochem. Cosmochim. Acta* 154, 186–200. <https://doi.org/10.1016/j.gca.2015.01.010>.
- Abbott, A.N., Löhr, S., Trethewey, M., 2019. Are clay minerals the primary control on the oceanic rare earth element budget? *Front. Mar. Sci.* 6 <https://doi.org/10.3389/fmars.2019.00504>.
- Abrahamsen, E.P., Meijers, A.J.S., Polzin, K.L., Naveira Garabato, A.C., King, B.A., Firing, Y.L., Sallée, J.-B., Sheen, K.L., Gordon, A.L., Huber, B.A., Meredith, M.P., 2019. Stabilization of dense Antarctic water supply to the Atlantic Ocean overturning circulation. *Nat. Clim. Change* 9, 742–746. <https://doi.org/10.1038/s41558-019-0561-2>.
- Adkins, J.F., 2013. The role of deep ocean circulation in setting glacial climates. *Paleoceanography* 28, 539–561. <https://doi.org/10.1002/palo.20046>.
- Ahmad, S.M., Babu, G.A., Padmakumari, V.M., Dayal, A.M., Sukhija, B.S., Nagabhushanam, P., 2005. Sr, Nd isotopic evidence of terrigenous flux variations in the Bay of Bengal: implications of monsoons during the last ~34,000 years. *Geophys. Res. Lett.* 32 <https://doi.org/10.1029/2005GL024519>.
- Albani, S., Mahowald, N.M., Murphy, L.N., Raiswell, R., Moore, J.K., Anderson, R.F., McGee, D., Bradtmiller, L.I., Delmonte, B., Hesse, P.P., Mayewski, P.A., 2016. Paleodust variability since the Last Glacial Maximum and implications for iron inputs to the ocean. *Geophys. Res. Lett.* 43, 3944–3954. <https://doi.org/10.1002/2016GL067911>.
- Amakawa, H., Fukami, Y., Torimoto, J., Nozaki, T., Iijima, K., Usui, A., Suzuki, K., 2018. Origin of Neodymium in the Surface Layer of Ferromanganese Crusts. Presented at the 28th International Ocean and Polar Engineering Conference. International Society of Offshore and Polar Engineers.
- Amakawa, H., Yu, T.-L., Tazoe, H., Obata, H., Gamo, T., Sano, Y., Shen, C.-C., Suzuki, K., 2019. Neodymium concentration and isotopic composition distributions in the southwestern Indian Ocean and the Indian sector of the Southern Ocean. *Chem. Geol.* 511, 190–203. <https://doi.org/10.1016/j.chemgeo.2019.01.007>.
- Amante, C., Eakins, B.W., 2009. ETOPO1 Arc-Minute Global Relief Model: Procedures, Data Sources and Analysis, vol. 24. NOAA technical memorandum NESDIS NGDC.
- Amrhein, D.E., Wunsch, C., Marchal, O., Forget, G., 2018. A global glacial ocean state estimate constrained by upper-Ocean Temperature proxies. *J. Clim.* 31, 8059–8079. <https://doi.org/10.1175/JCLI-D-17-0769.1>.
- Anderson, R.F., Ali, S., Bradtmiller, L.I., Nielsen, S.H.H., Fleisher, M.Q., Anderson, B.E., Burckle, L.H., 2009. Wind-driven upwelling in the Southern Ocean and the deglacial rise in atmospheric  $CO_2$ . *Science* 323, 1443–1448. <https://doi.org/10.1126/science.1167441>.
- Arsouz, T., Dutay, J.-C., Kageyama, M., Lacan, F., Alkama, R., Marti, O., Jeandel, C., 2008. A modeling sensitivity study of the influence of the Atlantic meridional overturning circulation on neodymium isotopic composition at the Last Glacial Maximum. *Clim. Past* 4, 191–203. <https://doi.org/10.5194/cp-4-191-2008>.

- Arsouze, T., Dutay, J.-C., Lacan, F., Jeandel, C., 2009. Reconstructing the Nd oceanic cycle using a coupled dynamical – biogeochemical model. *Biogeosciences* 6, 2829–2846. <https://doi.org/10.5194/bg-6-2829-2009>.
- Arsouze, T., Dutay, J.-C., Lacan, F., Jeandel, C., 2007. Modeling the neodymium isotopic composition with a global ocean circulation model. *Chem. Geol.* 239, 165–177. <https://doi.org/10.1016/j.chemgeo.2006.12.006>.
- Baggenstos, D., Häberli, M., Schmitt, J., Shackleton, S.A., Birner, B., Severinghaus, J.P., Kellerhals, T., Fischer, H., 2019. Earth's radiative imbalance from the Last Glacial Maximum to the present. *Proc. Natl. Acad. Sci. Unit. States Am.* <https://doi.org/10.1073/pnas.1905447116>, 201905447.
- Barth, A., Beckers, J.-M., Troupin, C., Alvera-Azcárate, A., Vandenbulcke, L., 2014. divand-1.0: n-dimensional variational data analysis for ocean observations. *Geosci. Model Dev. (GMD)* 7, 225–241. <https://doi.org/10.5194/gmd-7-225-2014>.
- Basak, C., Fröllje, H., Lamy, F., Gersonde, R., Benz, V., Anderson, R.F., Molina-Kescher, M., Pahnke, K., 2018. Breakup of last glacial deep stratification in the South Pacific. *Science* 359, 900–904. <https://doi.org/10.1126/science.aao2473>.
- Bauska, T.K., Baggenstos, D., Brook, E.J., Mix, A.C., Marcott, S.A., Petrenko, V.V., Schaefer, H., Severinghaus, J.P., Lee, J.E., 2016. Carbon isotopes characterize rapid changes in atmospheric carbon dioxide during the last deglaciation. *Proc. Natl. Acad. Sci. Unit. States Am.* 113, 3465–3470. <https://doi.org/10.1073/pnas.1513868113>.
- Behrens, M.K., Pahnke, K., Schnetger, B., Brumsack, H.-J., 2018. Sources and processes affecting the distribution of dissolved Nd isotopes and concentrations in the West Pacific. *Geochem. Cosmochim. Acta* 222, 508–534. <https://doi.org/10.1016/j.gca.2017.11.008>.
- Bereiter, B., Shackleton, S., Baggenstos, D., Kawamura, K., Severinghaus, J., 2018. Mean global ocean temperatures during the last glacial transition. *Nature* 553, 39. <https://doi.org/10.1038/nature25152>.
- Bertram, C.J., Elderfield, H., 1993. The geochemical balance of the rare earth elements and neodymium isotopes in the oceans. *Geochem. Cosmochim. Acta* 57, 1957–1986. [https://doi.org/10.1016/0016-7037\(93\)90087-D](https://doi.org/10.1016/0016-7037(93)90087-D).
- Blaser, Patrick, Gutjahr, Marcus, Pöppelmeier, Frerk, Frank, Martin, Kaboth-Bahr, Stefanie, Lippold, Jörg, 2020. Labrador Sea bottom water provenance and REE exchange during the past 35,000 years. *Earth Planet Sci. Lett.* 542 <https://doi.org/10.1016/j.epsl.2020.116299>.
- Blaser, P., Lippold, J., Gutjahr, M., Frank, N., Link, J.M., Frank, M., 2016. Extracting foraminiferal seawater Nd isotope signatures from bulk deep sea sediment by chemical leaching. *Chem. Geol.* 439, 189–204. <https://doi.org/10.1016/j.chemgeo.2016.06.024>.
- Blaser, P., Pöppelmeier, F., Schulz, H., Gutjahr, M., Frank, M., Lippold, J., Heinrich, H., Link, J.M., Hoffmann, J., Szidat, S., Frank, N., 2019. The resilience and sensitivity of Northeast Atlantic deep water  $\epsilon_{Nd}$  to overprinting by detrital fluxes over the past 30,000 years. *Geochem. Cosmochim. Acta* 245, 79–97. <https://doi.org/10.1016/j.gca.2018.10.018>.
- Böhm, E., Lippold, J., Gutjahr, M., Frank, M., Blaser, P., Antz, B., Fohlmeister, J., Frank, N., Andersen, M.B., Deininger, M., 2015. Strong and deep Atlantic meridional overturning circulation during the last glacial cycle. *Nature* 517, 73–76. <https://doi.org/10.1038/nature14059>.
- Bond, G., Showers, W., Cheseby, M., Lotti, R., Almasi, P., deMenocal, P., Priore, P., Cullen, H., Hajdas, I., Bonani, G., 1997. A pervasive millennial-scale cycle in North Atlantic Holocene and glacial climates. *Science* 278, 1257–1266. <https://doi.org/10.1126/science.278.5341.1257>.
- Bradtmiller, L.L., McManus, J.F., Robinson, L.F., 2014.  $^{231}\text{Pa}/^{230}\text{Th}$  evidence for a weakened but persistent Atlantic meridional overturning circulation during Heinrich Stadial 1. *Nat. Commun.* 5, 5817. <https://doi.org/10.1038/ncomms6817>.
- Broecker, W., Barker, S., Clark, E., Hajdas, I., Bonani, G., Stott, L., 2004. Ventilation of the glacial deep Pacific ocean. *Science* 306, 1169–1172. <https://doi.org/10.1126/science.1102293>.
- Broecker, W., Clark, E., Barker, S., 2008. Near constancy of the Pacific Ocean surface to mid-depth radiocarbon-age difference over the last 20 kyr. *Earth Planet Sci. Lett.* 274, 322–326. <https://doi.org/10.1016/j.epsl.2008.07.035>.
- Broecker, W.S., 1998. Paleocirculation during the Last Deglaciation: a bipolar seesaw? *Paleoceanography* 13, 119–121. <https://doi.org/10.1029/97PA03707>.
- Broecker, W.S., Takahashi, Taro, Takahashi, Timothy, 1985. Sources and flow patterns of deep-ocean waters as deduced from potential temperature, salinity, and initial phosphate concentration. *J. Geophys. Res. Oceans* 90, 6925–6939. <https://doi.org/10.1029/JC090iC04p06925>.
- Burke, A., Robinson, L.F., 2012. The Southern Ocean's role in carbon exchange during the last deglaciation. *Science* 335, 557–561. <https://doi.org/10.1126/science.1208163>.
- Burton, K.W., Vance, D., 2000. Glacial–interglacial variations in the neodymium isotope composition of seawater in the Bay of Bengal recorded by planktonic foraminifera. *Earth Planet Sci. Lett.* 176, 425–441. [https://doi.org/10.1016/S0012-821X\(00\)00011-X](https://doi.org/10.1016/S0012-821X(00)00011-X).
- Carter, P., Vance, D., Hillenbrand, C.D., Smith, J.A., Shoosmith, D.R., 2012. The neodymium isotopic composition of waters masses in the eastern Pacific sector of the Southern Ocean. *Geochem. Cosmochim. Acta* 79, 41–59. <https://doi.org/10.1016/j.gca.2011.11.034>.
- Chalk, T.B., Foster, G.L., Wilson, P.A., 2019. Dynamic storage of glacial CO<sub>2</sub> in the Atlantic Ocean revealed by boron [CO<sub>3</sub><sup>2-</sup>] and pH records. *Earth Planet Sci. Lett.* 510, 1–11. <https://doi.org/10.1016/j.epsl.2018.12.022>.
- Che, H., Zhang, J., 2018. Water mass analysis and end-member mixing contribution using coupled radiogenic Nd isotopes and Nd concentrations: interaction between marginal seas and the Northwestern Pacific. *Geophys. Res. Lett.* 45, 2388–2395. <https://doi.org/10.1002/2017GL076978>.
- Crocker, A.J., Chalk, T.B., Bailey, I., Spencer, M.R., Gutjahr, M., Foster, G.L., Wilson, P.A., 2016. Geochemical response of the mid-depth Northeast Atlantic Ocean to freshwater input during Heinrich events 1 to 4. *Quat. Sci. Rev.* 151, 236–254. <https://doi.org/10.1016/j.quascirev.2016.08.035>.
- Curry, W.B., Oppo, D.W., 2005. Glacial water mass geometry and the distribution of  $\delta^{13}\text{C}$  of  $\Sigma\text{CO}_2$  in the western Atlantic Ocean. *Paleoceanography* 20, PA1017. <https://doi.org/10.1029/2004PA001021>.
- Davies-Walczak, M., Mix, A.C., Stoner, J.S., Southon, J.R., Cheseby, M., Xuan, C., 2014. Late glacial to Holocene radiocarbon constraints on North Pacific intermediate water ventilation and deglacial atmospheric CO<sub>2</sub> sources. *Earth Planet Sci. Lett.* 397, 57–66. <https://doi.org/10.1016/j.epsl.2014.04.004>.
- de Lavergne, C., Madec, G., Capet, X., Maze, G., Roquet, F., 2016. Getting to the bottom of the ocean. *Nat. Geosci.* 9, 857–858. <https://doi.org/10.1038/ngeo2850>.
- de Lavergne, C., Madec, G., Roquet, F., Holmes, R.M., McDougall, T.J., 2017. Abyssal ocean overturning shaped by seafloor distribution. *Nature* 551, 181–186. <https://doi.org/10.1038/nature24472>.
- Deng, F., Henderson, G.M., Castrillejo, M., Perez, F.F., Steinfeldt, R., 2018. Evolution of  $^{231}\text{Pa}$  and  $^{230}\text{Th}$  in overflow waters of the north Atlantic. *Biogeosciences* 15, 7299–7313. <https://doi.org/10.5194/bg-15-7299-2018>.
- Du, J., Haley, B.A., Mix, A.C., 2016. Neodymium isotopes in authigenic phases, bottom waters and detrital sediments in the Gulf of Alaska and their implications for paleo-circulation reconstruction. *Geochem. Cosmochim. Acta* 193, 14–35. <https://doi.org/10.1016/j.gca.2016.08.005>.
- Du, J., Haley, B.A., Mix, A.C., Walczak, M.H., Praetorius, S.K., 2018. Flushing of the deep Pacific Ocean and the deglacial rise of atmospheric CO<sub>2</sub> concentrations. *Nat. Geosci.* 11, 749–755. <https://doi.org/10.1038/s41561-018-0205-6>.
- Dubois-Dauphin, Q., Colin, C., Bonneau, L., Montagna, P., Wu, Q., Van Rooij, D., Reverdin, G., Douville, E., Thil, F., Waldner, A., Frank, N., 2017. Fingerprinting Northeast Atlantic water masses using neodymium isotopes. *Geochem. Cosmochim. Acta* 210, 267–288. <https://doi.org/10.1016/j.gca.2017.04.002>.
- Duplessy, J.C., Shackleton, N.J., Fairbanks, R.G., Labeyrie, L., Oppo, D., Kallel, N., 1988. Deepwater source variations during the last climatic cycle and their impact on the global deepwater circulation. *Paleoceanography* 3, 343–360. <https://doi.org/10.1029/PA003i003p00343>.
- Elderfield, H., Sholkovitz, E.R., 1987. Rare earth elements in the pore waters of reducing nearshore sediments. *Earth Planet Sci. Lett.* 82, 280–288. [https://doi.org/10.1016/0012-821X\(87\)90202-0](https://doi.org/10.1016/0012-821X(87)90202-0).
- Elmore, A.C., Piotrowski, A.M., Wright, J.D., Scrivner, A.E., 2011. Testing the extraction of past seawater Nd isotopic composition from North Atlantic deep sea sediments and foraminifera. *G-cubed* 12, Q09008. <https://doi.org/10.1029/2011GC003741>.
- Fagel, N., Innocent, C., Stevenson, R.K., Hillaire-Marcel, C., 1999. Deep circulation changes in the Labrador Sea since the last glacial Maximum: new constraints from Sm–Nd data on sediments. *Paleoceanography* 14, 777–788. <https://doi.org/10.1029/1999PA000041>.
- Ferrari, R., 2014. Oceanography: what goes down must come up. *Nature* 513, 179–180. <https://doi.org/10.1038/513179a>.
- Filippova, A., Frank, M., Kienast, M., Rickli, J., Hathorne, E., Yashayev, I.M., Pahnke, K., 2017. Water mass circulation and weathering inputs in the Labrador Sea based on coupled Hf–Nd isotope compositions and rare earth element distributions. *Geochem. Cosmochim. Acta* 199, 164–184. <https://doi.org/10.1016/j.gca.2016.11.024>.
- Frank, M., 2002. Radiogenic isotopes: tracers of past ocean circulation and erosional input. *Rev. Geophys.* 40, 1001. <https://doi.org/10.1029/2000RG000094>.
- Friedrich, T., Timmermann, A., Stichel, T., Pahnke, K., 2014. Ocean circulation reconstructions from  $\epsilon_{Nd}$ : a model-based feasibility study. *Paleoceanography* 29, 1003–1023. <https://doi.org/10.1002/2014PA002658>.
- García-Solsona, E., Jeandel, C., 2020. Balancing rare earth element distributions in the Northwestern Mediterranean Sea. *Chem. Geol.* 532, 119372. <https://doi.org/10.1016/j.chemgeo.2019.119372>.
- Gardner, W.D., Jo Richardson, M., Mishonov, A.V., Biscaye, P.E., 2018. Global comparison of benthic nepheloid layers based on 52 years of nephelometer and transmissometer measurements. *Prog. Oceanogr.* 168, 100–111. <https://doi.org/10.1016/j.pocan.2018.09.008>.
- Gebbie, G., 2014. How much did Glacial North Atlantic Water shoal? *Paleoceanography* 29, 190–209. <https://doi.org/10.1002/2013PA002557>.
- Gebbie, G., Huybers, P., 2012. The mean age of ocean waters inferred from radiocarbon observations: sensitivity to surface sources and accounting for mixing histories. *J. Phys. Oceanogr.* 42, 291–305. <https://doi.org/10.1175/JPO-D-11-043.1>.
- Gebbie, G., Huybers, P., 2010. Total matrix Intercomparison: a method for determining the geometry of water-mass pathways. *J. Phys. Oceanogr.* 40, 1710–1728. <https://doi.org/10.1175/2010JPO472.1>.
- German, C.R., Elderfield, H., 1989. Rare earth elements in Saanich Inlet, British Columbia, a seasonally anoxic basin. *Geochem. Cosmochim. Acta* 53, 2561–2571. [https://doi.org/10.1016/0016-7037\(89\)90128-2](https://doi.org/10.1016/0016-7037(89)90128-2).
- Goldstein, S.J., Jacobsen, S.B., 1987. The Nd and Sr isotopic systematics of river-water dissolved material: implications for the sources of Nd and Sr in seawater. *Chem. Geol. Isot. Geosci.* 66, 245–272. [https://doi.org/10.1016/0168-9622\(87\)90045-5](https://doi.org/10.1016/0168-9622(87)90045-5).
- Goldstein, S.L., Hemming, S.R., 2003. Long-lived isotopic tracers in oceanography, paleoceanography, and ice-sheet dynamics. In: Holland, H.D., Turekian, K.K. (Eds.), *Treatise on Geochemistry*. Pergamon, Oxford, pp. 453–489.
- Goldstein, S.L., Onions, R.K., Hamilton, P.J., 1984. A Sm–Nd isotopic study of

- atmospheric dusts and particulates from major river systems. *Earth Planet Sci. Lett.* 70, 221–236. [https://doi.org/10.1016/0012-821X\(84\)90007-4](https://doi.org/10.1016/0012-821X(84)90007-4).
- Goswami, V., Singh, S.K., Bhushan, R., Rai, V.K., 2012. Temporal variations in  $^{87}\text{Sr}/^{86}\text{Sr}$  and  $\epsilon_{\text{Nd}}$  in sediments of the southeastern Arabian Sea: impact of monsoon and surface water circulation. *G-cubed* 13, Q01001. <https://doi.org/10.1029/2011GC003802>.
- Grasse, P., Bosse, L., Hathorne, E.C., Böning, P., Pahnke, K., Frank, M., 2017. Short-term variability of dissolved rare earth elements and neodymium isotopes in the entire water column of the Panama Basin. *Earth Planet Sci. Lett.* 475, 242–253. <https://doi.org/10.1016/j.epsl.2017.07.022>.
- Grenier, M., Francois, R., Soon, M., van der Loeff, M.R., Yu, X., Valk, O., Not, C., Moran, S.B., Edwards, R.L., Lu, Y., LePore, K., Allen, S.E., 2019. Changes in circulation and particle scavenging in the Amerasian Basin of the Arctic Ocean over the last three decades inferred from the water column distribution of geochemical tracers. *J. Geophys. Res. Oceans* n/a. <https://doi.org/10.1029/2019JC015265>.
- Grenier, M., Garcia-Solsona, E., Lemaitre, N., Trull, T.W., Bouvier, V., Nonnotte, P., van Beek, P., Souhaut, M., Lacan, F., Jeandel, C., 2018. Differentiating lithogenic supplies, water mass transport, and biological processes on and off the Kerguelen plateau using rare earth element concentrations and neodymium isotopic compositions. *Front. Mar. Sci.* 5 <https://doi.org/10.3389/fmars.2018.00426>.
- Grousset, F.E., Biscaye, P.E., 2005. Tracing dust sources and transport patterns using Sr, Nd and Pb isotopes. *Chem. Geol.* 222, 149–167. <https://doi.org/10.1016/j.chemgeo.2005.05.006>.
- Grousset, F.E., Cortijo, E., Huon, S., Hervé, L., Richter, T., Burdloff, D., Duprat, J., Weber, O., 2001. Zooming in on Heinrich layers. *Paleoceanography* 16, 240–259. <https://doi.org/10.1029/2000PA000559>.
- Grousset, F.E., Parra, M., Bory, A., Martinez, P., Bertrand, P., Shimmield, G., Ellam, R.M., 1998. Saharan wind regimes traced by the Sr–Nd isotopic composition of subtropical Atlantic sediments: last glacial maximum vs today. *Quat. Sci. Rev.* 17, 395–409. [https://doi.org/10.1016/S0277-3791\(97\)00048-6](https://doi.org/10.1016/S0277-3791(97)00048-6).
- Grousset, F.E., Pujol, C., Labeyrie, L., Auffret, G., Boelaert, A., 2000. Were the North Atlantic Heinrich events triggered by the behavior of the European ice sheets? *Geology* 28, 123–126. [https://doi.org/10.1130/0091-7613\(2000\)28<123:WTNAHE>2.0.CO;2](https://doi.org/10.1130/0091-7613(2000)28<123:WTNAHE>2.0.CO;2).
- Gu, S., Liu, Z., Jahn, A., Rempfer, J., Zhang, J., Joos, F., 2019. Modeling neodymium isotopes in the ocean component of the community earth system model (CESM1). *J. Adv. Model. Earth Syst.* 11, 624–640. <https://doi.org/10.1029/2018MS001538>.
- Gu, S., Liu, Z., Oppo, D.W., Lynch-Stieglitz, J., Jahn, A., Zhang, J., Wu, L., 2020. Assessing the potential capability of reconstructing glacial Atlantic water masses and AMOC using multiple proxies in CESM. *Earth Planet Sci. Lett.* 541, 116294. <https://doi.org/10.1016/j.epsl.2020.116294>.
- Gu, S., Liu, Z., Zhang, J., Rempfer, J., Joos, F., Oppo, D.W., 2017. Coherent response of Antarctic intermediate water and Atlantic meridional overturning circulation during the last deglaciation: reconciling contrasting neodymium isotope reconstructions from the tropical Atlantic. *Paleoceanography* 32. <https://doi.org/10.1002/2017PA003092>, 2017PA003092.
- Gutjahr, M., Frank, M., Stirling, C.H., Keigwin, L.D., Halliday, A.N., 2008. Tracing the Nd isotope evolution of north Atlantic deep and intermediate waters in the western North Atlantic since the last glacial Maximum from Blake ridge sediments. *Earth Planet Sci. Lett.* 266, 61–77. <https://doi.org/10.1016/j.epsl.2007.10.037>.
- Gutjahr, M., Frank, M., Stirling, C.H., Klemm, V., van de Fliedert, T., Halliday, A.N., 2007. Reliable extraction of a deepwater trace metal isotope signal from Fe–Mn oxyhydroxide coatings of marine sediments. *Chem. Geol.* 242, 351–370. <https://doi.org/10.1016/j.chemgeo.2007.03.021>.
- Haley, B.A., Du, J., Abbott, A.N., McManus, J., 2017. The impact of benthic processes on rare earth element and neodymium isotope distributions in the oceans. *Front. Mar. Sci.* 4 <https://doi.org/10.3389/fmars.2017.00426>.
- Haley, B.A., Frank, M., Hathorne, E., Piasias, N., 2014. Biogeochemical implications from dissolved rare earth element and Nd isotope distributions in the Gulf of Alaska. *Geochem. Cosmochim. Acta* 126, 455–474. <https://doi.org/10.1016/j.gca.2013.11.012>.
- Haley, B.A., Klinkhammer, G.P., 2003. Complete separation of rare earth elements from small volume seawater samples by automated ion chromatography: method development and application to benthic flux. *Mar. Chem.* 82, 197–220. [https://doi.org/10.1016/S0304-4203\(03\)00070-7](https://doi.org/10.1016/S0304-4203(03)00070-7).
- Haley, B.A., Klinkhammer, G.P., McManus, J., 2004. Rare earth elements in pore waters of marine sediments. *Geochem. Cosmochim. Acta* 68, 1265–1279. <https://doi.org/10.1016/j.gca.2003.09.012>.
- Hein, C.J., Galy, V., Galy, A., France-Lanord, C., Kudrass, H., Schwenk, T., 2017. Post-glacial climate forcing of surface processes in the Ganges–Brahmaputra river basin and implications for carbon sequestration. *Earth Planet Sci. Lett.* 478, 89–101. <https://doi.org/10.1016/j.epsl.2017.08.013>.
- Hemming, S.R., 2004. Heinrich events: massive late Pleistocene detritus layers of the North Atlantic and their global climate imprint. *Rev. Geophys.* 42 <https://doi.org/10.1029/2003RG000128>.
- Hemming, S.R., Broecker, W.S., Sharp, W.D., Bond, G.C., Gwiazda, R.H., McManus, J.F., Klas, M., Hajdas, I., 1998. Provenance of Heinrich layers in core V28–82, northeastern Atlantic:  $^{40}\text{Ar}/^{39}\text{Ar}$  ages of ice-rafted hornblende, Pb isotopes in feldspar grains, and Nd–Sr–Pb isotopes in the fine sediment fraction. *Earth Planet Sci. Lett.* 164, 317–333. [https://doi.org/10.1016/S0012-821X\(98\)00224-6](https://doi.org/10.1016/S0012-821X(98)00224-6).
- Hillaire-Marcel, C., de Vernal, A., Bilodeau, G., Weaver, A.J., 2001. Absence of deep-water formation in the Labrador Sea during the last interglacial period. *Nature* 410, 1073–1077. <https://doi.org/10.1038/35074059>.
- Hodell, D.A., Nicholl, J.A., Bontognali, T.R.R., Danino, S., Dorador, J., Dowdeswell, J.A., Einsle, J., Kuhlmann, H., Martrat, B., Mleneck-Vautravets, M.J., Rodríguez-Tovar, F.J., Röhl, U., 2017. Anatomy of Heinrich Layer 1 and its role in the last deglaciation. *Paleoceanography* 32, 284–303. <https://doi.org/10.1002/2016PA003028>.
- Horikawa, K., Martin, E.E., Asahara, Y., Sagawa, T., 2011. Limits on conservative behavior of Nd isotopes in seawater assessed from analysis of fish teeth from Pacific core tops. *Earth Planet Sci. Lett.* 310, 119–130. <https://doi.org/10.1016/j.epsl.2011.07.018>.
- Howe, J.N.W., Huang, K.-F., Oppo, D.W., Chiessi, C.M., Mulitza, S., Blusztajn, J., Piotrowski, A.M., 2018. Similar mid-depth Atlantic water mass provenance during the last glacial Maximum and Heinrich stadial 1. *Earth Planet Sci. Lett.* 490, 51–61. <https://doi.org/10.1016/j.epsl.2018.03.006>.
- Howe, J.N.W., Piotrowski, A.M., Noble, T.L., Mulitza, S., Chiessi, C.M., Bayon, G., 2016a. North Atlantic deep water circulation during the last glacial Maximum. *Nat. Commun.* 7, 11765. <https://doi.org/10.1038/ncomms11765>.
- Howe, J.N.W., Piotrowski, A.M., Oppo, D.W., Huang, K.-F., Mulitza, S., Chiessi, C.M., Blusztajn, J., 2016b. Antarctic intermediate water circulation in the South Atlantic over the past 25,000 years. *Paleoceanography* 31, 1302–1314. <https://doi.org/10.1002/2016PA002975>.
- Hu, R., Piotrowski, A.M., 2018. Neodymium isotope evidence for glacial-interglacial variability of deepwater transit time in the Pacific Ocean. *Nat. Commun.* 9, 4709. <https://doi.org/10.1038/s41467-018-07079-z>.
- Huang, H., Gutjahr, M., Eisenhauer, A., Kuhn, G., 2020. No detectable Weddell Sea Antarctic bottom water export during the last and penultimate glacial Maximum. *Nat. Commun.* 11, 1–10. <https://doi.org/10.1038/s41467-020-14302-3>.
- Huang, K.-F., Oppo, D.W., Curry, W.B., 2014. Decreased influence of Antarctic intermediate water in the tropical Atlantic during North Atlantic cold events. *Earth Planet Sci. Lett.* 389, 200–208. <https://doi.org/10.1016/j.epsl.2013.12.037>.
- Ivanovic, R.F., Gregoire, L.J., Burke, A., Wickert, A.D., Valdes, P.J., Ng, H.C., Robinson, L.F., McManus, J.F., Mitrovica, J.X., Lee, L., Dentith, J.E., 2018. Acceleration of northern ice sheet melt during deglaciation. *Paleoceanogr. Paleoclimatol.* 33, 807–824. <https://doi.org/10.1029/2017PA003308>.
- Jacobel, A.W., Anderson, R.F., Jaccard, S.L., McManus, J.F., Pavia, F.J., Winckler, G., 2020. Deep Pacific storage of respired carbon during the last ice age: perspectives from bottom water oxygen reconstructions. *Quat. Sci. Rev.* 230, 106065. <https://doi.org/10.1016/j.quascirev.2019.106065>.
- Jacobsen, S.B., Wasserburg, G.J., 1980. Sm–Nd isotopic evolution of chondrites. *Earth Planet Sci. Lett.* 50, 139–155. [https://doi.org/10.1016/0012-821X\(80\)90125-9](https://doi.org/10.1016/0012-821X(80)90125-9).
- Jeandel, C., Arsouze, T., Lacan, F., Techine, P., Dutay, J., 2007. Isotopic Nd compositions and concentrations of the lithogenic inputs into the ocean: a compilation, with an emphasis on the margins. *Chem. Geol.* 239, 156–164. <https://doi.org/10.1016/j.chemgeo.2006.11.013>.
- Johannesson, K.H., Burdige, D.J., 2007. Balancing the global oceanic neodymium budget: evaluating the role of groundwater. *Earth Planet Sci. Lett.* 253, 129–142. <https://doi.org/10.1016/j.epsl.2006.10.021>.
- Jones, K.M., Khatiwala, S.P., Goldstein, S.L., Hemming, S.R., van de Fliedert, T., 2008. Modeling the distribution of Nd isotopes in the oceans using an ocean general circulation model. *Earth Planet Sci. Lett.* 272, 610–619. <https://doi.org/10.1016/j.epsl.2008.05.027>.
- Jonkers, L., Zahn, R., Thomas, A., Henderson, G., Abouchami, W., François, R., Masque, P., Hall, I.R., Bickert, T., 2015. Deep circulation changes in the central South Atlantic during the past 145 kyr reflected in a combined  $^{231}\text{Pa}/^{230}\text{Th}$ , Neodymium isotope and benthic  $\delta^{13}\text{C}$  record. *Earth Planet Sci. Lett.* 419, 14–21. <https://doi.org/10.1016/j.epsl.2015.03.004>.
- Josse, J., Husson, F., 2016. missMDA: a package for handling missing values in multivariate data analysis. *J. Stat. Software* 70, 1–31. <https://doi.org/10.18637/jss.v070.i01>.
- Jullien, E., Grousset, F.E., Hemming, S.R., Peck, V.L., Hall, I.R., Jeantet, C., Billy, I., 2006. Contrasting conditions preceding MIS3 and MIS2 Heinrich events. *Global Planet. Change* 54, 225–238. <https://doi.org/10.1016/j.gloplacha.2006.06.021>.
- Keigwin, L.D., Swift, S.A., 2017. Carbon isotope evidence for a northern source of deep water in the glacial western North Atlantic. *Proc. Natl. Acad. Sci. Unit. States Am.* 201614693 <https://doi.org/10.1073/pnas.1614693114>.
- Kurahashi-Nakamura, T., Paul, A., Losch, M., 2017. Dynamical reconstruction of the global ocean state during the Last Glacial Maximum. *Paleoceanography* 32, 326–350. <https://doi.org/10.1002/2016PA003001>.
- Kwon, E.Y., Hain, M.P., Sigman, D.M., Galbraith, E.D., Sarmiento, J.L., Toggweiler, J.R., 2012. North Atlantic ventilation of “southern-sourced” deep water in the glacial ocean. *Paleoceanography* 27, PA2208. <https://doi.org/10.1029/2011PA002211>.
- Lacan, F., Jeandel, C., 2005a. Neodymium isotopes as a new tool for quantifying exchange fluxes at the continent–ocean interface. *Earth Planet Sci. Lett.* 232, 245–257. <https://doi.org/10.1016/j.epsl.2005.01.004>.
- Lacan, F., Jeandel, C., 2005b. Acquisition of the neodymium isotopic composition of the north Atlantic deep water. *G-cubed* 6, Q12008. <https://doi.org/10.1029/2005GC000956>.
- Lacan, F., Jeandel, C., 2004a. Denmark Strait water circulation traced by heterogeneity in neodymium isotopic compositions. *Deep-Sea Res. Part A Oceanogr. Res. Pap.* 51, 71–82. <https://doi.org/10.1016/j.dsr.2003.09.006>.
- Lacan, F., Jeandel, C., 2004b. Neodymium isotopic composition and rare earth element concentrations in the deep and intermediate Nordic Seas: constraints on the Iceland Scotland Overflow Water signature. *G-cubed* 5, Q11006. <https://doi.org/10.1029/2003GC000956>.

- [doi.org/10.1029/2004GC000742](https://doi.org/10.1029/2004GC000742).
- Lacan, F., Tachikawa, K., Jeandel, C., 2012. Neodymium isotopic composition of the oceans: a compilation of seawater data. *Chem. Geol.* 300–301, 177–184. <https://doi.org/10.1016/j.chemgeo.2012.01.019>.
- Lacerra, M., Lund, D., Yu, J., Schmittner, A., 2017. Carbon storage in the mid-depth Atlantic during millennial-scale climate events. *Paleoceanography* 32, 780–795. <https://doi.org/10.1002/2016PA003081>.
- Lambelet, M., Flierdt, T., van de, Butler, E.C.V., Bowie, A.R., Rintoul, S.R., Watson, R.J., Remenyi, T., Lannuzel, D., Warner, M., Robinson, L.F., Bostock, H.C., Brattmiller, L.L., 2018. The neodymium isotope fingerprint of Adélie coast bottom water. *Geophys. Res. Lett.* 45 (11) <https://doi.org/10.1029/2018GL080074>, 247–11,256.
- Lambelet, M., van de Flierdt, T., Crockett, K., Rehkämper, M., Kreissig, K., Coles, B., Rijkenberg, M.J.A., Gerringa, L.J.A., de Baar, H.J.W., Steinfeldt, R., 2016. Neodymium isotopic composition and concentration in the western North Atlantic Ocean: results from the GEOTRACES GA02 section. *Geochem. Cosmochim. Acta* 177, 1–29. <https://doi.org/10.1016/j.gca.2015.12.019>.
- Lambert, F., Tagliabue, A., Shaffer, G., Lamy, F., Winckler, G., Farias, L., Gallardo, L., Pol-Holz, R.D., 2018. Dust fluxes and iron fertilization in Holocene and last glacial Maximum climates. *Geophys. Res. Lett.* 42, 6014–6023. <https://doi.org/10.1002/2015GL064250>.
- Lang, D.C., Bailey, I., Wilson, P.A., Chalk, T.B., Foster, G.L., Gutjahr, M., 2016. Incursions of southern-sourced water into the deep North Atlantic during late Pliocene glacial intensification. *Nat. Geosci.* 9, 375–379. <https://doi.org/10.1038/ngeo2688>.
- Laukert, G., Frank, M., Bauch, D., Hathorne, E.C., Gutjahr, M., Janout, M., Hölemann, J., 2017a. Transport and transformation of riverine neodymium isotope and rare earth element signatures in high latitude estuaries: a case study from the Laptev Sea. *Earth Planet Sci. Lett.* 477, 205–217. <https://doi.org/10.1016/j.epsl.2017.08.010>.
- Laukert, G., Frank, M., Bauch, D., Hathorne, E.C., Rabe, B., von Appen, W.-J., Wegner, C., Zieringer, M., Kassens, H., 2017b. Ocean circulation and freshwater pathways in the Arctic Mediterranean based on a combined Nd isotope, REE and oxygen isotope section across Fram Strait. *Geochem. Cosmochim. Acta* 202, 285–309. <https://doi.org/10.1016/j.gca.2016.12.028>.
- Laukert, G., Makhotin, M., Petrova, M.V., Frank, M., Hathorne, E.C., Bauch, D., Böning, P., Kassens, H., 2018. Water mass transformation in the Barents Sea inferred from radiogenic neodymium isotopes, rare earth elements and stable oxygen isotopes. *Chem. Geol.* <https://doi.org/10.1016/j.chemgeo.2018.10.002>.
- Lê, S., Josse, J., Husson, F., 2008. FactoMineR: an R package for multivariate analysis. *J. Stat. Software* 25, 1–18. <https://doi.org/10.18637/jss.v025.i01>.
- Lippold, J., Gutjahr, M., Blaser, P., Christner, E., de Carvalho Ferreira, M.L., Mulitza, S., Christl, M., Wombacher, F., Böhm, E., Antz, B., Cartapanis, O., Vogel, H., Jaccard, S.L., 2016. Deep water provenance and dynamics of the (de)glacial Atlantic meridional overturning circulation. *Earth Planet Sci. Lett.* 445, 68–78. <https://doi.org/10.1016/j.epsl.2016.04.013>.
- Lippold, J., Luo, Y., Francois, R., Allen, S.E., Gherardi, J., Pichat, S., Hickey, B., Schulz, H., 2012. Strength and geometry of the glacial Atlantic meridional overturning circulation. *Nat. Geosci.* 5, 813–816. <https://doi.org/10.1038/ngeo1608>.
- Lippold, J., Pöppelmeier, F., Süfke, F., Gutjahr, M., Goepfert, T.J., Blaser, P., Friedrich, O., Link, J.M., Wacker, L., Rheinberger, S., Jaccard, S.L., 2019. Constraining the variability of the Atlantic meridional overturning circulation during the Holocene. *Geophys. Res. Lett.* 46, 11338–11346. <https://doi.org/10.1029/2019GL084988>.
- Liu, J., He, W., Cao, L., Zhu, Z., Xiang, R., Li, T., Shi, X., Liu, S., 2019. Staged fine-grained sediment supply from the Himalayas to the Bengal Fan in response to climate change over the past 50,000 years. *Quat. Sci. Rev.* 212, 164–177. <https://doi.org/10.1016/j.quascirev.2019.04.008>.
- Lund, D.C., 2013. Deep Pacific ventilation ages during the last deglaciation: evaluating the influence of diffusive mixing and source region reservoir age. *Earth Planet Sci. Lett.* 381, 52–62. <https://doi.org/10.1016/j.epsl.2013.08.032>.
- Lund, D.C., Mix, A.C., Southon, J., 2011. Increased ventilation age of the deep northeast Pacific Ocean during the last deglaciation. *Nat. Geosci.* 4, 771–774. <https://doi.org/10.1038/ngeo1272>.
- Lund, D.C., Tassin, A.C., Hoffman, J.L., Schmittner, A., 2015. Southwest Atlantic water mass evolution during the last deglaciation. *Paleoceanography* 30, 477–494. <https://doi.org/10.1002/2014PA002657>.
- Lynch-Stieglitz, J., Valley, S.G., Schmidt, M.W., 2019. Temperature-dependent ocean–atmosphere equilibration of carbon isotopes in surface and intermediate waters over the deglaciation. *Earth Planet Sci. Lett.* 506, 466–475. <https://doi.org/10.1016/j.epsl.2018.11.024>.
- Mahowald, N.M., Baker, A.R., Bergametti, G., Brooks, N., Duce, R.A., Jickells, T.D., Kubilay, N., Prospero, J.M., Tegen, I., 2005. Atmospheric global dust cycle and iron inputs to the ocean. *Global Biogeochem. Cycles* 19. <https://doi.org/10.1029/2004GB002402>.
- Marchitto, T.M., Lehman, S.J., Ortiz, J.D., Flückiger, J., Geen, A. van, 2007. Marine radiocarbon evidence for the mechanism of deglacial atmospheric CO<sub>2</sub> rise. *Science* 316, 1456–1459. <https://doi.org/10.1126/science.1138679>.
- Marcott, S.A., Bauska, T.K., Buizert, C., Steig, E.J., Rosen, J.L., Cuffey, K.M., Fudge, T.J., Severinghaus, J.P., Ahn, J., Kalk, M.L., McConnell, J.R., Sowers, T., Taylor, K.C., White, J.W.C., Brook, E.J., 2014. Centennial-scale changes in the global carbon cycle during the last deglaciation. *Nature* 514, 616–619. <https://doi.org/10.1038/nature13799>.
- Marinov, I., Gnanadesikan, A., Toggweiler, J.R., Sarmiento, J.L., 2006. The Southern Ocean biogeochemical divide. *Nature* 441, 964–967. <https://doi.org/10.1038/nature04883>.
- Marshall, J., Speer, K., 2012. Closure of the meridional overturning circulation through Southern Ocean upwelling. *Nat. Geosci.* 5, 171–180. <https://doi.org/10.1038/ngeo1391>.
- McManus, J.F., Francois, R., Gherardi, J.-M., Keigwin, L.D., Brown-Leger, S., 2004. Collapse and rapid resumption of Atlantic meridional circulation linked to deglacial climate changes. *Nature* 428, 834–837. <https://doi.org/10.1038/nature02494>.
- Meijers, A.J.S., 2014. The Southern Ocean in the coupled model Intercomparison project phase 5. *Philos. Trans. R. Soc. A* 372, 20130296. <https://doi.org/10.1098/rsta.2013.0296>.
- Meile, C., Cappellen, P.V., 2003. Global estimates of enhanced solute transport in marine sediments. *Limnol. Oceanogr.* 48, 777–786. <https://doi.org/10.4319/lo.2003.48.2.0777>.
- Menviel, L., England, M.H., Meissner, K.J., Mouchet, A., Yu, J., 2014. Atlantic-Pacific seesaw and its role in outgassing CO<sub>2</sub> during Heinrich events. *Paleoceanography* 29, 58–70. <https://doi.org/10.1002/2013PA002542>.
- Menviel, L., Spence, P., Yu, J., Chamberlain, M.A., Matear, R.J., Meissner, K.J., England, M.H., 2018. Southern Hemisphere westerlies as a driver of the early deglacial atmospheric CO<sub>2</sub> rise. *Nat. Commun.* 9, 2503. <https://doi.org/10.1038/s41467-018-04876-4>.
- Menviel, L., Yu, J., Joos, F., Mouchet, A., Meissner, K.J., England, M.H., 2016. Poorly ventilated deep ocean at the Last Glacial Maximum inferred from carbon isotopes: a data-model comparison study. *Paleoceanography* 32, 2–17. <https://doi.org/10.1002/2016PA003024>.
- Middleton, J.L., Mukhopadhyay, S., Langmuir, C.H., McManus, J.F., Huybers, P.J., 2018. Millennial-scale variations in dustiness recorded in Mid-Atlantic sediments from 0 to 70 ka. *Earth Planet Sci. Lett.* 482, 12–22. <https://doi.org/10.1016/j.epsl.2017.10.034>.
- Mix, A.C., Fairbanks, R.G., 1985. North Atlantic surface-ocean control of Pleistocene deep-ocean circulation. *Earth Planet Sci. Lett.* 73, 231–243. [https://doi.org/10.1016/0012-821X\(85\)90072-X](https://doi.org/10.1016/0012-821X(85)90072-X).
- Molina-Kescher, M., Hathorne, E.C., Osborne, A.H., Behrens, M.K., Kölling, M., Pahnke, K., Frank, M., 2018. The influence of basaltic islands on the oceanic REE distribution: a case study from the tropical South Pacific. *Front. Mar. Sci.* 5 <https://doi.org/10.3389/fmars.2018.00050>.
- Morrison, R., Waldner, A., Hathorne, E.C., Rahlf, P., Zieringer, M., Montagna, P., Colin, C., Frank, M., 2018. Limited influence of basalt weathering inputs on the seawater neodymium isotope composition of the northern Iceland Basin. *Chem. Geol.* <https://doi.org/10.1016/j.chemgeo.2018.10.019>.
- Muglia, J., Schmittner, A., 2015. Glacial Atlantic overturning increased by wind stress in climate models. *Geophys. Res. Lett.* 42, 9862–9868. <https://doi.org/10.1002/2015GL064583>.
- Muglia, J., Skinner, L.C., Schmittner, A., 2018. Weak overturning circulation and high Southern Ocean nutrient utilization maximized glacial ocean carbon. *Earth Planet Sci. Lett.* 496, 47–56. <https://doi.org/10.1016/j.epsl.2018.05.038>.
- Naik, S.S., Basak, C., Goldstein, S.L., Naidu, P.D., Naik, S.N., 2019. A 16-kyr record of ocean circulation and monsoon intensification from the central Bay of Bengal. *G-cubed* 20, 872–882. <https://doi.org/10.1029/2018GC007860>.
- Negre, C., Zahn, R., Thomas, A.L., Masqué, P., Henderson, G.M., Martínez-Méndez, G., Hall, I.R., Mas, J.L., 2010. Reversed flow of Atlantic deep water during the last glacial Maximum. *Nature* 468, 84–88. <https://doi.org/10.1038/nature09508>.
- Ng, H.C., Robinson, L.F., McManus, J.F., Mohamed, K.J., Jacobel, A.W., Ivanovic, R.F., Gregoire, L.J., Chen, T., 2018. Coherent deglacial changes in western Atlantic Ocean circulation. *Nat. Commun.* 9, 2947. <https://doi.org/10.1038/s41467-018-05312-3>.
- Okazaki, Y., Timmermann, A., Menviel, L., Harada, N., Abe-Ouchi, A., Chikamoto, M.O., Mouchet, A., Asahi, H., 2010. Deepwater formation in the north pacific during the last glacial termination. *Science* 329, 200–204. <https://doi.org/10.1126/science.1190612>.
- Oppo, D.W., Fairbanks, R.G., 1987. Variability in the deep and intermediate water circulation of the Atlantic Ocean during the past 25,000 years: northern Hemisphere modulation of the Southern Ocean. *Earth Planet Sci. Lett.* 86, 1–15. [https://doi.org/10.1016/0012-821X\(87\)90183-X](https://doi.org/10.1016/0012-821X(87)90183-X).
- Oppo, D.W., Gebbie, G., Huang, K.-F., Curry, W.B., Marchitto, T.M., Pietro, K.R., 2018. Data constraints on glacial Atlantic water mass geometry and properties. *Paleoceanogr. Paleoclimatol.* 33, 1013–1034. <https://doi.org/10.1029/2018PA003408>.
- Osborne, A.H., Haley, B.A., Hathorne, E.C., Flögel, S., Frank, M., 2014. Neodymium isotopes and concentrations in Caribbean seawater: tracing water mass mixing and continental input in a semi-enclosed ocean basin. *Earth Planet Sci. Lett.* 406, 174–186. <https://doi.org/10.1016/j.epsl.2014.09.011>.
- Otto-Bliessner, B.L., Hewitt, C.D., Marchitto, T.M., Brady, E., Abe-Ouchi, A., Crucifix, M., Murakami, S., Weber, S.L., 2007. Last Glacial Maximum ocean thermohaline circulation: PMIP2 model intercomparisons and data constraints. *Geophys. Res. Lett.* 34 <https://doi.org/10.1029/2007GL029475>.
- Pahnke, K., Goldstein, S.L., Hemming, S.R., 2008. Abrupt changes in Antarctic Intermediate Water circulation over the past 25,000 years. *Nat. Geosci.* 1, 870–874. <https://doi.org/10.1038/ngeo0360>.
- Peck, V.L., Hall, I.R., Zahn, R., Elderfield, H., Grousset, F., Hemming, S.R., Scourse, J.D., 2006. High resolution evidence for linkages between NW European ice sheet instability and Atlantic Meridional Overturning Circulation. *Earth Planet Sci. Lett.* 243, 476–488. <https://doi.org/10.1016/j.epsl.2005.12.023>.
- Piepgras, D.J., Jacobsen, S.B., 1988. The isotopic composition of neodymium in the

- North Pacific. *Geochem. Cosmochim. Acta* 52, 1373–1381. [https://doi.org/10.1016/0016-7037\(88\)90208-6](https://doi.org/10.1016/0016-7037(88)90208-6).
- Piepgas, D.J., Wasserburg, G.J., 1987. Rare earth element transport in the western North Atlantic inferred from Nd isotopic observations. *Geochem. Cosmochim. Acta* 51, 1257–1271. [https://doi.org/10.1016/0016-7037\(87\)90217-1](https://doi.org/10.1016/0016-7037(87)90217-1).
- Piepgas, D.J., Wasserburg, G.J., 1982. Isotopic composition of neodymium in waters from the drake passage. *Science* 217, 207–214. <https://doi.org/10.1126/science.217.4556.207>.
- Piepgas, D.J., Wasserburg, G.J., 1980. Neodymium isotopic variations in seawater. *Earth Planet Sci. Lett.* 50, 128–138. [https://doi.org/10.1016/0012-821X\(80\)90124-7](https://doi.org/10.1016/0012-821X(80)90124-7).
- Piotrowski, A.M., Banakar, V.K., Scrivner, A.E., Elderfield, H., Galy, A., Dennis, A., 2009. Indian Ocean circulation and productivity during the last glacial cycle. *Earth Planet Sci. Lett.* 285, 179–189. <https://doi.org/10.1016/j.epsl.2009.06.007>.
- Piotrowski, A.M., Goldstein, S.L., Hemming, S.R., Fairbanks, R.G., 2005. Temporal relationships of carbon cycling and ocean circulation at glacial boundaries. *Science* 307, 1933–1938. <https://doi.org/10.1126/science.1104883>.
- Piotrowski, A.M., Goldstein, S.L., Hemming, S.R., Fairbanks, R.G., 2004. Intensification and variability of ocean thermohaline circulation through the last deglaciation. *Earth Planet Sci. Lett.* 225, 205–220. <https://doi.org/10.1016/j.epsl.2004.06.002>.
- Plaza-Morlote, M., Rey, D., Santos, J.F., Ribeiro, S., Heslop, D., Bernabeu, A., Mohamed, K.J., Rubio, B., Martins, V., 2017. Southernmost evidence of large European ice sheet-derived freshwater discharges during the Heinrich stadials of the last glacial period (Galician interior basin, northwest Iberian continental margin). *Earth Planet Sci. Lett.* 457, 213–226. <https://doi.org/10.1016/j.epsl.2016.10.020>.
- Poggemann, D.-W., Nürnberg, D., Hathorne, E.C., Frank, M., Rath, W., Reißig, S., Bahr, A., 2018. Deglacial heat uptake by the Southern Ocean and rapid northward redistribution via Antarctic intermediate water. *Paleoceanogr. Paleoclimatol.* 33, 1292–1305. <https://doi.org/10.1029/2017PA003284>.
- Pöppelmeier, F., Blaser, P., Gutjahr, M., Süfke, F., Thornalley, D.J.R., Grützner, J., Jakob, K.A., Link, J.M., Szidat, S., Lippold, J., 2019. Influence of ocean circulation and benthic exchange on deep northwest Atlantic Nd isotope records during the past 30,000 years. *G-cubed* 20, 4457–4469. <https://doi.org/10.1029/2019GC008271>.
- Pöppelmeier, F., Gutjahr, M., Blaser, P., Oppo, D.W., Jaccard, S.L., Regelous, M., Huang, K.-F., Süfke, F., Lippold, J., 2020. Water mass gradients of the mid-depth Southwest Atlantic during the past 25,000 years. *Earth Planet Sci. Lett.* 531, 115963. <https://doi.org/10.1016/j.epsl.2019.115963>.
- Purkey, S.G., Johnson, G.C., 2013. Antarctic bottom water warming and freshening: contributions to sea level rise, ocean freshwater budgets, and global heat gain. *J. Clim.* 26, 6105–6122. <https://doi.org/10.1175/JCLI-D-12-00834.1>.
- Rae, J.W.B., Broecker, W., 2018. What fraction of the Pacific and Indian oceans' deep water is formed in the Southern Ocean? *Biogeosciences* 15, 3779–3794. <https://doi.org/10.5194/bg-15-3779-2018>.
- Rae, J.W.B., Burke, A., Robinson, L.F., Adkins, J.F., Chen, T., Cole, C., Greenop, R., Li, T., Little, E.F.M., Nita, D.C., Stewart, J.A., Taylor, B.J., 2018. CO<sub>2</sub> storage and release in the deep Southern Ocean on millennial to centennial timescales. *Nature* 562, 569. <https://doi.org/10.1038/s41586-018-0614-0>.
- Rahlf, P., Hathorne, E., Laukert, G., Gutjahr, M., Weideab, S., Frank, M., 2019. Tracing water mass mixing and continental inputs in the southeastern Atlantic Ocean with dissolved neodymium isotopes. *Earth Planet Sci. Lett.* <https://doi.org/10.1016/j.epsl.2019.115944>, 115944.
- Rashid, H., England, E., Thompson, L., Polyak, L., 2011. Late glacial to Holocene Indian summer monsoon variability based upon sediment records taken from the Bay of Bengal. *Terr. Atmos. Ocean Sci.* 22, 215–228. [https://doi.org/10.3319/TAO.2010.09.17.02\(TibXS\)](https://doi.org/10.3319/TAO.2010.09.17.02(TibXS)).
- Rashid, H., Gourlan, A.T., Marche, B., Sheppard, K., Khélifi, N., 2019. Changes in Indian summer monsoon using neodymium (Nd) isotopes in the Andaman Sea during the last 24,000 years. *Earth Syst. Environ.* <https://doi.org/10.1007/s41748-019-00105-0>.
- Reimi, M.A., Marcantonio, F., 2016. Constraints on the magnitude of the deglacial migration of the ITCZ in the central equatorial Pacific ocean. *Earth Planet Sci. Lett.* 453, 1–8. <https://doi.org/10.1016/j.epsl.2016.07.058>.
- Rempfer, J., Stocker, T.F., Joos, F., Dutay, J.-C., 2012a. On the relationship between Nd isotopic composition and ocean overturning circulation in idealized freshwater discharge events. *Paleoceanogr.* 27. <https://doi.org/10.1029/2012PA002312>.
- Rempfer, J., Stocker, T.F., Joos, F., Dutay, J.-C., 2012b. Sensitivity of Nd isotopic composition in seawater to changes in Nd sources and paleoceanographic implications. *J. Geophys. Res. Oceans* 117. <https://doi.org/10.1029/2012JC008161>.
- Rempfer, J., Stocker, T.F., Joos, F., Dutay, J.-C., Siddall, M., 2011. Modelling Nd-isotopes with a coarse resolution ocean circulation model: sensitivities to model parameters and source/sink distributions. *Geochem. Cosmochim. Acta* 75, 5927–5950. <https://doi.org/10.1016/j.gca.2011.07.044>.
- Revel, M., Sinko, J., Grousset, F., 1996. Sr and Nd isotopes as tracers of North Atlantic lithic particles: paleoclimatic implications. *Paleoceanogr.* 11, 95–113. <https://doi.org/10.1029/95PA03199>.
- Roberts, N.L., Piotrowski, A.M., 2015. Radiogenic Nd isotope labeling of the northern NE Atlantic during MIS 2. *Earth Planet Sci. Lett.* 423, 125–133. <https://doi.org/10.1016/j.epsl.2015.05.011>.
- Roberts, N.L., Piotrowski, A.M., Elderfield, H., Eglinton, T.I., Lomas, M.W., 2012. Rare earth element association with foraminifera. *Geochem. Cosmochim. Acta* 94, 57–71. <https://doi.org/10.1016/j.gca.2012.07.009>.
- Roberts, N.L., Piotrowski, A.M., McManus, J.F., Keigwin, L.D., 2010. Synchronous deglacial overturning and water mass source changes. *Science* 327, 75–78. <https://doi.org/10.1126/science.1178068>.
- Robinson, L.F., Adkins, J.F., Keigwin, L.D., Southon, J., Fernandez, D.P., Wang, S.-L., Scheirer, D.S., 2005. Radiocarbon variability in the western North Atlantic during the last deglaciation. *Science* 310, 1469–1473. <https://doi.org/10.1126/science.1114832>.
- Ronge, T.A., Tiedemann, R., Lamy, F., Köhler, P., Alloway, B.V., Pol-Holz, R.D., Pahnke, K., Southon, J., Wacker, L., 2016. Radiocarbon constraints on the extent and evolution of the South Pacific glacial carbon pool. *Nat. Commun.* 7, 11487. <https://doi.org/10.1038/ncomms11487>.
- Rousseau, T.C.C., Sonke, J.E., Chmeleff, J., Beek, P. van, Souhaut, M., Boaventura, G., Seyler, P., Jeandel, C., 2015. Rapid neodymium release to marine waters from lithogenic sediments in the Amazon estuary. *Nat. Commun.* 6, 7592. <https://doi.org/10.1038/ncomms8592>.
- Ruddiman, W.F., 1977. Late Quaternary deposition of ice-rafted sand in the subpolar North Atlantic (lat 40° to 65°N). *GSA Bull.* 88, 1813–1827. [https://doi.org/10.1130/0016-7606\(1977\)88<1813:LQDOIS>2.0.CO;2](https://doi.org/10.1130/0016-7606(1977)88<1813:LQDOIS>2.0.CO;2).
- Rutberg, R.L., Hemming, S.R., Goldstein, S.L., 2000. Reduced North Atlantic deep water flux to the glacial Southern Ocean inferred from neodymium isotope ratios. *Nature* 405, 935–938. <https://doi.org/10.1038/35016049>.
- Sarnthein, M., Schneider, B., Grootes, P.M., 2013. Peak glacial <sup>14</sup>C ventilation ages suggest major draw-down of carbon into the abyssal ocean. *Clim. Past* 9, 2595–2614. <https://doi.org/10.5194/cp-9-2595-2013>.
- Sarnthein, M., Winn, K., Jung, S.J.A., Duplessy, J.-C., Labeyrie, L., Erlenkeuser, H., Ganssen, G., 1994. Changes in East Atlantic deepwater circulation over the last 30,000 years: eight time slice reconstructions. *Paleoceanogr.* 9, 209–267. <https://doi.org/10.1029/93PA03301>.
- Schlitzer, R., Anderson, R.F., Dodas, E.M., Lohan, M., Geibert, W., Tagliabue, A., Bowie, A., Jeandel, C., Maldonado, M.T., Landing, W.M., Cockwell, D., Abadie, C., Abouchami, W., Achterberg, E.P., Agather, A., Aguiar-Islas, A., van Aken, H.M., Andersen, M., Archer, C., Auro, M., de Baar, H.J., Baars, O., Baker, A.R., Bakker, K., Basak, C., Baskaran, M., Bates, N.R., Bauch, D., van Beek, P., Behrens, M.K., Black, E., Blumh, K., Bopp, L., Bouman, H., Bowman, K., Bown, J., Boyd, P., Boyle, M., Boyle, E.A., Branellec, P., Bridgestock, L., Brissebrat, G., Browning, T., Bruland, K.W., Brumsack, H.-J., Brzezinski, M., Buck, C.S., Buck, K.N., Buesseler, K., Bull, A., Butler, E., Cai, P., Mor, P.C., Cardinal, D., Carlson, C., Carrasco, G., Casacuberta, N., Casciotti, K.L., Castrillejo, M., Chamizo, E., Chance, R., Charette, M.A., Chaves, J.E., Cheng, H., Chever, F., Christl, M., Church, T.M., Closset, I., Colman, A., Conway, T.M., Cossa, D., Croot, P., Cullen, J.T., Cutter, G.A., Daniels, C., Dehairs, F., Deng, F., Dieu, H.T., Duggan, B., Dulaquais, G., Dumoussaud, C., Echegoyen-Sanz, Y., Edwards, R.L., Ellwood, M., Fahrbach, E., Fitzsimmons, J.N., Russell Flegel, A., Fleisher, M.Q., van de Fliedert, T., Frank, M., Friedrich, J., Fripiat, F., Fröllje, H., Galer, S.J.G., Gamo, T., Ganeshram, R.S., Garcia-Orellana, J., Garcia-Solsona, E., Gault-Ringold, M., George, E., Gerringa, L.J.A., Gilbert, M., Godoy, J.M., Goldstein, S.L., Gonzalez, S.R., Grissom, K., Hammerschmidt, C., Hartman, A., Hassler, C.S., Hathorne, E.C., Hatta, M., Hawco, N., Hayes, C.T., Heimbürger, L.-E., Helgøe, J., Heller, M., Henderson, G.M., Henderson, P.B., van Heuven, S., Ho, P., Horner, T.J., Hsieh, Y.-T., Huang, K.-F., Humphreys, M.P., Isshiki, K., Jacquot, J.E., Janssen, D.J., Jenkins, W.J., John, S., Jones, E.M., Jones, J.L., Kadko, D.C., Kayser, R., Kenna, T.C., Khondoker, R., Kim, T., Kipp, L., Klar, J.K., Klunder, M., Kretschmer, S., Kumamoto, Y., Laan, P., Labatut, M., Lacan, F., Lam, P.J., Lambelet, M., Lamborg, C.H., Le Moigne, F.A.C., Le Roy, E., Lechtenfeld, O.J., Lee, J.-M., Lherminier, P., Little, S., López-Lora, M., Lu, Y., Masque, P., Mawji, E., McClain, C.R., Measures, C., Mehic, S., Barraqueta, J.-L.M., van der Merwe, P., Middag, R., Mieruch, S., Milne, A., Minami, T., Moffett, J.W., Moncoiffe, G., Moore, W.S., Morris, P.J., Morton, P.L., Nakaguchi, Y., Nakayama, N., Niedermiller, J., Nishioka, J., Nishiuchi, A., Noble, A., Obata, H., Ober, S., Ohnemus, D.C., van Ooijen, J., O'Sullivan, J., Owens, S., Pahnke, K., Paul, M., Pavia, F., Pena, L.D., Peters, B., Planchon, F., Planquette, H., Pradoux, C., Puigcorbè, V., Quay, P., Queroue, F., Radic, A., Rauschenberg, S., Rehkämper, M., Rember, R., Remenyi, T., Resing, J.A., Rickli, J., Rigaud, S., Rijkenberg, M.J.A., Rintoul, S., Robinson, L.F., Roca-Martí, M., Rodellas, V., Roeske, T., Rolison, J.M., Rosenberg, M., Roshan, S., Rutgers van der Loeff, M.M., Ryabenko, E., Saito, M.A., Salt, L.A., Sanial, V., Sarthou, G., Schallenberg, C., Schauer, U., Scher, H., Scheller, C., Schnetger, B., Scott, P., Sedwick, P.N., Semiletov, I., Shelley, R., Sherrell, R.M., Shiller, A.M., Sigman, D.M., Singh, S.K., Slagter, H.A., Slater, E., Smethie, W.M., Snaith, H., Sohrin, Y., Soht, B., Sonke, J.E., Speich, S., Steinfeldt, R., Stewart, G., Stichel, T., Stirling, C.H., Stutsman, J., Swarr, G.J., Swift, J.H., Thomas, A., Thorne, K., Till, C.P., Till, R., Townsend, A.T., Townsend, E., Tuerena, R., Twining, B.S., Vance, D., Velazquez, S., Venchiarutti, C., Villa-Alfageme, M., Vivancos, S.M., Voelker, A.H.L., Wake, B., Warner, M.J., Watson, R., van Weerlee, E., Alexandra Weigand, M., Weinstein, Y., Weiss, D., Wisotzki, A., Woodward, E.M.S., Wu, J., Wu, Y., Wuttig, K., Wyatt, N., Xiang, Y., Xie, R.C., Xue, Z., Yoshikawa, H., Zhang, J., Zhang, P., Zhao, Y., Zheng, L., Zheng, X.-Y., Zieringer, M., Zimmer, L.A., Ziveri, P., Zunino, P., Zurbrugg, C., 2018. The GEO-TRACES intermediate data product 2017. *Chem. Geol.* 493, 210–223. <https://doi.org/10.1016/j.chemgeo.2018.05.040>.
- Schmitt, J., Schneider, R., Elsig, J., Leuenberger, D., Lourantou, A., Chappellaz, J., Köhler, P., Joos, F., Stocker, T.F., Leuenberger, M., Fischer, H., 2012. Carbon isotope constraints on the deglacial CO<sub>2</sub> rise from ice cores. *Science* 336, 711–714. <https://doi.org/10.1126/science.1217161>.
- Schmittner, A., Lund, D.C., 2015. Early deglacial Atlantic overturning decline and its role in atmospheric CO<sub>2</sub> rise inferred from carbon isotopes ( $\delta^{13}\text{C}$ ). *Clim. Past* 11, 135–152. <https://doi.org/10.5194/cp-11-135-2015>.
- Shackleton, S., Bereiter, B., Baggenstos, D., Bauska, T.K., Brook, E.J., Marcott, S.A.,

- Severinghaus, J.P., 2019. Is the noble gas-based rate of ocean warming during the younger Dryas overestimated? *Geophys. Res. Lett.* 46, 5928–5936. <https://doi.org/10.1029/2019GL082971>.
- Shakun, J.D., Clark, P.U., He, F., Marcott, S.A., Mix, A.C., Liu, Z., Otto-Bliesner, B., Schmittner, A., Bard, E., 2012. Global warming preceded by increasing carbon dioxide concentrations during the last deglaciation. *Nature* 484, 49–54. <https://doi.org/10.1038/nature10915>.
- Siddall, M., Khaliwala, S., van de Flierdt, T., Jones, K., Goldstein, S.L., Hemming, S., Anderson, R.F., 2008. Towards explaining the Nd paradox using reversible scavenging in an ocean general circulation model. *Earth Planet Sci. Lett.* 274, 448–461. <https://doi.org/10.1016/j.epsl.2008.07.044>.
- Sikes, E.L., Allen, K.A., Lund, D.C., 2017. Enhanced  $\delta^{13}\text{C}$  and  $\delta^{18}\text{O}$  differences between the south Atlantic and South Pacific during the last glaciation: the deep gateway hypothesis. *Paleoceanography* 32, 1000–1017. <https://doi.org/10.1002/2017PA003118>.
- Sikes, E.L., Samson, C.R., Guilderson, T.P., Howard, W.R., 2000. Old radiocarbon ages in the southwest Pacific Ocean during the last glacial period and deglaciation. *Nature* 405, 555–559. <https://doi.org/10.1038/35014581>.
- Skinner, L.C., Fallon, S., Waelbroeck, C., Michel, E., Barker, S., 2010. Ventilation of the deep Southern Ocean and deglacial  $\text{CO}_2$  rise. *Science* 328, 1147–1151. <https://doi.org/10.1126/science.1183627>.
- Skinner, L.C., Primeau, F., Freeman, E., Fuente, M. de la, Goodwin, P.A., Gottschalk, J., Huang, E., McCave, I.N., Noble, T.L., Scrivner, A.E., 2017. Radiocarbon constraints on the glacial ocean circulation and its impact on atmospheric  $\text{CO}_2$ . *Nat. Commun.* 8, 16010. <https://doi.org/10.1038/ncomms16010>.
- Skinner, L.C., Scrivner, A.E., Vance, D., Barker, S., Fallon, S., Waelbroeck, C., 2013. North Atlantic versus Southern Ocean contributions to a deglacial surge in deep ocean ventilation. *Geology* 41, 667–670. <https://doi.org/10.1130/G34133.1>.
- Stichel, T., Pahnke, K., Duggan, B., Goldstein, S.L., Hartman, A.E., Paffrath, R., Scher, H.D., 2018. TAG plume: revisiting the hydrothermal neodymium contribution to seawater. *Front. Mar. Sci.* 5, 96. <https://doi.org/10.3389/fmars.2018.00096>.
- Struve, T., Roberts, N.L., Frank, M., Piotrowski, A.M., Spielhagen, R.F., Gutjahr, M., Teschner, C., Bauch, H.A., 2019. Ice-sheet driven weathering input and water mass mixing in the Nordic Seas during the last 25,000 years. *Earth Planet Sci. Lett.* 514, 108–118. <https://doi.org/10.1016/j.epsl.2019.02.030>.
- Struve, T., van de Flierdt, T., Burke, A., Robinson, L.F., Hammond, S.J., Crocket, K.C., Bradtmiller, L.L., Auro, M.E., Mohamed, K.J., White, N.J., 2017. Neodymium isotopes and concentrations in aragonitic scleractinian cold-water coral skeletons - modern calibration and evaluation of palaeo-applications. *Chem. Geol.* 453, 146–168. <https://doi.org/10.1016/j.chemgeo.2017.01.022>.
- Tachikawa, K., Arsouze, T., Bayon, G., Bory, A., Colin, C., Dutay, J.-C., Frank, N., Giraud, X., Gourlan, A.T., Jeandel, C., Lacan, F., Meynadier, L., Montagna, P., Piotrowski, A.M., Plancherel, Y., Pucéat, E., Roy-Barman, M., Waelbroeck, C., 2017. The large-scale evolution of neodymium isotopic composition in the global modern and Holocene ocean revealed from seawater and archive data. *Chem. Geol.* 457, 131–148. <https://doi.org/10.1016/j.chemgeo.2017.03.018>.
- Tachikawa, K., Athias, V., Jeandel, C., 2003. Neodymium budget in the modern ocean and paleo-oceanographic implications. *J. Geophys. Res. Oceans* 108, 3254. <https://doi.org/10.1029/1999JC000285>.
- Tachikawa, K., Piotrowski, A.M., Bayon, G., 2014. Neodymium associated with foraminiferal carbonate as a recorder of seawater isotopic signatures. *Quat. Sci. Rev.* 88, 1–13. <https://doi.org/10.1016/j.quascirev.2013.12.027>.
- Talley, L.D., 2013. Closure of the global overturning circulation through the Indian, Pacific, and southern oceans: schematics and transports. *Oceanography* 21, 80–97. <https://doi.org/10.5670/oceanog.2013.07>.
- Thornalley, D.J.R., Bauch, H.A., Gebbie, G., Guo, W., Ziegler, M., Bernasconi, S.M., Barker, S., Skinner, L.C., Yu, J., 2015. A warm and poorly ventilated deep Arctic Mediterranean during the last glacial period. *Science* 349, 706–710. <https://doi.org/10.1126/science.aaa9554>.
- van de Flierdt, T., Griffiths, A.M., Lambelet, M., Little, S.H., Stichel, T., Wilson, D.J., 2016. Neodymium in the oceans: a global database, a regional comparison and implications for palaeoceanographic research. *Philos. Trans. R. Soc. A* 374, 20150293. <https://doi.org/10.1098/rsta.2015.0293>.
- Vance, D., Little, S.H., de Souza, G.F., Khaliwala, S., Lohan, M.C., Middag, R., 2017. Silicon and zinc biogeochemical cycles coupled through the Southern Ocean. *Nat. Geosci.* 10, 202–206. <https://doi.org/10.1038/ngeo2890>.
- Verplanck, E.P., Farmer, G.L., Andrews, J., Dunhill, G., Millo, C., 2009. Provenance of Quaternary glacial and glaciomarine sediments along the southeast Greenland margin. *Earth Planet Sci. Lett.* 286, 52–62. <https://doi.org/10.1016/j.epsl.2009.06.012>.
- von Blanckenburg, F., Bouchez, J., Ibarra, D.E., Maher, K., 2015. Stable runoff and weathering fluxes into the oceans over Quaternary climate cycles. *Nat. Geosci.* 8, 538–542. <https://doi.org/10.1038/ngeo2452>.
- Waelbroeck, C., Paul, A., Kucera, M., Rosell-Melé, A., Weinelt, M., Schneider, R., Mix, A.C., Abelmann, A., Armand, L., Bard, E., Barker, S., Barrows, T.T., Benway, H., Cacho, I., Chen, M.-T., Cortijo, E., Crosta, X., Vernal, A. de, Dokken, T., Duprat, J., Elderfield, H., Eynaud, F., Gersonde, R., Hayes, A., Henry, M., Hillaire-Marcel, C., Huang, C.-C., Jansen, E., Juggins, S., Kallel, N., Kiefer, T., Kienast, M., Labeyrie, L., Leclaire, H., Londeix, L., Mangin, S., Matthiessen, J., Marret, F., Meland, M., Morey, A.E., Mulitza, S., Pflaumann, U., Piasis, N.G., Radi, T., Rochon, A., Rohling, E.J., Sbaiff, L., Schäfer-Neth, C., Solignac, S., Spero, H., Tachikawa, K., Turon, J.-L., 2009. Constraints on the magnitude and patterns of ocean cooling at the Last Glacial Maximum. *Nat. Geosci.* 2, 127–132. <https://doi.org/10.1038/ngeo411>.
- Wei, R., Abouchami, W., Zahn, R., Masque, P., 2016. Deep circulation changes in the south Atlantic since the last glacial Maximum from Nd isotope and multi-proxy records. *Earth Planet Sci. Lett.* 434, 18–29. <https://doi.org/10.1016/j.epsl.2015.11.001>.
- Wilson, D.J., Piotrowski, A.M., Galy, A., Clegg, J.A., 2013. Reactivity of neodymium carriers in deep sea sediments: implications for boundary exchange and paleoceanography. *Geochem. Cosmochim. Acta* 109, 197–221. <https://doi.org/10.1016/j.gca.2013.01.042>.
- Wilson, D.J., Piotrowski, A.M., Galy, A., McCave, I.N., 2012. A boundary exchange influence on deglacial neodymium isotope records from the deep western Indian Ocean. *Earth Planet Sci. Lett.* 341–344, 35–47. <https://doi.org/10.1016/j.epsl.2012.06.009>.
- Wu, Q., Colin, C., Liu, Z., Douville, E., Dubois-Dauphin, Q., Frank, N., 2015. New insights into hydrological exchange between the South China Sea and the Western Pacific Ocean based on the Nd isotopic composition of seawater. *Deep Sea Res. Part II Top. Stud. Oceanogr.* The South China Sea Deep 122, 25–40. <https://doi.org/10.1016/j.dsr2.2015.11.005>.
- Xie, R.C., Marcantonio, F., 2012. Deglacial dust provenance changes in the Eastern Equatorial Pacific and implications for ITCZ movement. *Earth Planet Sci. Lett.* 317 (318), 386–395. <https://doi.org/10.1016/j.epsl.2011.11.014>.
- Xie, R.C., Marcantonio, F., Schmidt, M.W., 2014. Reconstruction of intermediate water circulation in the tropical North Atlantic during the past 22,000 years. *Geochem. Cosmochim. Acta* 140, 455–467. <https://doi.org/10.1016/j.gca.2014.05.041>.
- Yu, Z., Colin, C., Ma, R., Meynadier, L., Wan, S., Wu, Q., Kallel, N., Sepulcre, S., Dapoigny, A., Bassinot, F., 2018. Antarctic intermediate water penetration into the northern Indian ocean during the last deglaciation. *Earth Planet Sci. Lett.* 500, 67–75. <https://doi.org/10.1016/j.epsl.2018.08.006>.
- Yu, Z., Colin, C., Meynadier, L., Douville, E., Dapoigny, A., Reverdin, G., Wu, Q., Wan, S., Song, L., Xu, Z., Bassinot, F., 2017. Seasonal variations in dissolved neodymium isotope composition in the Bay of Bengal. *Earth Planet Sci. Lett.* 479, 310–321. <https://doi.org/10.1016/j.epsl.2017.09.022>.
- Zhao, N., Marchal, O., Keigwin, L., Amrhein, D., Gebbie, G., 2018. A synthesis of deglacial deep-sea radiocarbon records and their (In)Consistency with modern ocean ventilation. *Paleoceanogr. Paleoclimatol.* 33, 128–151. <https://doi.org/10.1002/2017PA003174>.
- Zhao, N., Oppo, D.W., Huang, K.-F., Howe, J.N.W., Blusztajn, J., Keigwin, L.D., 2019. Glacial-interglacial Nd isotope variability of North Atlantic Deep Water modulated by North American ice sheet. *Nat. Commun.* 10, 1–10. <https://doi.org/10.1038/s41467-019-13707-z>.
- Zheng, X.-Y., Plancherel, Y., Saito, M.A., Scott, P.M., Henderson, G.M., 2016. Rare earth elements (REEs) in the tropical South Atlantic and quantitative deconvolution of their non-conservative behavior. *Geochem. Cosmochim. Acta* 177, 217–237. <https://doi.org/10.1016/j.gca.2016.01.018>.
- Zieringer, M., Frank, M., Stumpf, R., Hathorne, E.C., 2019. The distribution of neodymium isotopes and concentrations in the eastern tropical North Atlantic. *Chem. Geol.* 511, 265–278. <https://doi.org/10.1016/j.chemgeo.2018.11.024>.